Dzyaloshinskii-Moriya Interaction and Domain Wall Motion in Polycrystalline and Epitaxial Magnetic Multilayers

Kowsar Shahbazi

University of Leeds

School of Physics and Astronomy

Submitted in accordance with the requirements for the degree of

Doctor of Philosophy

December, 2018

“Rehearsal of Passion”

Persian calligraphy by Ahmad Teimouri.

Intellectual Property Statement

The candidate confirms that the work submitted is her own and that appropriate credit has been given within the thesis where reference has been made to the work of others.

This copy has been supplied on the understanding that it is copyright material and that no quotation from the thesis may be published without proper acknowledgement.

The right of Kowsar Shahbazi to be identified as Author of this work has been asserted by her in accordance with the Copyright, Designs and Patents Act 1988.

Publications

1. G. V. Karnad, C. Gorini, K. Lee, T. Schulz, R. Lo Conte, A.W.J. Wells, D-S. Han, **K. Shahbazi**, J-S. Kim, T.A. Moore, H.J.M. Swagten, U. Eckern, R. Raimondi, M. Kläui, *Evidence for Phonon Skew Scattering in the Spin Hall Effect of Platinum*, Phys. Rev. B, 97:100405, 2018.
2. P. M. Shepley, H. Tunnicliffe, **K. Shahbazi**, G. Burnell, T.A. Moore, *Tuning Domain Wall Energy with Strain: Balancing Anisotropy and Exchange Energies in Pt/Co/Ir*, Phys. Rev. B, 97:134417, 2018.
3. K. Zeissler, S. Finizio, **K. Shahbazi**, J. Massey, F. Al Ma'Mari, D.M. Bracher, A. Kleibert, M.C. Rosamond, E.H. Linfield, T.A. Moore, J. Raabe, G. Burnell, C.H. Marrows, *Discrete Hall Resistivity Contribution from Néel Skyrmions in Multilayer Nanodiscs*, Nature Nano. 13:1161-1166, 2018.
4. **K. Shahbazi**, A. Hrabec, S. Moretti, M.B. Ward, T.A. Moore, V. Jeudy, E. Martinez, C.H. Marrows, *Magnetic Properties and Field-Driven Dynamics of Chiral Domain Walls in Epitaxial* $Pt/Co/Au_xPt_{1-x}$ *Trilayers*, Phys. Rev. B, 98:214413, 2018.
5. **K. Shahbazi**, J-V. Kim, H.T. Nembach, J.M. Shaw, A. Bischof, M.D. Rossell, V. Jeudy, T.A. Moore, C.H. Marrows, *Domain Wall Motion and Interfacial Dzyaloshinskii-Moriya Interactions in* $Pt/Co/Ir(t_{\mathrm{Ir}})/Ta$ *Multilayers*, arXiv preprint, arXiv:1810.03454, 2018 (Submitted to Phys. Rev. B).

Acknowledgements

First and foremost I would like to express my sincere gratitude to my supervisor, Prof. Chris Marrows for his advice and encouragement during my PhD. I am grateful for his patience, motivation and understanding even in non-scientific aspects of doing research. I'd like to thank Dr. Thomas Moore for his invaluable advice and comments on reports, publications and project meetings.

All the lab works owe much to Dr. Mannan Ali who was always there to answer any peculiar questions about equipment. I would also like to thank Prof. Bryan Hickey and Oscar Cespedes for the hard time they gave me during my transfer and second year viva. Their crucial comments, deep questions and willingness to encourage me to dig deeper, was truly what I needed during my first years. I am grateful to Dr. Gavin Burnell for sharing his never-ending knowledge in the lab or during coffee time (although sometimes it was too deep and complicated that I couldn't digest more than 50% of it).

Special thanks goes to my fellow PIs and researchers in the Marie-Curie Wall network for the insightful discussions and joyful times we had together all around Europe, especially Prof. Gianfranco Durin for single-handedly coordinating the project, and his welcoming and modest attitude towards students.

I cannot thank enough members of CM group, for the friendly environment they offered me, their help in trainings, their sweet treats for coffee time, the lunchtime crosswords, and the group trips. Heartfelt thanks go to my officemates: Jamie, Shoug, Amy and Risalat. Thanks go also to all of the technical staff in the cryogenics, electronics and mechanical workshops who have been always ready and willing to assist. Especially Stewart Weston for his kindness and the warm chats we had.

I have to thank a long list of dear friends, both near and far. Among them are: Arash for listening to me and being a great comfort. Mahdieh for her heavenly food. Ali for his daily calls, and showing me a new side of people. Priya and Fatma, for praising me more than I deserved and always being there for me even thousands of kilometers apart. Katharina, for her strange and delicious food and the green and cheerful flat that we shared.

Saeed, for tolerating my hours-long calls when I was deep down. Rowan and Victoria for their unfinishable kindness and their welcoming lovely smiles. Sophie, for her great sense of humour, who tried to keep me up in my down times. Aleš, for his infinite energy, the "exposed walking" trips and his kind help and support in research. Philippa, for sharing her passion to promote science and support for women scientists. Risalat, for not taking my horrible jokes seriously, and patiently waiting for me at the other side of passport check-points in different airports around the Europe. I am, also, endlessly indebted to Amir for his kind words, support, and motivation during my writing time. This thesis wouldn't be written without his assistance and encouragement.

Last but not least countless thanks goes to my parents, Mahboubeh and Hossein, who always believed in me and supported my ideas no matter how crazy they were. I am profoundly grateful to have you in my life.

Abstract

The domain wall (DW) dynamics of epitaxial and polycrystalline multilayers with perpendicular magnetic anisotropy have been investigated. DC magnetron sputtering was used to deposit different multilayers. The saturation magnetization, anisotropy energies, exchanges stiffness constant, and DW width and energy density were calculated using hard-axis hysteresis loops and change of magnetization with temperature. The evaluated magnetic parameters were used in study of asymmetrical bubble expansion and Brillouin light spectroscopy (BLS) spectra to derive the strength of interfacial Dzyaloshinskii-Moriya interaction (DMI) in the films.

Pt\Co\Au_xPt_{1-x} ($x = 0,\ 0.5,\ 1$) epitaxial trilayers with increasing broken inversion symmetry were deposited by sputtering. Zero DMI and no visible current-induced DW motion proven the expected fully symmetrical layers and interfaces in the case of $x = 0$. Field-induced DW motion (FIDWM) was used to calculate the depinning field, temperature, and velocity. All these material dependent parameters increased with x. They were used to estimate the value of Gilbert damping constant, which was compared to the same value evaluated from full micromagnetic calculations performed in colaboration with Simone Moretti. Larger values of Gilbert damping from FIDWM were attributed to other dissipation mechanisms that happen solely during DW motion. It was shown that DMI and SHE in the multilayers rise with concentration of Au on the top layer.

The effect of inserting Ir in the top interface of polycrystalline Pt\Co\Ta films was also investigated through DMI and DW behaviour. It was shown that motion of the left-handed DWs in Pt\Co\Ir(t_{Ir})\Ta multilayers (t_{Ir} = 0.0–2.0 nm) perfectly follows the universal creep and depinning regimes. The depinning related parameters and evaluated DMI did not change significantly for Ir of more than two monolayers. Evaluation of DMI showed that insertion of Ir layer reduces the net DMI of the multilayer, suggesting a negative DMI constant for Ir\Co interfaces. This opposes previous theoretical calculations and experimental studies. The observed anomalies in asymmetrical bubble expansion results could not be explained with the previous simple creep model of DW motion. Including changes of depinning field with in-plane applied field into the dynamics, micromagnetic simulation by

Joo-Von Kim could successfully reproduce the experimental data.

Finally, to study the DMI of Hf layers with different thicknesses, multilayers of Pt\Co\Hf(t_{Hf})\Ta (t_{Hf} = 0.0–2.0 nm) were deposited. The magnetic characterization of films showed an approximately 0.7 nm thick magnetic dead-layer in the multilayers. The DMI in these films was again investigated using BLS and asymmetric bubble expansion. The results showed that Hf enhances DMI in the stack, suggesting a positive sign of DMI for the Hf\Co interface, which is opposite to DMI of Pt\Co interfaces. Changing the thickness did not show a significant effect on DMI factor.

Contents

Abbreviations

AC	Alternating Current
BLS	Brillouin Light Scattering
BW	Bloch Wall
CIDWM	Current-Induced Domain Wall Motion
DC	Direct Current
DL	Dead Layer
DMI	Dzyaloshinskii-Moriya Interaction
DU	Down-Up
DW	Domain Wall
EDX	Energy Dispersive X-ray Spectroscopy
FCC	Face-Centred Cubic
FIB	Focused Ion-Beam
FIDWM	Field-Induced Domain Wall Motion
FM	Ferromagnet/Ferromagnetic
HAADF	High Angle Annular dark Field
HDD	Hard Disk Drive
HM	Heavy Metal
HRSTEM	High Resolution Scanning TEM
InP	In-Plane
LH	Left-Handed
LW	Left domain Wall
MOKE	Magneto-Optical Kerr Effect
MTM	Multi-Target Module
NM	Normal Metal
NW	Néel Wall
OoP	Out-of-Plane
PMA	Perpendicular Magnetic Anisotropy
RF	Radio Frequency
RGA	Residual Gas Analyser
RH	Right-handed
RT	Room Temperature
RW	Right domain Wall
SEM	Scanning Electron Microscope
SHA	Spin Hall Angle
SHE	Spin Hall Effect
SLT	Slonczewski-like Torque
SOT	Spin-Orbit Torque
SQUID	Superconducting Quantum Interface Device
SSD	Solid State Drive
STT	Spin Transfer Torque
SW	Spin Wave
TEM	Transmission Electron Microscope
UD	Up-Down
VSM	Vibrating Sample Magnetometry
XRD	X-Ray Diffraction
XRR	X-Ray Reflectivity

Chapter 1

Introduction

1.1 A Moving Wall

The Oxford dictionary says a *wall* is "something that forms a barrier or stops you from making progress"[1], but how about using the very same thing to make progress?

Wall, truly and mostly, is a structure to separate two regions and to forbid intrusion, whether it is in architecture, human cells, or even in a computer's firewall. But in magnetic materials it is created to reduce the energy cost [2], moves to get uniformity, and wraps up to make topologically stable hedgehogs [3, 4].

Magnetic domain walls are the smallest magnetic textures that can, potentially, be used in new generation of digital processing and recording technique, so-called spintronics [5]. Spintronics is simply spin-based electronics and aims to increase processing speed, reduce power consumption and more importantly integrate the processing and recording parts of a digital system (*i.e.* logic and memory) [6, 7]. These two parts are currently operating with different materials and concepts: on one hand there are semiconductor devices for processing side and on the other hand, there are magnetic, optical, magneto-optical, or solid-state media to save data for processing.

On top of that, today's most common non-volatile memories have mechanical reading and writing parts, nanometres away from the media, which makes them very vulnerable to any shock. Also, the amount of data need to be saved and/or processed is growing rapidly. Just as a little example, $\sim$ 300 hours of video is uploaded onto Youtube every minute [8]. This amount of data needs an even bigger capacity of volatile and non-volatile data storage devices, as it's not just the data need to be saved, but also there are many processing issues and codes acting on them.

There are different types of storage media on the market, but each have their own imperfections. Solid-state random access memories (known mostly as SSDs) are fast, although expensive. Magnetic hard disk drives (HDDs) are cheap but slow [9]. Going into more details, SSDs are based on different technologies, each one has its own disadvantages as well, including finite number of write cycles before having an unpredictable operation, big effective cell size [7], and low write time and read data rate [7]. If there were a single memory storage benefiting from both low cost of HDDs and high performance and reliability of SSDs, the non-volatile storage technology could take a breath. The new introduced memory should have high capacity, low power and short access time, preferably at no cost increase to be able to be called a *universal memory*.

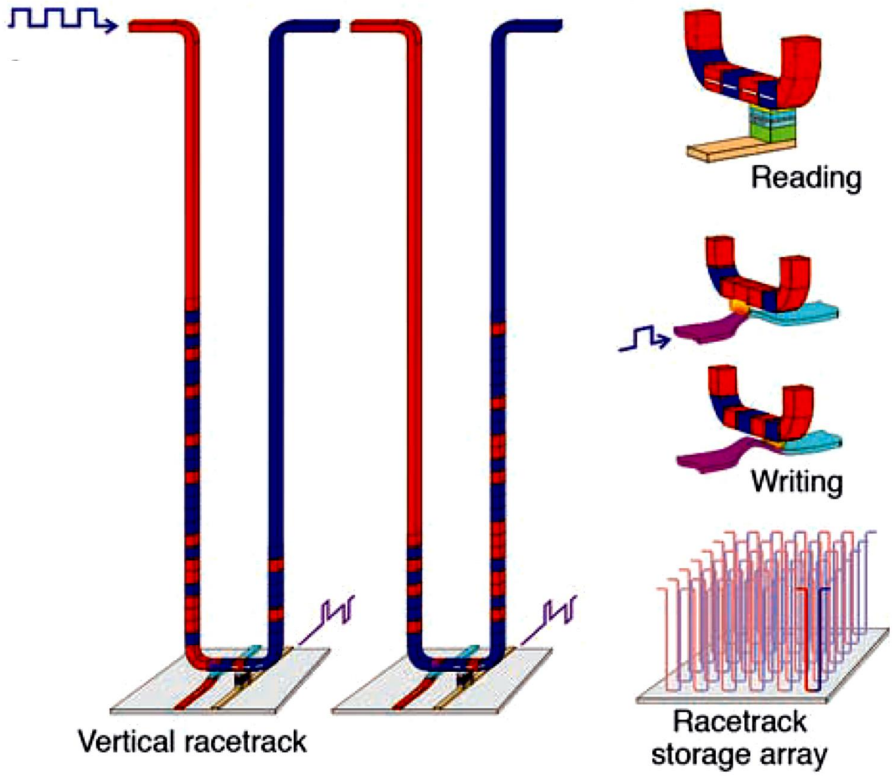

Figure 1.1: A proposed shape of a racetrack memory, as a 3D compatible storage media storing the data in U-shaped nanowire perpendicular to the substrate plane [7]

The proposed magnetic recording media –so-called race-track memories– are promised to overcome these obstacles using domain walls (DWs) or skyrmions [7]. Literally, these devices are based on moving successive closely-spaced DWs along the racetrack that can be moved and controlled by spin polarized currents going through the track (Figure 1.1). This, puts down the need of moving and separate mechanical parts as the writing and reading heads will be stable and connected to the track. The spin current may be produced inside the bulk of the heavy metal layer deposited next to main ferromagnetic layer (spin Hall effect) or at interfaces with metal or metal-oxide films (Rashba effect) [10]. Clearly, to have short access time and low power consumption the DW speed should be the highest possible, while the employed electric current to do so stays at lowest conceivable value.

To be able to control these components efficiently, interfacial Dzyaloshinskii-Moriya interaction (DMI) and spin-Hall effect (SHE) should be optimized in multilayer systems.

The latter, would cause Slonczewski-like torque (SLT) –or as it is often called damping-like torque– to be applied on ferromagnetic layer whose strength determines maximum velocity with which the wall can move [11]. The former would change the energetically favourable DWs from Bloch to chiral Néel in a system with perpendicular magnetic anisotropy (PMA) [12]. Néel walls, unlike Bloch walls, are sensitive to SLT [11, 13]. To optimize SHE and DMI we need to use materials with high spin-orbit interaction and one of the best candidates would be 5d materials (heavy metals) [14, 15]. To have DMI one also needs broken inversion symmetry in the system [16].

1.2 The Interaction That Brings up Homochirality

"Perhaps looking-glass milk isn't good to drink", Alice says to Kitty [17], like she already knew that the mirrored milk might not be digestible. It's true; and it's not just in fiction that handedness is important. Just about everything in life is chiral. Opposite chirality of flavourings are usually different in scent and/or taste [18]. Amino acids in living organisms always have one handedness: they are left-handed [19]. Your digestive system just acts on right-handed sugar and passes on the left-handed ones [20]. Humans, even, are nearly homochiral: 90% right-handed vs. only 10% left-handed [21]. The chirality of life is what makes it work as smoothly as it does. But what does *chiral* mean? Lord Kelvin in 1883 said "I call any geometrical figure or any groups of points chiral and say it has chirality if its image in a plane mirror, ideally realized cannot be brought to coincide with itself."[22]. How did life choose one mirror reflection over another? As much as the answer is an evolutionary mystery for handedness of humans, it is now obvious that DMI plays the god for homochiral magnetic domain walls in multilayer thin films.

The exchange interaction in ferromagnetic materials dictates that the spins should stay parallel to each other. As this effect is symmetric with swapping the two spins, it is more known as the *symmetric exchange*. On the other hand, anti-symmetric exchange is the interaction that changes sign with changing spin order, which wants the neighbouring spins to be perpendicular to one another. Igor Dzyaloshinskii proposed this interaction for the first time in 1957 [23]. Later, in 1960, Toru Moriya calculated the interaction for local magnetic systems [24]. Dzyaloshinskii stated that this interaction will only happen when both low symmetry and spin-orbit coupling are present. In 1990 A. Fert suggested the possibility of DMI observation at the surface of magnetic material

[25], which strength was studied analytically by Crépieux and Lacroix in 1998 [26]. It took 9 years to observe the DMI arising from surfaces/interfaces experimentally [27]. Soon after, first principles calculations explained the rotation of DW from Bloch to Néel type and its handedness for F\W(110) films [28]. At the end of their article, they invited experimentalists to "unravel and exploit these phenomena in more detail"[28].

Since the recall of Heide *et al.* till today, investigation of DMI in multilayer thin films has been extensive. Specially, the study of DMI in systems with PMA became a hot subject in investigations of domain wall dynamics. Different combinations of multilayers have been investigated for evaluation of DMI in different materials [29–33]. It has been shown that although this effect arrises because of the high spin-orbit coupling of the heavy metal layer in ferromagnet/heavymetal (FM/HM) multilayers, DMI can still change sign and strength depending on the adjacent ferromagnetic material [34]. Practically, as the existence of DMI is dependent on breaking the symmetry, any physical change in the multilayer system, even in the atomic level, can enhance this effect. This can be from using different layers at either sides of a FM [35], altering the thickness of either the FM layer [31, 36] or the neighbouring layer [12, 37, 38], changing the morphology of the interface by annealing temperature [39], deposition temperature [40], changing Ar partial pressure during sputtering [41], insertion of a dusting layer [12], to proximity induced magnetization [31, 42]. Even nominally symmetrical layers, if polycrystalline, can exhibit a non-zero DMI [12, 43, 44].

As stated, adding this DMI term into the free energy of a non-centrosymmetric system, left and right handed degeneracy would be broken, and homochirality is observed. The theory of chiral symmetry breaking was formulated in 2001 by Bogdanov and Rössler [45]. In particular, for current induced motion of DWs, when current is applied to the system domain walls with dissimilar chirality will move in opposite directions [13]. Thus, in a nanowire (*i.e.* racetrack) with no specific chirality, DWs will move towards each other and annihilate. As such, the handedness or chirality of the system would be important for application and is favourable if it can be tuned. Also, controlling the direction of domain wall motion under the influence of a spin Hall torque in such systems is vital. This will happen in systems that have broken inversion symmetry and Néel wall with a definite chirality. In such structures, the DMI dictates a preferred direction of motion for a DW depending on the direction of DM vector [10, 46]. Moreover, DMI will delay the Walker breakdown field, leading to higher

velocities for the DW [11].

In summary, DW type, homochirality of the system, DW's direction of motion and its achievable speed before breakdown are all indebted to symmetry breaking at the interface and spin-orbit coupling strength, causing the antisymmetric exchange interaction, called DMI.

1.3 The Effect of Separation

Devices with perpendicular magnetic anisotropy are more promising for spintronic devices based on current-induced domain wall motion (CIDWM) considering the interaction between the current and domain walls, also wall size [12]. Passing a current through a ferromagnetic layer with a fixed magnetization, one can make spin polarized current. If this spin-polarized current goes into another ferromagnetic layer, transfer of spin can apply a torque on the magnetization of the layer. This effect is called spin transfer torque (STT) and was used exctensively in magnetic tunnel junctions or spin valves. Another way to introduce torque in such devices is to put a ferromagnet (FM) in adjacent to a heavy metal (HM). Charge current passing through a heavy metal material with a strong spin-orbit coupling would induce a non-equilibrium spin accumulation transverse to the charge flow [47], this phenomenon is called the spin Hall effect. Also, in 2D structures, the asymmetry of potential in normal direction of the 2D plane causes a momentum-dependent splitting of spin bands, namely the Rashba effect, named after Emmanuel Rashba the discoverer [48]. These two effects cause spin angular momentum transfer to the wall, hence applying a torque to moments, the so-called spin orbit torque (SOT) that makes DWs to move forward [7]. In the case of devices with Out-of-plane (OoP) anisotropy, it was thought that the dominant effect to manipulate the magnetic tilting is the Rashba effect [49], but in 2012 it was shown that SHE torque can actually manipulate magnetization in such systems using current comparable to spin transfer torque tunnel junctions [50]. As one wants to keep the needed charge current as low as possible, the materials with bigger produced spin-current (hence spin-torque) will be favourable. The conversion efficiency is defined as the ratio of spin current to the charge current which is called spin Hall angle (SHA) [51]. Consequently search for a material/structure with a large spin Hall effect is important to get a high efficiency of current induced DW motion system.

Spin Hall effect is an effect similar to conventional Hall effect but for spins. As

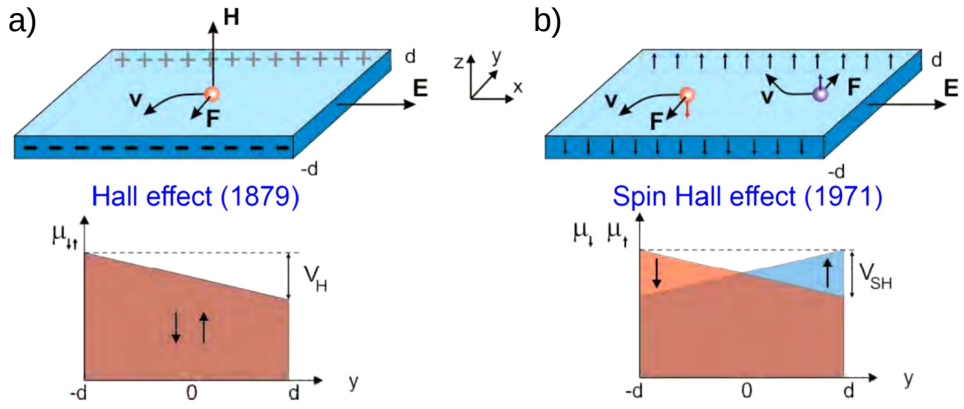

Figure 1.2: a) Hall effect vs. b) spin Hall effect [56]

Figure 1.2 represents, in conventional Hall effect charges with dissimilar sign passing a film in a presence of out of plane magnetic field would accumulate on opposite edges of the film, as a result of the Lorentz force. Thus, a voltage difference can be detected transverse to the current direction. In the spin Hall effect, a film with a passing electron current would experience a spin accumulation on lateral surfaces of the film. It was first predicted by Dyakonov and Perel in 1971 [52] but could not be directly observed until 33 years after in GaAs semiconductor systems [53, 54]. Nevertheless, it still needed some years to become something technologically applicable as Dyakonov said "What is it good for, practically? So far, nobody knows. My personal opinion is that the Spin Hall Effect is one of the many physical phenomena, which do not have any practical applications."[55]

In the presence of spin-orbit coupling, an electron current J_c passing through a metal along the film plane would acquire spin polarization perpendicular to the surface of the film. If we consider the polarization vector $\hat{p}$, then the produced transverse spin current J_s is along y axis and can be derived as:

$$\vec{J_s} = \theta_{SH}\, \hat{p} \times \vec{J_c} \tag{1.1}$$

where θ_{SH} is the dimensionless spin Hall angle. It might be also useful to define spin Hall conductivity which can be written as $\sigma_{SH} = (\hbar/2e)\theta_{SH}\sigma_c$ in which σ_c is the normal conductivity of material [57].

As mentioned, the early observations of SHE was done in semiconductor materials via optical methods [54]. The very first electrical measurement of SHE (practically

inverse SHE) in metals has been done by S. Valenzuela and M. Tinkham [58] in a lateral ferromagnet-normal metal structure at low temperature. Not long after, T. Kimura from the Y. Otani group [59] reported room-temperature spin Hall measurement in Pt and evaluated the SHA of Pt to be 0.0037. Although it was a high underestimation, this measurement was a breakthrough because initially, it was the first observed SHE at room temperature, secondly, it was the first direct SHE measurement in metals and at last, it showed that the spin Hall conductivity of Pt is much larger (10^4 times [59]) than the studied semiconductor systems. Since then, the spin Hall angle of Pt was intensely evaluated and yet there is a lot of disagreement in its value, some of them even differ by more than an order of magnitude using different approaches to measure the spin Hall angle [60]. The spin Hall angle of platinum –which is the most famous heavy metal in such systems– reported to have values $0.0037 < \theta_{\mathrm{SH,Pt}} < 0.37$ [59–66]. Moreover, β-Ta, Pt-doped Au and β-W are reported to have some of the largest spin Hall angles, 0.12-0.15 [67], 0.12 [68] and 0.30-0.40 [69–71], respectively.

1.4 Thesis at a Glance

This report frames the attempts towards understanding the DMI of different material stacks and evaluation process for the Dzyaloshinskii-Moriya interaction. Some fundamental concepts such as different magnetic anisotropies, DW type in PMA systems, their chirality and motion regimes will be introduced firstly. Then details of DMI evaluation using different techniques will be explained. Then the experimental methods for deposition and characterization of the samples will be described in chapter 3.

The obtained results are separated into three parts, each regarding to a set of samples and their related measurements and progression. The first (Chapter 4) is on trilayers of Pt\Co\$\mathrm{Au}_x\mathrm{Pt}_{1-x}$ which are epitaxially grown on C-plane Sapphire. Confirming their epitaxial texture using TEM and XRD, the strength of DMI using bubble expansion is estimated and field and current induced DW motion is investigated.

Chapter 5 focuses on polycrystalline multilayers of Pt\Co\Ir(x)\Ta, changing the thickness of Ir. The magnetization characterization and confirmation of Ta β-phase will be stated. Then, field induced DW progression in different motion regimes will be studied and its parameters are explained. Afterwards, DMI on these multilayer systems are investigated using Brillouin light scattering (BLS) spectroscopy and asymmetric bubble expansion techniques. The results will be compared with micromagnetic

simulations of the same system. At last, shortcomings of the theory to explain bubble expansion will be discussed. Also, some arguments on DMI sign of Ir\Co interfaces are detailed.

The last chapter on the results (Chapter 6) is describing the deposition characterization and DMI evaluation of polycrystalline Pt\Co\Hf(x)\Ta. Here also, DMI will be investigated using asymmetric bubble expansion and BLS. The effect of Hf insertion will be discussed and compared to the reports in literature.

Last, a summary of the key points will be given in chapter 7, along with possible future directions of this project.

Chapter 2

Theoretical Background

2.1 Introduction

In this chapter some of the theoretical concepts underpinning experimental observations in this thesis, will be explained. Firstly, the basic of ferromagntism, exchange interaction will be briefly explained. Afterwards, different types of magnetic anisotropy will be described as the main feature of all the sample systems in this work. Then, the details of domain wall behaviour and its motion will be set out. Lastly, the Dzyaloshinskii-Moriya interaction and observation using asymmetric bubble expansion and Brillouin light scattering will be discussed.

2.2 Exchange Interaction and Ferromagnetic Ordering

The Pauli exclusion principle rules that two electrons cannot have the same quantum state. As electrons are fermionic indistinguishable particles, this means that their total energy wave function should be anti-symmetric. In such a case, two electrons with parallel spins cannot occupy the same space, which is in favour of their Coulomb repulsion. This reduction of energy for parallel spin configuration leads to Hund's first rule. Heisenberg's generalized exchange interaction Hamiltonian for a many-electron lattice can be written as

$$H_{\text{ex}} = -\sum_{i \neq j} J_{ij} \vec{S}_i . \vec{S}_j \tag{2.1}$$

where $\vec{S}_i$ and $\vec{S}_j$ are spin angular momentums of two sites of the lattice and J_{ij} is the exchange coupling strength between them. If just neighbouring sites are counted then J is a single constant for the material. This assumption is often true as the exchange is a short-range interaction that reduces rapidly with distance.

If $J > 0$, then the minimum energy configuration happens when spins are collinear and parallel. Such material is called *ferromagnetic* and displays spontaneous magnetization. For $J < 0$ anti-parallel spins are preferred and *antiferromagnetism* is observed. It should be noted that the picture is not always as simple as this, and very much depends on the symmetry of the lattice structure and value of exchange integral.

For continuous magnetization the exchange energy is approximated as

$$E_{\text{ex}} = -\int_V A \left[(\nabla m_x)^2 + (\nabla m_y)^2 + (\nabla m_z)^2 \right] dV \tag{2.2}$$

where $m_{x,y,z}$ are different components of the magnetization, V the volume of the magnetic material and A the exchange stiffness and temperature dependent. For materials

with simple lattice, A is defined as $A \sim JS^2Q/a$, where Q is the number of atoms per unit cell (1 for simple cubic, 2 for body-centered cubic (BCC) and 4 for face-centered cubic (FCC) structures), S is the spin number and a is the lattice constant.

2.3 Magnetic Anisotropy

When a magnetic field is applied to a magnetic material, there will be a certain field when all the moments in the material are aligned with the externally applied field. The material in this condition is usually referred as *magnetically saturated*. If the needed field to saturate the material is dependent on the direction, then the material is known to have *magnetic anisotropy*. In this way, the material needs smaller applied field to reach the saturated state along its *easy axis* rather than the *hard axis*. This phenomenon is very important for different applications. For example permanent magnets are made from materials with large magnetic anisotropy, while magnetic sensors are preferred to have a very low anisotropy [72]. There are different components to the anisotropy depending on its origin. A few of them will be discussed in this section.

2.3.1 Magnetocrystalline Anisotropy

Crystalline anisotropy happens when the energy it takes to magnetize the material is dependent on the crystalline axes [2]. In 1929, Akulov showed that magnetocrystalline anisotropy is dependent on the angle between magnetization and a specific crystalline axis, θ [73] and for a cubic material is given by [2]

$$E_{cubic} = K_0 + K_1({a_1}^2{a_2}^2 + {a_2}^2{a_3}^2 + {a_3}^2{a_1}^2) + K_2({a_1}^2{a_2}^2{a_3}^2) + ... \tag{2.3}$$

where a_i is the cosine of θ, and K_0, K_1, K_2, *etc.* are the successive orders of anisotropy constant, which are material and temperature dependent. Anisotropy constants are usually decreasing with temperature and reach zero at Curie temperature, T_C [2]. The origin of magnetocrystalline anisotropy is spin-orbit coupling. In simple words, if an external energy/force tends to rotate the spin (*magnetization rotation*), the spin-orbit coupling relates it to the orbit. The strong coupling between orbital motion of electrons and the crystalline lattice make this rotation costly. As a result, the cost (*i.e.* energy) of rotation of the magnetization will become dependent on the crystalline axes [2].

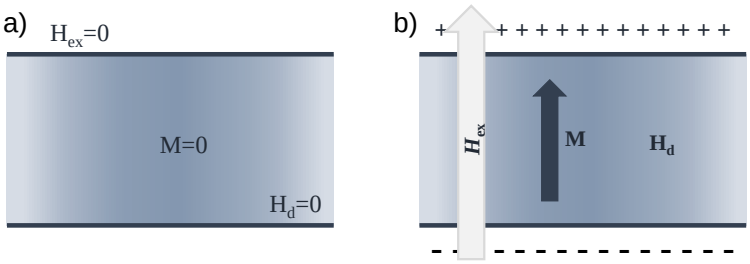

Figure 2.1: Demagnetizing Field in a thin film when: a) there is no external field applied, and the sample is not magnetized, b) with external field.

2.3.2 Shape Anisotropy

Shape anisotropy is related to the geometry of the sample [2] and is the result of the magnetostatic interactions between magnetic dipoles. When spins of the material are uniformly aligned, magnetic charges appear on opposing surfaces of the sample (Figure 2.1). These charges induce an internal magnetic field that opposes the external applied field and is known as the demagnetizing field [74]. The present dipolar interaction is stronger whenever this demagnetizing field, H_{D} is along the shortest dimension of the sample. As a result, for a spherical sample there will be no preferred direction. For magnetic thin film, it usually means that the magnetisation preferentially lies in the plane of the film [2]. This internal field, interact with magnetization and leads to an energy term. The demagnetizing enegry (also called magnetostatic energy) is defined as

$$\varepsilon_{\mathrm{d}} = -\frac{1}{2}\int \mu_0 \vec{H}_{\mathrm{D}} \cdot \vec{M} dV \tag{2.4}$$

where V is the volume of magnetic material. This demagnetizing energy, in turn, results in shape anisotropy energy density which is defined as [75]

$$K_{\mathrm{shape}} = \frac{\mu_0}{4}(1-3N)M_{\mathrm{S}}^2 \tag{2.5}$$

where μ_0 is the vacuum permeability, M_{S} is the saturation magnetization and N is the demagnetizing factor which is dependent on the sample geometry. For thin films, $N = 1$, thus the $K_{\mathrm{shape}} = -(1/2)\mu_0 M_{\mathrm{S}}^2$.

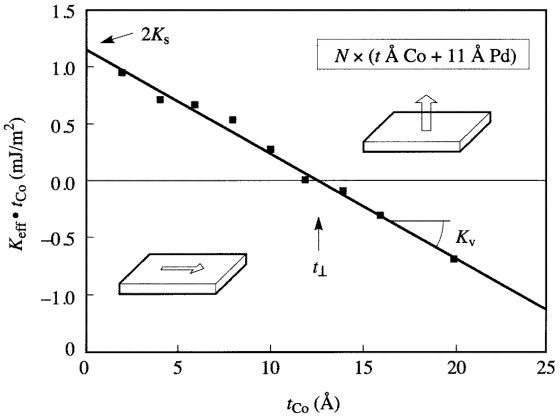

Figure 2.2: Effective anisotropy times the individual Co layer thickness vs. the individual Co layer thickness of Co/Pd multilayers. The y-intercept equals twice the interface anisotropy, while the slope gives the volume contribution [78].

2.3.3 Perpendicular Anisotropy

Opposing to what was stated in the previous part, in some thin films the easy-axis does not lie in the plane of the sample. Néel suggested that this rotation of easy axis to the perpendicular direction originates in the symmetry reduction at the interface [76].

In a thin film generally all shape, magnetocrystalline, and interface anisotropies are playing a role, so it is important to differentiate between surface and volume contributions to the anisotropy. Gradmann and Müller defined the anisotropy energy density between the film and its normal axis as [72, 77]

$$K_{\text{eff}} = \frac{2K_{\text{s}}}{t_{\text{FM}}} + K_V \tag{2.6}$$

where K_{eff} is the effective anisotropy density, K_{V} the volume contribution, K_{s} the surface contribution, and t_{FM} the thickness of the ferromagnetic material. Equation 2.6 indicates that K_{eff} inversely depends on the t_{FM}. So, if plotting $K_{\text{eff}}t_{\text{FM}}$ as a function of t_{FM}, as figure 2.2 presents, K_{s} and K_{V} will be half of the intercept and slope of the fitted line, respectively [78]. The balance between the surface and volume components determines the strength and direction of the magnetic anisotropy. Hence, for $t_{\text{FM}} < t_\perp = -2K_{\text{s}}/K_{\text{V}}$ the system would exhibit perpendicular magnetic anisotropy.

The very first report of PMA was in Co/Pd sputtered multilayers with $t_{\text{Co}} < 0.8$ nm in 1985 [79]. In general, Co\X thin films, where X=Pt, Pd, Au, Ir, Ni, *etc.* are known

to exhibit perpendicular magnetic anisotropy. In these systems, the out-of-plane $3d$ orbitals experience the symmetry breaking, which leads to changes in their band energy. Also, the $3d$ orbitals hybridize with their neighbouring $5d$ bands of the X heavy-metal. This interfacial symmetry breaking and hybridization are the most important origin of the PMA. Nevertheless, there are other factors like interface sharpness [80], degree of (111) texture [81], defect density [82] *etc.* that will change the K_s/K_V ratio, thus strength of PMA.

2.4 Domain Walls

Domain wall in magnetic materials usually refers to an interface for which the magnetization of two neighbouring domains gradually changes from one direction to another. In perpendicularly magnetized systems, it usually undergoes a π rotation. In a uniaxial system there is a competition between magnetic (uniaxial) anisotropy and exchange interaction. While the exchange interaction wants to keep adjacent spins parallel, magnetic anisotropy wants them aligned with a certain direction. In this way, the former wants to widen the domain wall (less change of magnetization direction between two neighbouring spins) and the latter would like it narrower (less volume in which magnetization is not parallel to easy axis). A balance between these two effects results in a certain width of the domain wall as follows:

$$\Delta = \sqrt{\frac{A}{K_{\text{eff}}}} \tag{2.7}$$

where A is the exchange stiffness, and K_{eff} is anisotropy energy.

2.4.1 Different Domain walls in PMA Structures

In PMA thin films there are two types of spin structures for the DW: Bloch and Néel wall [83, 84]. In Bloch domain walls (BW) the spins are rotating around the normal to the DW so that the magnetization in the middle of the DW is parallel to the DW plane. Néel wall (NW) magnetization, on the other hand, is perpendicular to the DW plane and the spins are rotating around the in-plane direction of the DW (Figure 2.3).

It was believed that the DW ground state in all ultra-thin ferromagnetic structures is BW [85] as the Néel structure introduces surface charges at the wall face. This causes a demagnetizing filed, hence a greater energy cost to create Néel type [2]. In 2010 it

was shown that BWs are unstable in perpendicular magnetized thin films and Néel wall was observed in magnetic bilayers [86]. The Néel wall was firstly suggested by Louis Néel in 1955 [84] and it was seen in in-plane magnetized thin films when the thickness of the film was less than the thickness of the DW (*e. g.* $t_{\mathrm{FM}} < 40$ nm in Permalloy) [2], but for the case of PMA films, it is Dzyaloshinskii-Moriya interaction that overcomes the energy cost.

2.4.2 Domain Wall Chirality

One of the important aspects of DW motion control is the DW chirality. In PMA ferromagnetic materials the stabilized Bloch or Néel walls can be left-handed (counter-clock-wise) or right-handed (clock-wise) chiral as it is illustrated in figure 2.3. In this way, a chirality vector can be defined as $\langle \vec{m}_i \times \vec{m}_{i+1} \rangle / |m|^2$, where $\vec{m}_{i+1}$ and $\vec{m}_{i+1}$ are adjacent moments in the wall moving from up to down DW. The direction of this vector is shown in the figure 2.3 for clockwise and anticlockwise Bloch and Néel walls.

Bloch walls usually have a combination of both chiralities, but homochiral Bloch walls were also reported [87]. For the Néel walls, the chirality of the DW is fixed by the Dzyaloshinskii-Moriya interaction which usually arises from the interface of the ferromagnetic ultra-thin layer with a heavy-metal [28]. It should be noted that these structure are two extremes of domain wall configuration, and more often than not a

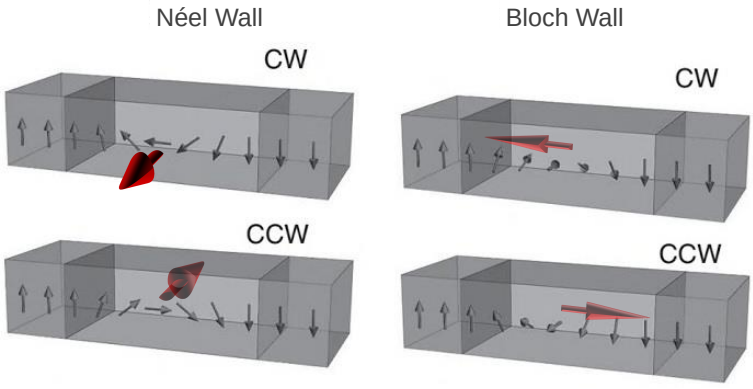

Figure 2.3: Different structure of DWs in PMA material, Néel and Bloch wall, where each can possess a chirality depending on the direction of their magnetization rotation. The chirality vector is shown by red vectors in the related wall configuration.

combination of the two appears in the system. This can be understood by rotating the chirality vector in figure 2.3.

The DMI usually manifests itself as an intrinsic in-plane field inside the domain wall and perpendicular to its plane, which forces the DW magnetization to have a certain chirality throughout the film. This homochirality of the film will be desirable in current induced DW motion, as in such a system all the DWs should move in the same direction.

2.4.3 Domain Wall Motion

DWs are commonly considered as a 1D elastic interface moving in a 2D weakly disordered medium [1]. Disorder in this medium is usually described as a pinning disorder which competes with elasticity of the moving interface (*i.e.* DW), causes roughness in it and modifies the dynamics specially when the driving force (magnetic field or spin current in the case of DWs) is small. At zero temperature, there is a threshold force, *depinning force*, f_{d}, for which the elastic line could overcome the pinning barrier and start motion (Figure 2.4). Far from the depinning transition, $f \gg f_{\mathrm{d}}$, the *flow regime* would occur which is independent of the pinning force, limited by dissipation and depends on microscopic structure of the DW [88].

For finite temperatures, however, a thermally activated motion arises at $f < f_{\mathrm{d}}$, known as the *creep regime*, wherein DW's velocity follows on Arrhenius law,

$$v \sim \exp(-\Delta E/k_{\mathrm{B}}T) \tag{2.8}$$

where ΔE is the pinning barrier, T is temperature and k_{B} is the Boltzmann constant. This is depicted in figure 2.4. It is mentioned in various reports that when the medium has a weak correlated short-range disorder and the driving force is very low (*i.e.* $f \to 0$) ΔE changes with $f^{-\mu}$ where $\mu = -\frac{1}{4}$ [89–91]. μ is called the "creep exponent". Metaxas *et al.* [88] stated that the creep formula for DW propagation is valid not just for $H \ll H_{\mathrm{d}}$ ($f = H$ for field driven DWs) but also for higher fields very close to depinning field, H_{d}. Recently, it was shown that creep regime follows a universal pattern for the

[1] This assumption is not true when the driving force is large and DW does not see the pinning of the background matrix, namely when it is not moving in creep regime, which will be discussed later in the chapter.

whole range of $0 < H < H_d$ and can be described by [91, 92]:

$$v(H,T) = v(H_\mathrm{d},T)\exp\left(-\frac{\Delta E}{k_\mathrm{B}T}\right) \tag{2.9}$$

with

$$\Delta E = k_\mathrm{B}T_\mathrm{d}\left(\left[\frac{H}{H_\mathrm{d}}\right]^{-\frac{1}{4}} - 1\right) \tag{2.10}$$

where T_d is the characteristic pinning energy scale and $v(H_\mathrm{d},T)$ is the depinning velocityr. They [92] emphasize that equation 2.9 is a universal function for describing the creep regime, independent of the material in use and leads to unique pinning energy barrier function, $\Delta E(H) = k_\mathrm{B}T\ln[v(H_\mathrm{d},T)/v(H,T)]$. The only non-universal material and temperature-dependent parameters are depinning field H_d, velocity at the depinning field $v(H_\mathrm{d},T)$, and depinning temperature T_d which are in turn coming from the microscopical origin of pinning. It is also clear that increasing the field to the point where $H \to H_\mathrm{d}$ fades the energy barrier ($\Delta E \to 0$). Moreover, for the lower extreme of $H \to 0$ equation 2.10 still returns the original creep law: $v = v_0\exp\left[\left(\frac{T_\mathrm{d}}{T}\right)\left(\frac{H}{H_\mathrm{d}}\right)^{-\frac{1}{4}}\right]$ [89].

As stated above, close to depinning field the pinning barrier disappears gradually and levels with the thermal activation energy. Thereafter, the velocity is an integrated function of temperature and driving field. At the depinning transition point the curve experiences a *"thermal rounding "* [93] with:

$$v(H_\mathrm{d},T) = v_T\left(\frac{T}{T_\mathrm{d}}\right)^{\psi} \tag{2.11}$$

and field-induced changes in the velocity follows

$$v(H, T \ll T_\mathrm{d}) = v_H\left(\frac{H-H_\mathrm{d}}{H_\mathrm{d}}\right)^{\beta} \tag{2.12}$$

where $\psi = 0.15$ [91, 93, 94] is the thermal rounding exponent, $\beta = 0.25$ [95] is the depinning exponent, and v_T and v_H are depinning velocities [94]. For most of experiments on magnetic materials the experimental temperature is much lower than depinning temperature, T_d, hence field dependent changes dominate in the velocity just above the depinning field, $H \geqslant H_\mathrm{d}[1 + (0.8 \times (\frac{T}{T_\mathrm{d}})^{\psi})^{\frac{1}{\beta}}]$. Then, the generalized homogeneous velocity function will be

$$v(H,T) = \frac{v_\mathrm{T}(H_\mathrm{d},T)}{x_0}\left(\frac{H-H_\mathrm{d}}{H_\mathrm{d}}\right)^{\beta} \tag{2.13}$$

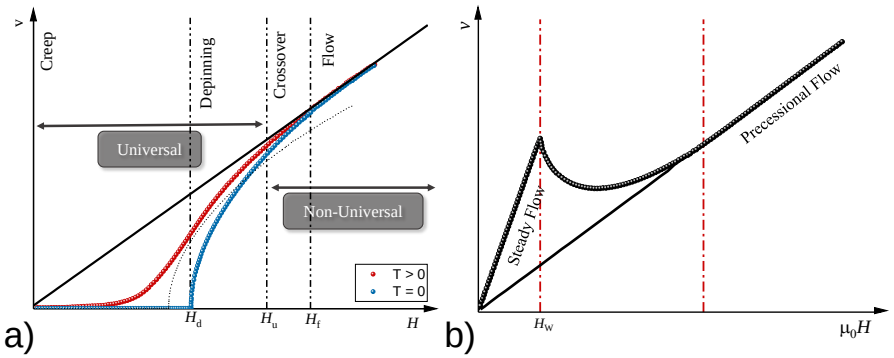

Figure 2.4: a) Changes in velocity of an elastic interface in a weakly disordered medium. This shows different regimes that DW goes through at zero and finite temperatures. For $T > 0$ when driving force is less than depinning force, a thermally activated motion known as creep regime would occur. Higher than H_d the pinning barrier tends to zero and driving force and temperature play the main role up to a upper limit of H_u, after which there is a non-universal crossover for the DW to reach the flow regime. b) In a perfect magnetic system DWs experience two different flow regimes with a crossover region with negative slope. The magnetization direction of the DW remains stable in steady regime up to Walker field, H_W and is precessing throughout the linear regime of precessional flow. The solid line shows the linear extrapolation of observed flow regime. (Figure is a reproduction from [88])

where $x_0 = 0.65 \pm 0.04$ is dimensionless amplitude ratio of the depinning velocities, v_T/v_H and material and temperature independent [94]. This function also was proved to have a universal behaviour [94], wherein there are only 3 material and temperature-dependent parameters which are the same parameters as in creep universal function: depinning temperature T_d, depinning field H_d and velocity at the depinning field $v(H_\mathrm{d}, T)$.

The universal behaviour of depinning has an upper limit, H_u, after which DW usually passes a non-linear intermediate course to reach to flow motion. As mentioned, DW velocity in the flow regime is limited by dissipation. Here dissipation can be described by damping factor, α, which is estimated from domain wall mobility, m, depending on which flow regime is observed. For a DW moving in a perfect medium with no disorder and in low fields, DW proceeds into the magnetic medium with no change in its magnetization direction. In this *steady regime* DW's velocity changes

linearly with the field, $v = mH$ with

$$m = \frac{\gamma\Delta}{\alpha} \tag{2.14}$$

where γ is the gyromagnetic ratio, Δ DW width, and α the Gilbert damping factor [88].

After a field known as Walker (breakdown) field, H_{W}, the internal dynamics of the DW breaks down and velocity-changes with the field becomes negative. Well above H_{W}, DW regains its stability and experiences a second linear flow regime in which the magnetization precess and its mobility is [88]

$$m = \frac{\gamma\Delta}{\alpha + \alpha^{-1}} \tag{2.15}$$

In a disordered medium, on the other hand, the Walker field is usually less than the depinning field, thus the steady regime is hidden in the creep regime. This limits observation of steady flow regime to materials with very low pinning potential. The very first experimental results on linear flow regime were reported by Metaxas *et al.* where in fact they concluded that the motion was in the precessional flow regime [88].

2.5 Dzyaloshinskii-Moriya Interaction

The structure of domain walls are usually determined as a result of exchange interaction, magnetic anisotropy and dipolar interaction, *e.g.* in systems with perpendicular magnetic anisotropy the wall structure is usually Bloch as it is predicted to be the lowest energy condition [96]. But, this domain wall texture cannot be theoretically attributed to current-induced domain wall motions with velocities as high as 400 m/s in some PMA systems [97, 98]. One can change the wall texture to Néel with a fixed chirality by applying a high enough in-plane magnetic field [99].

Apart from this external modification of the wall type, there is some intrinsic effect that can be useful in this matter. If the system had inversion symmetry, as a result of symmetric exchange interaction the left-handed and right-handed DWs would have degenerate energy states. But, in systems where inversion symmetry is broken, the exchange energy would be no longer invariant in both sides and in presence of spin-orbit coupling a Dzyaloshinskii-Moriya interaction term would be introduced to system. This added term to the free energy can split the left and right hand degenerate energy

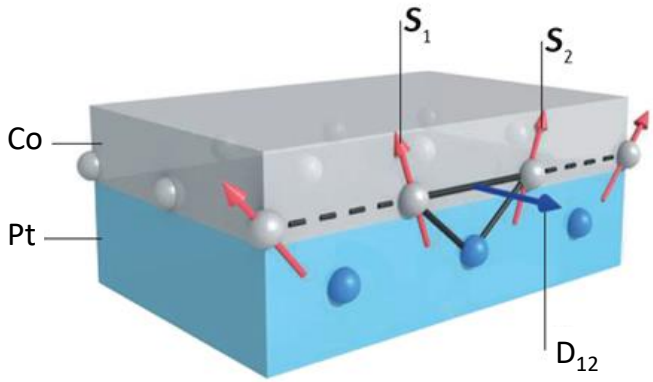

Figure 2.5: Schematic of the Dzyaloshinskiiâ€“Moriya interaction (DMI) at the interface between a magnetic film and a heavy metal [100] .

states [23, 24] and can be written as

$$E_{\mathrm{DM}} = -\frac{1}{2}\sum_{ij} \vec{D}.(\vec{S}_i \times \vec{S}_j) \tag{2.16}$$

where $\vec{D}_{ij}$ is DM vector and $\vec{S}_i$ and $\vec{S}_j$ are spin vectors of the two adjacent spins.

In ultra-thin films with PMA, if the layers on bottom and top of the FM are not similar, then the symmetry is broken perpendicular to the sample plane. If we consider a nano wire for which x axis lies on the direction of the wire, and define the z axis as the normal to the plane of the film, then the interface DMI is [11]

$$\begin{aligned} E_{\mathrm{DM}} &= D\left[m_z\frac{\partial m_x}{\partial x} - m_x\frac{\partial m_z}{\partial x}\right] + D\left[m_z\frac{\partial m_y}{\partial y} - m_y\frac{\partial m_z}{\partial y}\right] \\ &= D\left[m_z\boldsymbol{\nabla}\cdot\vec{m} - (\vec{m}.\vec{\nabla})m_z\right] \end{aligned} \tag{2.17}$$

where m_i are different components of magnetization.

As stated before, DMI in thin films is usually simplified as an intrinsic in-plane field inside the DW described as $H_{\mathrm{DMI}} = D/\mu_0 M_{\mathrm{S}}\Delta$ (where Δ is domain wall width). This internal field would act like the mentioned external in-plane field and if the interaction is big enough, it overcomes the shape anisotropy and changes the domain wall ground state from Bloch wall to homochiral Néel wall in PMA systems [101]. Any parameter that can make a change in symmetrical properties may affect DMI. This includes asymmetric metal composition, asymmetric crystal structure [102], asymmetric induced magnetic moment [42], or asymmetric interface properties like roughness, intermixing and density of stacking faults [12, 40].

2.5.1 Measuring DMI

The most important aspect of any phenomenon is human's ability to measure the effect easily and reliably. Several different methods have been used to evaluate the strength of the DMI, D. Current driven domain wall motion under in-plane (InP) applied field has been strongly investigated [10, 16, 30, 46]. But using current to study DMI complicates the situation as usually spin Hall effect, Rashba, and DMI are present simultaneously and needs determination of exact strength of different torques applied on the DW [103]. Also precise calculation of the current flow in the HM layer is another problem [57]. Furthermore, 1D modelling attempt to describe the motion in these cases does not always represent the true experimental condition. So, evaluating DMI using current based measurements includes experimental and theoretical complications and might bring large uncertainties. Microscopy measurements such as spin-polarized scanning tunnelling microscopy [104], spin-polarized low-energy electron microscopy [101], and photoemission electron microscopy combined with x-ray magnetic circular dichroism [105] can also be used, but these techniques are expensive and very time consuming. Brillouin light scattering uses non-reciprocal propagation of the spin waves in materials with DMI to measure D, at the same time it requires very specialized equipment [106, 107]. DW dynamics induced by magnetic field can also be used for determination of DMI strength. In the methods that are based on DW dynamics in flow regime, the large applied field deforms the internal structure of the DW and affect their dynamics [108]. Estimation of DMI using asymmetric bubble expansion with creep velocities [12, 109] is also widely adopted since it requires minimal sample preparation and relatively inexpensive equipment to implement. In this work, asymmetrical bubble expansion (by the author) and BLS (by collaborators in National Institute of Standards and Technology) were used to investigate the DMI strength, so in the following sections the procedures of these measurements are going to be discussed in more detail.

2.5.2 Asymmetrical Bubble Expansion

The effect of in-plane field on asymmetric enlargement of bubble domain has been investigated decades ago [110, 111] but never attributed to DMI until 2010. To my knowledge, Kabanov *et al.* were the first ones to mention DMI as one of the probable reasons for elongated domains in the presence of an in-plane field, which they stated that "may form phases with *different* spin chirality"[112]. Whereas it is now known that DMI

actually forces structures (DWs or skyrmions) with the *same* chirality throughout the material [113]. This, in turn, causes the asymmetrical propagation of bubble domains in PMA materials under influence of an in-plane magnetic field.

In 2013, Je *et al.* [109] added DMI and Zeeman energy terms to the domain wall energy density formula and tried to estimate DMI strength in multilayers of Pt\Co\Pt, a technique which was modified by Hrabec *et al.* [12] soon after. It is obvious that if a PMA system has bubble magnetic domains, a pulsed OoP field will cause symmetrical expansion of the domains. In the aforementioned process, a constant applied in-plane field will be added which changes the domain wall energy, σ_{DW}, in addition to DMI, mostly for the wall which is normal to the applied InP field.

Je *et al.* argued that if the domain wall motion follows the creep regime then the DW velocity is

$$v = v_0 \exp(-\zeta H_z^{-\mu}) \tag{2.18}$$

where v_0 is the characteristic speed, ζ is a scaling constant and μ is creep scaling exponent, which is 1/4 [114, 115]. In their formulae ζ is scaling coefficient and can be expressed as

$$\zeta = \zeta_0 [\sigma(H_x)/\sigma(0)]^{1/4} \tag{2.19}$$

where ζ_0 is scaling constant and σ is DW energy density which is dependent on the

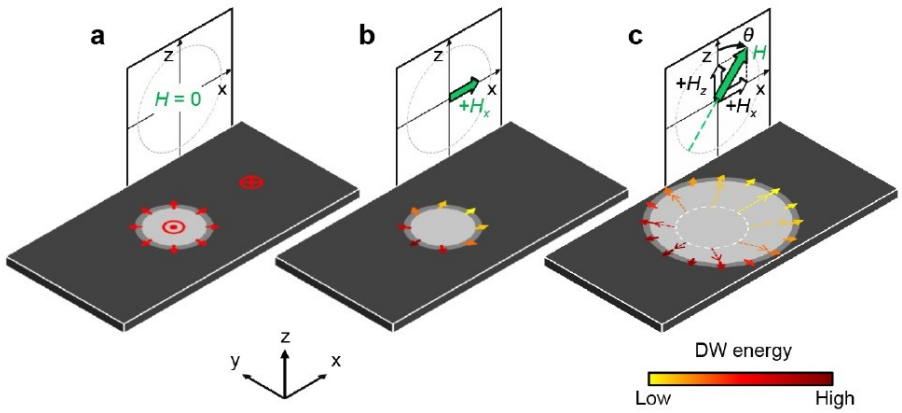

Figure 2.6: a) Symmetrical expansion of a bubble domain just applying OoP field. b) Change of the Néel DW energy when an InP field is applied. c) Asymmetrical expansion of bubble domain in presence of DMI, InP and OoP field [43] .

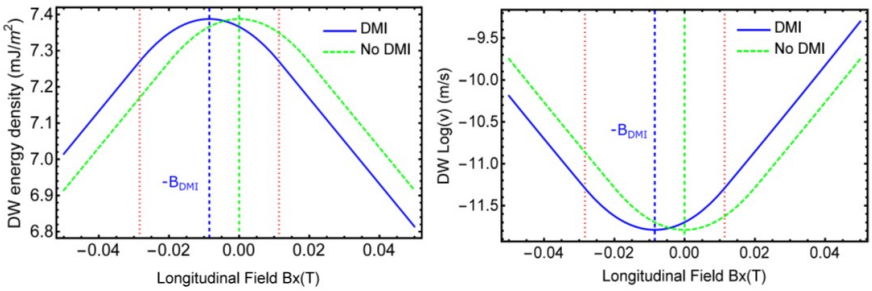

Figure 2.7: a) Changes of DW energy density in absence and presence of DMI when an in-plane field is applied on the DW, simulated from Je's formula [109]. When there is no DMI, DW energy peaks at zero in-plane field and will reduce symmetrically for opposite field directions. When DMI is present the peak in DW energy is shifted to a lower/higher value depending on the DMI sign. b) Changes in DW energy reflects into DW velocity. Minimum point in this graphs is where $H_{\mathrm{DMI}} = -H_{\mathrm{InP}}$. (Graph is courtesy of Simone Morreti)

applied in-plane magnetic field [11] as follows

$$\sigma_{\mathrm{DW}}(H_x) = \begin{cases} \sigma_0 + \frac{\pi^2 \Delta {M_{\mathrm{S}}}^2}{8K_{\mathrm{D}}}(H_x + H_{\mathrm{DMI}})^2, & : \text{if} |H_x + H_{\mathrm{DMI}}| < \frac{4K_{\mathrm{D}}}{\pi M_{\mathrm{S}}}. \\ \sigma_0 + 2K_{\mathrm{D}}\Delta - \pi\Delta M_{\mathrm{S}}|H_x + H_{\mathrm{DMI}}|, & : \text{otherwise}. \end{cases} \tag{2.20}$$

in which the top term is in the case that $H_x + H_{\mathrm{DMI}}$ is not big enough to transform the wall configuration from Bloch to the Néel. In equation 2.20, $\sigma_0 = 4\sqrt{AK_{\mathrm{eff}}}$ is the Bloch DW energy, M_{S} is the saturation magnetization, K_{D} is the DW anisotropy energy density, Δ is the DW width, and H_x and H_{DMI} are applied in-plane field and DMI field, respectively.

Changing the wall energy, the in-plane field breaks the radial symmetry of the creep velocity, while the OoP field would drive the domain wall to be creeping. If the DW is a Néel wall, then the second line of eq. 2.20 should be considered. Hence, wherever $H_{\mathrm{DMI}} = -H_{\mathrm{InP}}$ the wall energy is maximum, therefore propagation has a minimum velocity (Figure 2.7). So, having the DW velocity for different in-plane fields, the minimum of velocity vs. H_{InP} can be used to calculate DMI factor:

$$D_{\mathrm{eff}} = \mu_0 H_{\mathrm{DMI}} M_{\mathrm{S}} \Delta \tag{2.21}$$

where D_{eff} is the effective DMI factor and domain wall width $\Delta = \sqrt{A/K_{\mathrm{eff}}}$.

This magnetic driven wall motion method has at least two advantages over current based measurements. For one, it can be applied to sheet films and no patterning or electrical contact is needed. Secondly, as it is not current based no Rashba, spin Hall effect or heating are present, hence less contributing parameters.

2.5.3 Brillouin Light Scattering (BLS)

Brillouin light scattering mainly refers to inelastic scattering of light (photons) with low frequency vibrations in material which can be either thermally generated acoustic vibrations (phonons) or disturbances in magnetic ordering (spin-waves/magnons). It is named after Léon Nicolas Brillouin who first published "*Diffusion of light and x-rays by a transparent homogeneous body*" in 1922 [116]. However it is believed that Leonid Mandelstam discovered the scattering earlier in 1918, but did not publish it until 1926 [117]. In this work we are focusing on magnon/spin-wave (SW) scattering.

In BLS spectroscopy, the sample is usually irradiated with a laser beam, which interacts with magnons in the material. Momentum and energy conversion dictate that a magnon propagating towards the laser light should be annihilated and as a result the backscattered photon would have higher energy/frequency (anti-Stokes scattering). On the other hand, the magnon propagating from the laser beam is created and the related backscattered photon has lower energy/frequency (Stokes scattering). So, measuring the energy of backscattered photon, one could derive the frequency of propagated SWs.

In 2013, Moon [118] formulated SW dispersion relations in the presence of the interfacial Dzyaloshinskii-Moriya interaction for a uniformly in-plane magnetized structure. It states that SW dispersion relation would have a term which is linearly proprtional to SW's wave-vector, k and DMI factor, D. Consequently, it causes an antisymmetric SW propagation which depends on both SW propagation direction and the magnetization polarity [118]. This, in turn, results into a non-reciprocal frequency shift in Stokes and anti-Stokes peaks as it is shown in figure 2.8. This DMI-influenced frequency shift is [106]:

$$\Delta f_{\mathrm{DMI}} = \left| \frac{g^{\parallel} \mu_{\mathrm{B}}}{h} \right| \mathrm{sgn}(M_z) \frac{2D}{M_{\mathrm{S}}} k_x \tag{2.22}$$

where $g^{\parallel}$ is in-plane splitting factor, μ_{B} is Bohr magneton, h is Planck's constant, M_{S} is saturation magnetization and k_x is wave number of the spin waves.

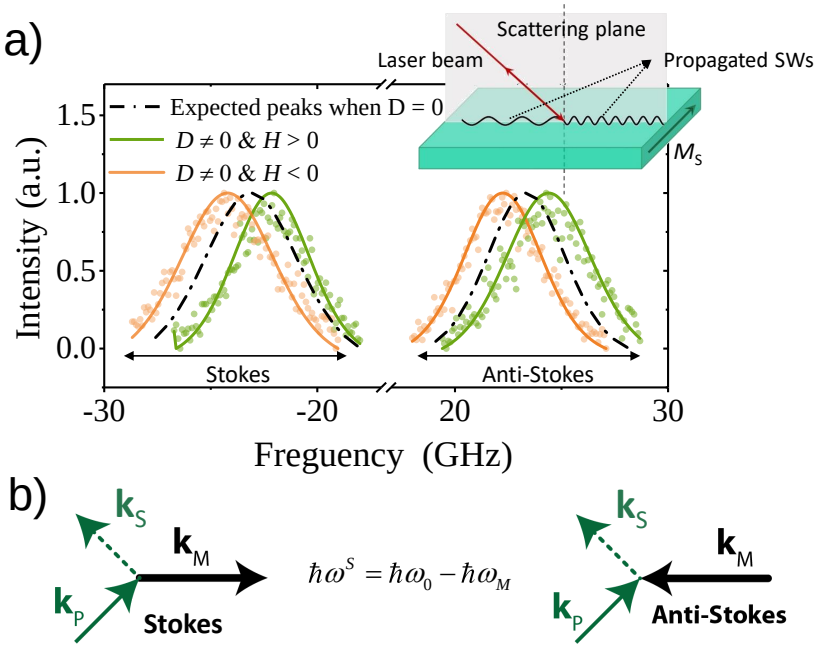

Figure 2.8: a) Normalized BLS spectra measured for Pt\Co\Ir at two opposite applied fields in orange and green. The black dashed line shows what is expected in case there is no DMI in the sample where Stokes and anti-Stokes frequency are the same. As it is depicted, there will be a frequency shift for Stokes and anti-Stokes peaks when DMI is present and the shift changes sign with magnetization. Symbols refer to experimental data and solid lines are Lorentzian fits. The inset represents Damon-Eshbach geometry which was used for measurements presented in this work. b) Momentum, and energy exchange for Stokes and anti-Stokes interactions. K_{P} is momentum of the polar incident light, K_{M} the magnon momentum, and K_{S} momentum of the scattered light.

2.6 Summary

In this chapter, the background physics of ferromagnetic thin films with PMA and their domain walls was explained to understand their behaviour in multilayers of this work. Ferromagnetic configuration of the FM layer occurs as the result of Pauli exclusion principle and Coulomb interaction. The PMA anisotropy in these films arises from competition between magnetocrystalline, shape and interface anisotropies. Domain walls can acquire Néel or Bloch characteristics with different chiralities depending on internal (DMI) or external fields applied locally. Their width and energy, also, is as

result of a balance between exchange and anisotropy. Moreover, DW dynamics can offer us a lot of insight in the material, structure and temperature related parameters which are crucial for further engineering of devices based on DW motion.

Chapter 3

Experimental Methods

3.1 Introduction

This chapter briefly details the sample fabrication procedures and characterisation methods that have been used in the present work. In short, polycrystalline and epitaxial multilayers were deposited on thermally oxidised Silicon (100) wafers and polished Sapphire (0001) substrates, respectively, using direct current (DC) magnetron sputtering. Growth rate measurements and basic characterisation of the samples have been done by the two most common x-ray methods: X-ray reflectivity (XRR) and X-ray diffraction (XRD). Also, cross sectional transmission electron microscopy imaging was used for structural, and topographical study of the samples. Then, magnetic properties were investigated by means of polar magneto-optic Kerr effect (MOKE) and superconducting quantum interference device vibrating sample magnetometry (SQUID-VSM). Some thin films were also patterned into wires using elctron beam and optical lithography processes. All the preparation above is to support investigation of interfacial magnetic properties, which here mostly includes study of domain wall motion and Dzyaloshinskii-Moriya interaction.

3.2 Sample Fabrication and Basic Characterisation

3.2.1 DC Magnetron Sputtering

A magnetron sputtering system is usually used for depositing magnetic multilayers. To do so, first the substrates are cut into 8 mm ×8 mm pieces (if needed) and cleaned in acetone and IPA using an ultrasonic bath (5–10 minutes each), then dried with air or N_2 before mounting in a vacuum chamber.

Polycrystalline Ta\Pt\Co\Ir\Ta and epitaxial Pt\Co\Pt_xAu_{1-x} multilayers have been deposited in a custom designed Kurt J. Lesker sputtering system equipped with 10 targets - including 4 magnetic and one RF sputtering - and able to deposit 24 samples in the same vacuum cycle (Figure 3.1). Multilayer growth is possible through using double sample and target shutters and a rotating substrate wheel. The base pressure can go down to 6×10^{-8} Torr using roughing and cryo-pump, successively also benefiting from liquid Nitrogen cooling system (so-called Meissner trap). A residual gas analyser (RGA) also can be employed to differentiate between partial pressure of different atoms or molecules. Polycrystaline Ta\Pt\Co\Hf\Ta multilayers have been sputtered in Singulus Technologies Multi-Target-Module (MTM) sputtering machine

Figure 3.1: The Kurt J. Lesker sputtering system showing substrate wheel.

with 10 DC/RF Cathodes in which base pressure is better than 1×10^{-8} Torr.

In general, once the pressure is low enough in a sputtering chamber, argon gas with a partial pressure (here about 2.8 mTorr) will be introduced into the system. Controlling the system with a built-in software, a negative potential will be applied to the target. An Ar plasma forms and Ar^+ ions accelerate towards the target and bombard it, causing the target to eject atoms and free electrons. The ejected atoms will coat any surface around and extra electrons feed the formation of Ar^+ ions and help continuation of the plasma. As figure 3.2 demonstrates, magnets underneath the target produce a magnetic field that confines plasma (Ar^+ ions and electrons) in a specified region on top of the target, prevent electrons striking the substrate, moreover enhancing probability of electron-Ar^+ interaction.

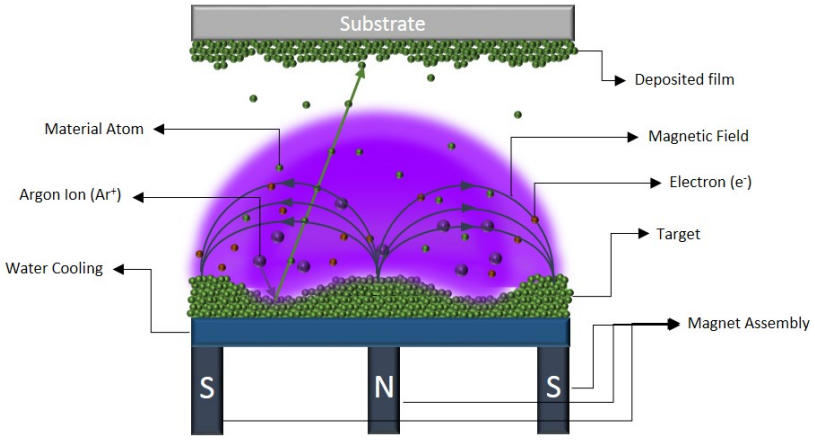

Figure 3.2: A typical magnetron sputtering system.

3.2.2 X-Ray Diffraction (XRD)

When a monochromatic X-ray strikes a sample surface, scattered beams from parallel lattice planes will undergo constructive and destructive interference. The constructive diffraction can be described by Bragg's Law

$$n\lambda = 2d\sin\theta, \tag{3.1}$$

where λ is the X-ray wavelength, θ the incidence angle, d the distance between parallel planes (Figure 3.3) and n is the order of reflection.

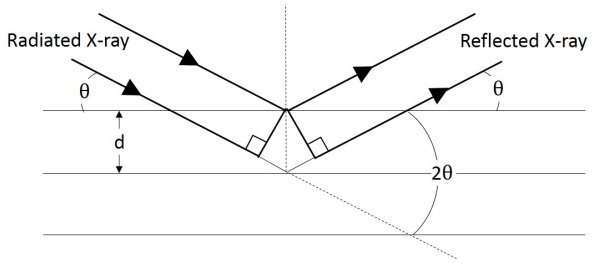

Figure 3.3: Bragg-Brentano (specular) diffraction geometry

In high angle XRD measurements (usually θ=15-90°) the possible direction of the diffraction depends on the symmetry of material's unit cell and its intensity varies with the number of irradiated planes that are perpendicular to the incidence beam and number of atoms in that plane. Also sample flatness, roughness, strain and stress can affect the intensity, shape and position of the reflected peak.

In the present project, crystal structure of films was characterized using a Cu-K_α beam. The Bragg-Brentano patterns were acquired in 20-80° range with a step size of 0.02° and dwelling time of 5 seconds.

3.2.3 X-Ray Reflectivity (XRR)

X-ray reflectivity was first used to characterize a copper coated glass by Prof. Lyman G. Parratt [119]. It can be used to derive film thickness, material density, interface roughness/inter-diffusion, and superlattice period (Figure 3.4).

As the refractive index of X-rays is less than one, there would be 100% reflection for incidence angles less than the critical angle, θ_c. Moreover, the penetration length of X-rays is proportional to $\sin(\theta/\mu)$ where μ is the material permeability. So for

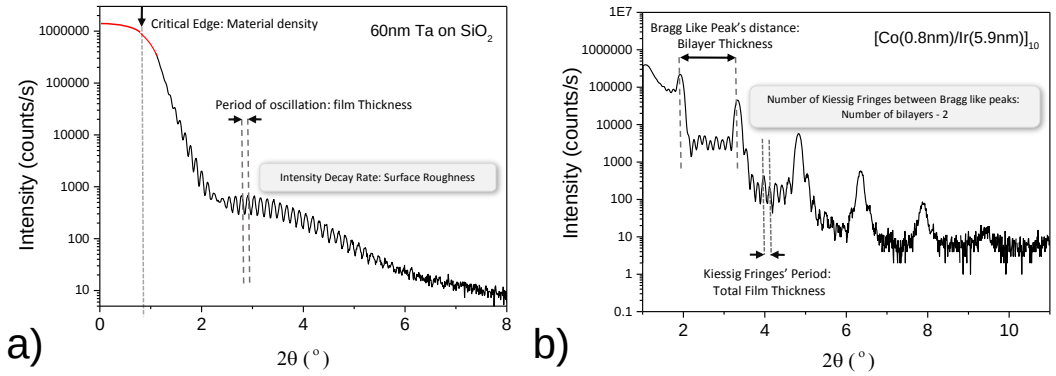

Figure 3.4: Specular XRR pattern from two sputtered samples. Parameters that can be estimated from the data are mentioned in the graph. a) Pattern for a monolayer of Ta deposited on SiO_2 (Red part of the graph is not from experimental data but added manualy to show probable critical edge), b) XRR for a superlatice film of $SiO_2\backslash[Co\backslash Ir]_{10}$.

grazing incidence on a perfect sample, the X-ray beam can reach substrate surface (for thicknesses less than 1 μm) and produce low frequency fringes called Kiessig fringes. The seperation between Kiessig fringes can give us an estimation of film thickness, so that smaller spacing means a thicker film. Also if the sample is a set of repeated bilayers (so called superlattice), Bragg-like peaks would appear in the pattern as a result of constructive interference from bilayer interfaces. Hence, the same way as for Kiessig fringes from a single film, the position and separation of peaks can be used to calculate bilayer thickness, as follows:

$$\theta_m^2 = \langle\theta_c\rangle^2 + m^2\left(\frac{\lambda}{2t_{bi}}\right), \tag{3.2}$$

where θ_m is position of the m^{th} bilayer peak, θ_c is the average critical angle of the total superlattice, λ is the wavelength of the X-ray, and t_{bi} is the bilayer thickness [120].

In this work, to achieve the most accurate deposition rate measurement for very thin films (thickness of some Angstroms) two bilayer superlattices of $[FM\backslash HM]_{10}$ are deposited (with normally the same deposition conditions for the final stacks). Then, using the low angle X-ray reflectivity patterns one can estimate the thickness of bilayer in the superlattice. Varying thickness of one of the materials in two deposited stacks can give us the deposition rate of each material.

3.2.4 Cross-Sectional High Resolution Scanning Transmission Electron Microscopy (HR-STEM)

The texture of supposedly epitaxial samples of Pt\Co\Pt_xAu_{1-x} and some of polycrystaline Pt\Co\Ir\Ta samples were investigated by cross sectional imaging using HR-STEM. This microscopy method provides atomic resolution imaging of the thin film and can be used to investigate thickness and structure of the different layers. Furthermore, *in situ* energy dispersive X-ray spectroscopy (EDX) can be exploited to get elemental analysis.

To be able to image with this technique, the sample should be transparent to electrons, meaning a very thin slice (<50 nm) of the stack should be prepared. Here, focused ion-beam (FIB) lift-out was used to prepare suitable slices. FIB is a system very much like SEM that uses Ga^+ beams for direct write lithography. FIB systems are usually equiped with an electron beam to be able to image the sample in real time.

Firstly, a rather thick layer (> 30-40 nm) of Pt is sputtered on top of the sample for protection against later radiated Ga^+ rays. Using ion beam deposition, the targeted area for further deposition/radiation can be limited to the desired dimensions (here roughly a rectangle of 15 μm (X) × 1.5 μm (Y) × 1.5 μm (Z)). Then, another high rate deposition of thick Pt will be used (∼300 nm in thickness). Afterwards, using a large Ga^+ beam current, two sides of the Pt rectangle will be milled down, leave a slice of material in the middle (the so-called bulking-out procedure). The central membrane then will get thinned (down to 1 micron) using further ion-beam milling with a smaller current. Tilting the sample, a frame around the membrane can be selected to be cut out (U-cut) and leaving a dangling slice just attached to the bulk on top corners. A needle will be attached to top of the membrane by Pt deposition and connections will be polished out (lift-out). The membrane will get attached to a copper mesh, again by Pt deposition and the needle will be set free (mounting). Then, the membrane will be milled to get a thickness of 60 nm. Finally, using ion milling on both sides of the membrane a polished slide with thickness of less than 50nms is in hand which is transparent to electron beams (Thinning and polishing). Different FIB proccessing steps are pictured in figure 3.5.

Note that here, on the samples which were finished in Pt or Au, instead of the first sputtered protective Pt layer a thin layer of sputtered carbon was used for protection and to enhance atomic contrast, which in turn helps with distinguishing the top layer

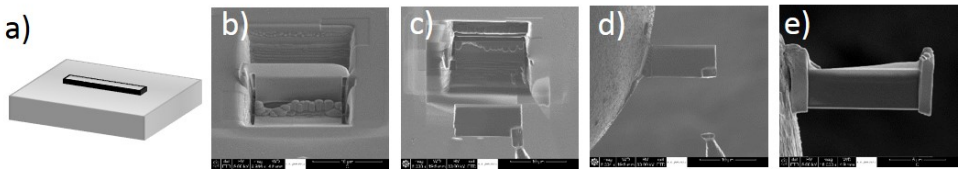

Figure 3.5: Sequence of TEM sample cross section preparation using FIB: a) Pt deposition, b) bulk out and U-cut, c) lift-out, d) mounting and e) thinning and polishing.

of the sample with later FIB deposited Pt.

The prepared membranes are then transmitted into the microscope. To get a beam of electrons, an extreme field emission gun (X-FEG) Shottkey emitter is used, and then beam goes through a monochromator to narrow the energy spread of electron source down to 100 meV. Subsequently, the electron beam gets focused by three sets of magnetic lenses down to the sample. Passing through the sample membrane, the transmitted electrons (and/or diffracted X-rays) can be detected to make a bright field image of atomic structure.

The microscope used was a FEI Titan3 Themis 300 operated by Michael Ward in University of Leeds (in case of epitaxial samples) and Marta D. Rossell in IBM Zürich (for polycrystalline specimens). Andreas Bischof has done the FIB process in IBM. The membranes were cut with a FIB FEI Helios 450S. Owing to several detectors that the system has, multiple measurements can be done at the same time. High angle annular dark field imaging (HAADF) was used here to get structural and topographical information by atomic resolution.

3.2.5 Energy-Dispersive X-ray Spectroscopy (EDX) Mapping

Energy-Dispersive X-ray analysis is an X-ray characterization technique which is usually used in SEM or TEM microscopes to identify elemental composition of the sample in question. If a radiated electron beam causes electrons from inner atomic shells of the sample to leave/excite, then higher state electrons will fill the vacancies and produce characteristic X-rays to the element.

An energy-dispersive spectrometer then can be used to detect emitted X-rays by the specimen, which converts X-ray energy into voltage pulses. This, in turn, will get sorted by voltage (*i.e.* X-ray energy) using a multichannel analyser.

In the present work, EDX was used for elemental mapping. In this technique, as the

electron beam scans the sample, characteristic X-rays will be detected and projected into an image specific to one element. The resolution is determined by the beam size and contrast is dependent on the dwell time at each point.

3.3 Magnetometry

The desired magnetic system in this study were thin films with perpendicular magnetic anisotropy. To examine their preferred anisotropy, a magneto-optical Kerr effect system was used to check in-plane and out-of-plane hysteresis loops of the sample. For more quantitative measurements such as evaluation of the saturation magnetization, anisotropy field and exchange stiffness we moved to SQUID-VSM. In the following, a brief explanation of these instruments and measurement procedure will be explained.

3.3.1 Laser-MOKE

Principally, when a polarized (laser) light reflects from a magnetic film, the polarization would change to elliptic, and the principal axis rotates (the so-called Kerr ellipticity and Kerr rotation, respectively). The amount of rotation is proportional to the value of magnetization.

There are basically three Kerr effects which are classified with respect to the magneto-optical geometry of the system: longitudinal, transverse, and polar configurations. Two of these are used in our MOKE system in University of Leeds (Figure 3.6) [121]:

1. Longitudinal Kerr effect: in which the field vector (of magnetic poles) is in the sample plane and parallel to the incident plane (plane containing normal line to the sample plane, incidence and reflected beam) for evaluating the in-plane component of magnetization.

2. Polar Kerr effect: in which the applied field is again parallel to the incident plane but perpendicular to the sample plane. In this configuration only out-of-plane component of magnetization is measured.

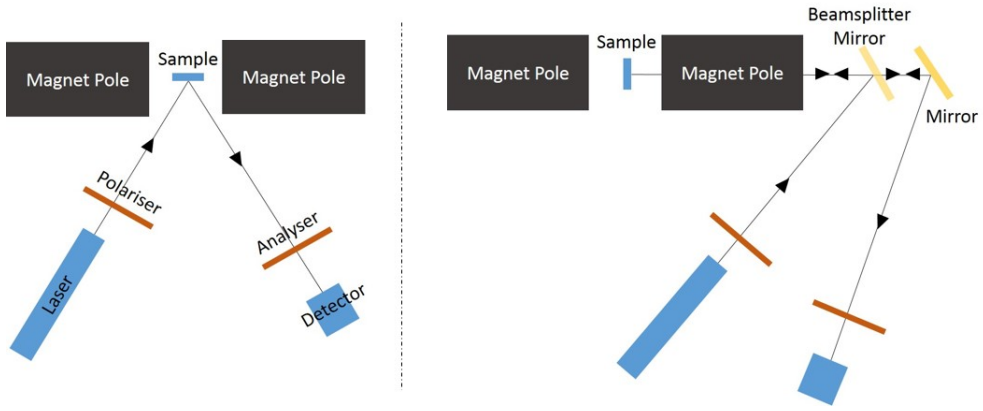

Figure 3.6: (left) Longitudinal and (right) polar MOKE configurations in Leeds. One can switch between them by moving optical rails that laser and detector are positioned on.

3.3.2 SQUID-VSM

SQUID-VSM is a very sensitive instrument to measure magnetic moments as small as 10^{-8} emu (10^{-11} Am^2). Its operation is based on the Faraday's law which is also used in standard VSM. A magnetic sample is connected to the end of a sample rod, and oscillates at a known frequency inside pick-up coils. The moving magnetic moment will induce an alternating current (AC) signal into the coils which are inductively coupled to a superconducting quantum interference device (SQUID), so that very weak signals would be converted to measurable voltage (Figure 3.7). In fact, SQUID works as a very sensitive and efficient current-to-voltage amplifier. The MPMS Quantum Design SQUID-VSM in Leeds can be used to measure samples in the range of 1.8-400 K (300-1000 K using an optional oven module) and in magnetic fields up to 7 T.

As the hard-axis of samples lies in the plane of the films, the magnetization and anisotropy fields of the different stacks were measured using in-plane magnetic loops by a SQUID-VSM device. As figure 3.7 shows, saturation magnetization, M_S, will be the average of saturated moments at high enough positive and negative applied fields devided by volume of the magnetic layer. As the investigated samples in this work all have out-of-plane anisotropy, the in-plane loops would not show any hysteresis, so the middle part of the graph as shown in figure 3.7 can be fitted with a line. The field on this line that has the saturation moment will be the anisotropy field, H_K , of the sample in hand.

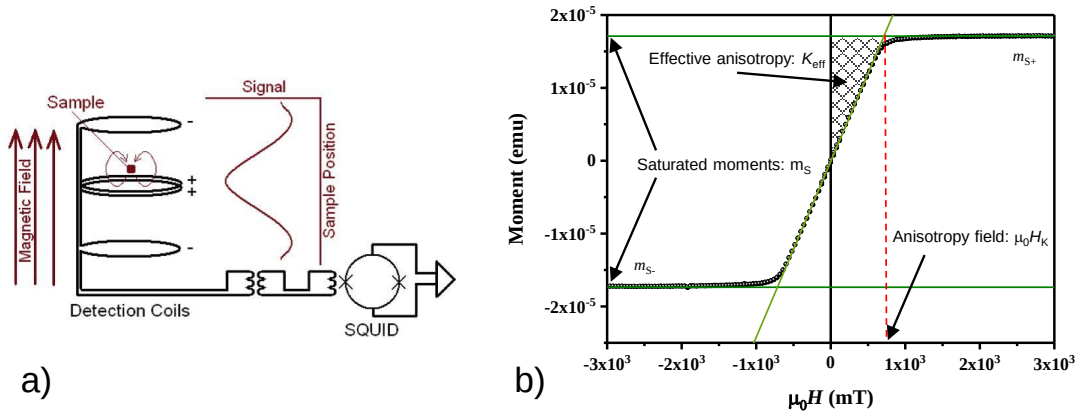

Figure 3.7: a) Schematic of detection system in Quantum Design MPMS SQUID-VSM [124], b) In-plane hysteresis loop of a Ta\Pt\Co\Ir\Ta stack with out-of-plane anisotropy deposited on SiO_2. Parameters that can be derived from experimental data are shown. The green lines are linear fits to data.

Also change of saturation magnetization, M_S, with temperature was measured for some samples in the range of 10-300 K. Recording M_S vs. T for two different in-plane applied fields (high enough to make sure sample is saturated at all times, here 2.8 T and 2 T) and taking the difference, one can remove the effect of temperature dependent diamagnetism coming from the substrate. Note that temperature dependence of magnetization far from Curie temperature can be described by Bloch law:

$$\frac{M(T)}{M(0)} = 1 - C\left(\frac{k_B T}{J}\right)^{\frac{3}{2}}, \tag{3.3}$$

where C=0.0294 for an FCC lattice, k_B is the Boltzman constant and J is the exchange integral [122]. One can fit the resulting curve with equation 3.3 and evaluate J as the fitting parameter. Then, the exchange stiffness, A, for an FCC material is [123]:

$$A = \frac{4JS^2}{a}, \tag{3.4}$$

where a is the lattice constant ($a = 3.55$ Å for cobalt) and $S = 1$.

3.4 Interfacial Magnetic Properties

As mentioned in the previous chapter, importance of material systems in hand is potential use of domain walls as an information carrier in storage media or processing

devices. To be able to optimize the properties of a domain wall, a deep study of its dynamics and underlying interfacial properties such as Dzyaloshinskii-Moriya interaction is needed. In this section, the processes used to investigate these properties will be explained.

3.4.1 Domain Wall Dynamics

To investigate domain wall dynamics, polar magneto-optical Kerr effect Microscopy (polar MOKE microscopy) was used. In this way, the images of domain walls before and after applying pulsed field/current were taken and velocity of motion of the domain walls could be calculated knowing the DW displacement during the pulse and the pulse time. The normal sequence of measurement is as follows:

1. Sample is placed under obective lens of the microscope.
2. Sample is saturated (up or down magnetized).
3. A small bubble domain/domain wall is nucleated (opposite magnetization)
4. If needed, a constant in-plane field is applied.
5. A background image is taken, then subtracted.
6. A pulse generator is used to apply a pulsed magnetic field/current.
7. Final image is saved.

Special care should be taken to find a good nucleation point where a consistent domain can be nucleated and destroyed several times. Also the InP magnetic field should be aligned with the sample so that it has no out-of-plane contribution to the driving field. Then, having the pulse time and displacement, velocity of DWs can be measured. In case of asymmetrical bubble expansion measurements, two right and left domain walls which are perpendicular to the direction of in-plane field can be measured. For every combination of driving forces and fields 3 to 5 images were taken using a different timing and the reported velocity is an average of all values.

Study of different dynamic regimes of a domain wall using bubble expansion has been done in Laboratorie de Physique des Solides(LPS), Universites Paris-Sud et Paris-Saclay, by the author. To be able to apply magnetic pulses as short as 1 μs a small coil (100 turns) with a rise-time of 250 ns was placed on top of the sample. The perpendicularly applied magnetic field was adjustable in amplitude (0 - 160 mT) and duration (1 μs - several seconds). In order to apply a field for longer than 60 μs

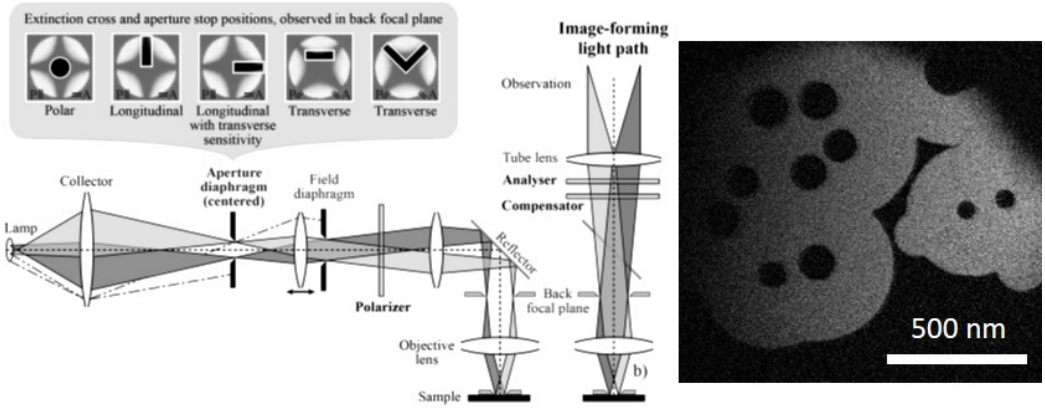

Figure 3.8: (left) The illumination loght path for perpendicular incidence in Kerr microscope in use at the university of Leeds [125]. (right) Bubble domains created with small coil in LPS.

multiple pulses were needed. The observation of flow regim was limited by mutiple domains growing into each other and destroying the domain wall.

To measure DMI by asymmetrical bubble expansion a Evico made wide-field Kerr microscope, which is supplied with an in-plane magnet, is used (Figure 3.8). The InP magnet can reaches fields up to 250 mT. Also, a home-made OoP coil is used to apply out-of-plane magnetic fields which can produce pulses as short as 3 ms and as large as 40 mT.

For current-induced measurements, the same Zeiss instrument with in-plane and out-of plane magnets was exploited to apply needed magnetic fields and to picture current induced domain wall motion. Samples were patterned into wires of 2.5×20 μm^2 and Cr\Au contacts were deposited on top. Then they were glued down by silver-paint and wire-bonded to the holder. An Agilent HP8114A pulse generator was used to apply nanosecond long current pulses. Firstly, the wires are saturated in one direction. Then, a DW is nucleated applying a short high voltage/current pulse when a very small OoP field (a few milli-Teslas) in the opposite direction is present. Afterwards, DW displacement can be measured by applying pulsed current. This measurement can be done in the absence and presence of a constant InP field.

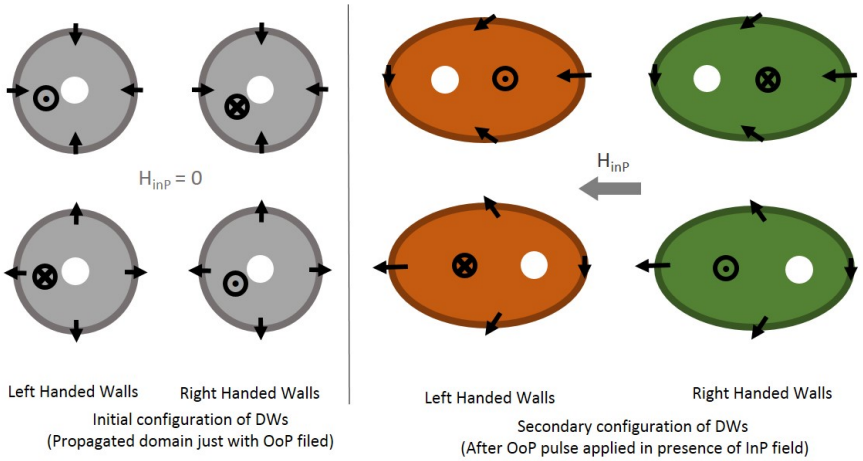

Figure 3.9: Revealing the chirality of the domain walls in the sample knowing direction of the bubble domain magnetization and in-plane field using Kerr images. The white spot in the middle is the initial nucleated domain which is subtracted from the final image. The same rules applies if the in-plane field is in the opposite direction.

3.4.2 Chirality of Domain Walls

Investigating bubble expansion, it is possible to know the chirality of domain walls with just one image. Assuming the bubble domain has chiral Néel wall, magnetization of the wall point to either the outside of the bubble or the inside, depending on the sign of DMI (Figure 3.9). When an in-plane field is applied, the direction of the DW magnetization will be implied by sum of H_{DMI} and H_{InP}. The part of the DW in which the initial magnetization is aligned with the applied in-plane field, has lower energy density, hence moves faster and further than other regions of the bubble. Then, knowing the magnetization direction of bubble itself (up or down) chirality of the walls would be known as explained in figure 3.9. Exploiting the same argument reveals that domain walls in all samples in this report are left-handed (LH).

3.4.3 Brillouin Light Scattering (BLS) Spectroscopy

Here, the Damon-Eshbach geometry BLS was used, in which the film is in-plane magnetized so that the magnetization is perpendicular to the scattering plane (Figure 2.8). As the backscattered light is detected, momentum conservation decides that SWs which are propagated in the scattering plane are being measured (Figure 3.10). The incident

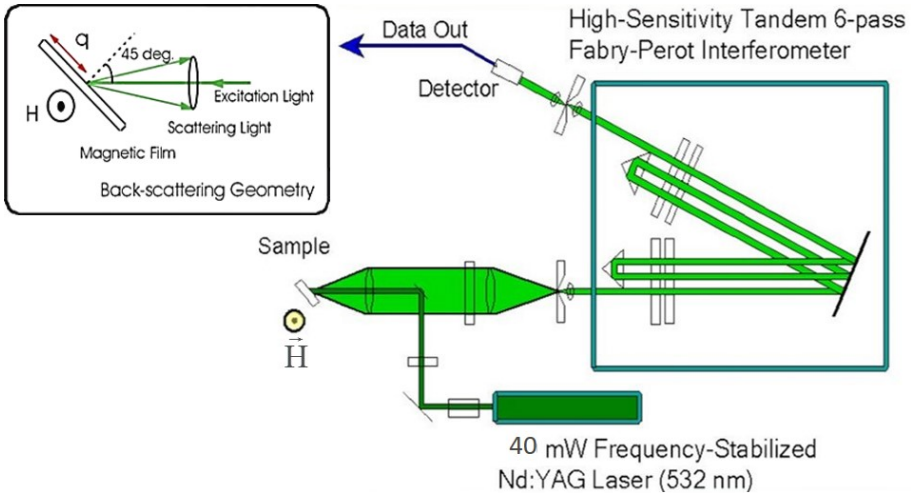

Figure 3.10: A schematic of the BLS instrument and the six-pass Fabry-Pérot interferometer. The inset depicts the backscattering setting in use (Schematic is courtesy of Justin M. Shaw).

laser power of the used instrument was 40 mW, which has a wavelength of $\lambda = 532$nm. As figure 3.10 shows, the sample is placed at the fixed angle of $\theta = 45^\circ$ on which the beam is focused using a $f/1.2$ lens. Hence, the measured SWs would have a wavenumber of $16.7\mu\text{m}^{-1}$. The backscattered beam is detected after going through a six-pass Fabry-Pérot interferometer. It should be noted that all BLS data are taken in National Institute of Standards and Technology (NIST) by Justin M. Shaw and Hans Nembach.

Chapter 4

Epitaxial Trilayers of Pt\Co\Au_xPt_{1-x}

4.1 Introduction

Investigating the Dzyaloshinskii-Moriya interaction in multilayers with broken inversion symmetry is a matter of enormous interest since it is the DMI that stabilises Néel DWs, skyrmions and other chiral structures in such systems. Many different structures have been studied to achieve higher DMI. However, DMI is very sensitive to interface quality. The effect of two different interfaces on each side of a ferromagnet is not solely dependent to the material which is used [41]; it also depends on growth conditions [41], FM and HM layer thickness [30, 126, 127], interface roughness and inter-diffusion [40, 128], crystallinity, oxidation [129, 130], *etc.* Every one of these can break the inversion symmetry in practice, due to differing interface quality.

On the other hand, nearly all studied thin films are deposited by sputtering at ambient temperature, thus polycrystalline or amorphous. This makes it difficult to compare or reproduce results, or learn about fundamental physics behind DMI. To avoid the often-reported ambiguities arising from the variable quality of sputtered polycrystalline or amorphous layers and unknown contributions to DMI from uncontrolled interfaces, here we investigated fully epitaxial layers of Pt\Co\Au_xPt_{1-x}. Changing the top layer systematically, we could change and control the broken inversion symmetry by adding gold to the top layer by co-sputtering. This would break the centro-symmetry of Pt\Co\Pt without contributing to the total DMI of the system [29, 34, 42].

4.2 Growth and Structural Analysis

We started off with the symmetrical case of Pt(3)\Co(0.6)\Pt(3) (numbers in pareantheses are nominal thicknesses in nanometer throughout the thesis, unless stated otherwise), which is expected to have zero or negligible DMI. Then, for the next trilayer, gold is added to the top layer by co-sputtering to break the inversion symmetry. The final structure is Pt(3)\Co(0.6)\Au(3) which has the highest broken inversion symmetry between the three, so expected to have the strongest DMI. Schematics of structures are displayed in figure 4.1.a.

The first platinum layer is grown at 550℃ on C-plane sapphire substrate, and the top Co\Au_xPt_{1-x} bilayer is deposited at 100℃. Then, the system is cooled down to less than 40℃ and a $\sim$ 2.5 nm capping Ta layer is sputtered afterwards to keep the main trilayer from oxidation. To get a 50-50 alloy of Au and Pt, the deposition powers

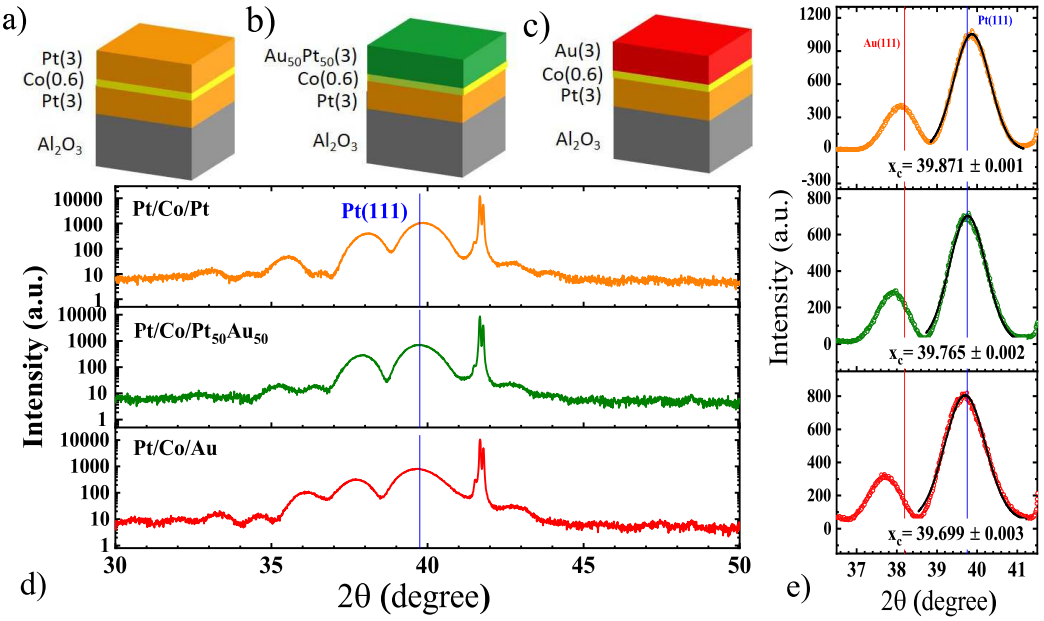

Figure 4.1: a-c) Structure of the Pt\Co\$Au_xPt_{1-x}$ samples deposited on C-plane (0001) sapphire substrate. d) XRD patterns of stacks of Pt\Co\$Au_xPt_{1-x}$ with different gold contributions to the top layer. Clear (111) texture of all three cases can be seen in patterns. e) The main XRD peak of the multilayers along with its Voigt fit. The center of the peak as found out by the fit is mentioned for each sample. The blue and red vertical line is showing expected (111) diffraction peak of bulk-Pt and bulk-Au respectively.

for Au and Pt were calibrated carefully to keep the growth rate stable at ~ 1 Å/s for both elements. The deposition and nanofabrication of the films in this chapter were done by Aleš Hrabec (ETH Zürich, formerly at the University of Leeds).

To examine the epitaxial structure, X-ray diffraction measurements have been done by our colleagues in Leeds electron microscopy and spectroscopy centre. Figure 4.1.d shows clear FCC(111) texture for the different samples, where the main peak sits at $\theta \backsimeq 40°$. This main peak is very close to the Pt (111) Bragg peak with $\theta_{\mathrm{Pt}} = 39.74°$. As figure 4.1.e shows, this main peak is slowly moving towards Au(111) at $\theta_{\mathrm{Au}} = 38.19°$ as the concentration of gold in the top layer is increasing. The appearance of Pendellösung fringes around the main peak is attributed to uniform strain in the multilayer and the good quality of the interfaces [131, 132]. Cross sectional STEM images (Figure 4.2.a-c)

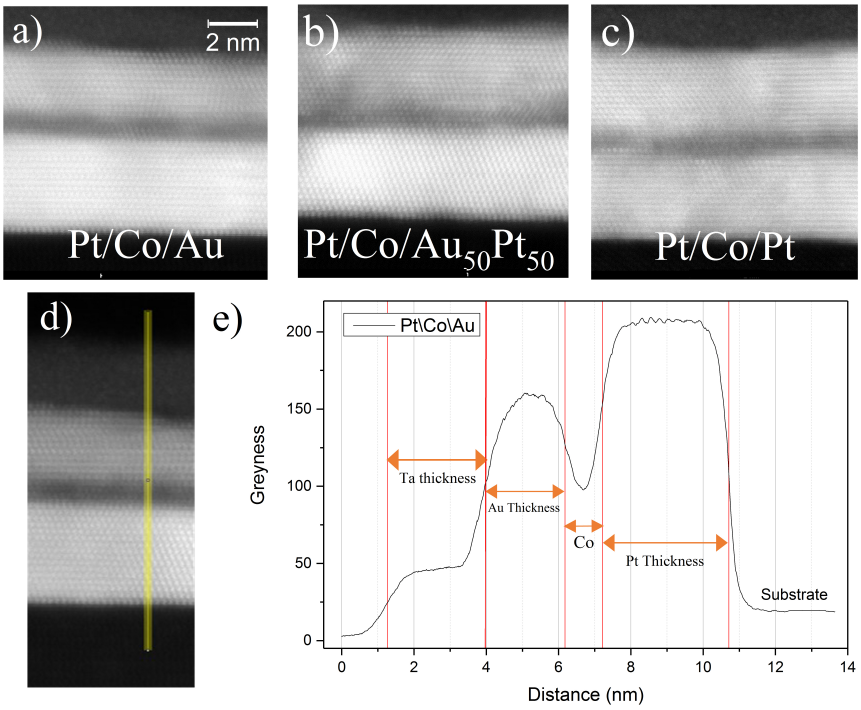

Figure 4.2: a-c) Cross sections of multilayers imaged by HR-STEM in Leeds (by Michael Ward), confirming the crystalline quality of the thin films. d-e) A sample of greyness change from the 0.4 nm stripe (in yellow) on the image. Width of the peaks were used to estimate thickness of different layers.

also show clear uniform crystallinity of the three multilayers, even in the thin cobalt layer. The fact that image brightness is related to the atomic number of the elements enables us to study the images in more detail. Vertical stripes of 0.3-0.4 nm width were selected (Figure 4.2.d), and the change of greyness was used to determine the thickness of the layers for each stripe (Figure 4.2.e). The STEM image scale was also calibrated using the in-plane atomic distance of the sapphire substrate. Averages of values were taken as the final thickness of the layers. Consequently, the measured thicknesses of table 4.1 was deduced. The resulted Co thickness is much higher than nominal thickness of 0.6 nm. This is as a result of additive effect of all atomic layers throughout the thickness of TEM slab (usually ~ 50 nm). Hence the thickness fluctuations of the thin Co layer is added to the actual thickness of the layer. It was also previously stated in literature than thickness evaluation from STEM cross section is not always resulting to a

Table 4.1: Thickness of different layers of thin films of Pt\Co\X\Ta (X is Au, $Au_{50}Pt_{50}$ or Pt), deduced from STEM cross section images. The mentioned errors are standard deviation from thickness profiles of the thin stripes.

Structure	Pt	Co	X	Capping Ta
	nm	nm	nm	nm
Pt\Co\Au	3.39 ± 0.01	1.03 ± 0.01	2.18 ± 0.01	2.55 ± 0.01
Pt\Co\$Au_{50}Pt_{50}$	3.21 ± 0.02	1.26 ± 0.03	2.70 ± 0.02	2.45 ± 0.01
Pt\Co\Pt	3.17 ± 0.04	1.17 ± 0.03	2.97 ± 0.02	2.17 ± 0.01

realistic value and depending on the interface interdiffusion it might lead to estimations twice as much [133]. As a result, we decided to use nominal thickness for Co to calculate different physical parameters (The error on nominal thickness calculation was assumed to be 10% for all values throughout the thesis). Images also show that Au layer has more fluctuation of thickness (*i.e.* roughness), as is normally expected for Au sputtered films.

4.3 Magnetic Characterization

All the samples show a square polar hysteresis loop confirming the out-of-plane character of Co. The square loops taken by MOKE are presented in figure 4.3.a along with the normalised hard-axis (in-plane) SQUID-VSM data (figure 4.3.b). The latter was used to measure saturation magnetization, M_S, and anisotropy field, H_K of the thin films as it was explained in detail in section 3.3.2.

To calculate M_S, it was assumed that all the measured moment is confined in the Co layer of thickness t_{Co}, and thickness of proximity magnetized material was neglected.

Changing Au's concentration systematically from 0% to 100%, and knowing that proximity magnetism in Au is negligible [34, 134], unlike Pt, one can assume that the amount of material with proximity induced anisotropy is twice as much in Pt\Co\Pt compared to Pt\Co\Au. Then subtracting Pt induced magnetization contribution from the total amount, the magnetization of cobalt, $M_{S,Co}$ can be deduced. The results are presented in figure 4.3.d showing total magnetization, plus Co and Pt contributions. The results show that induced magnetization of Pt is $\sim 20\%$ of the total magnetization

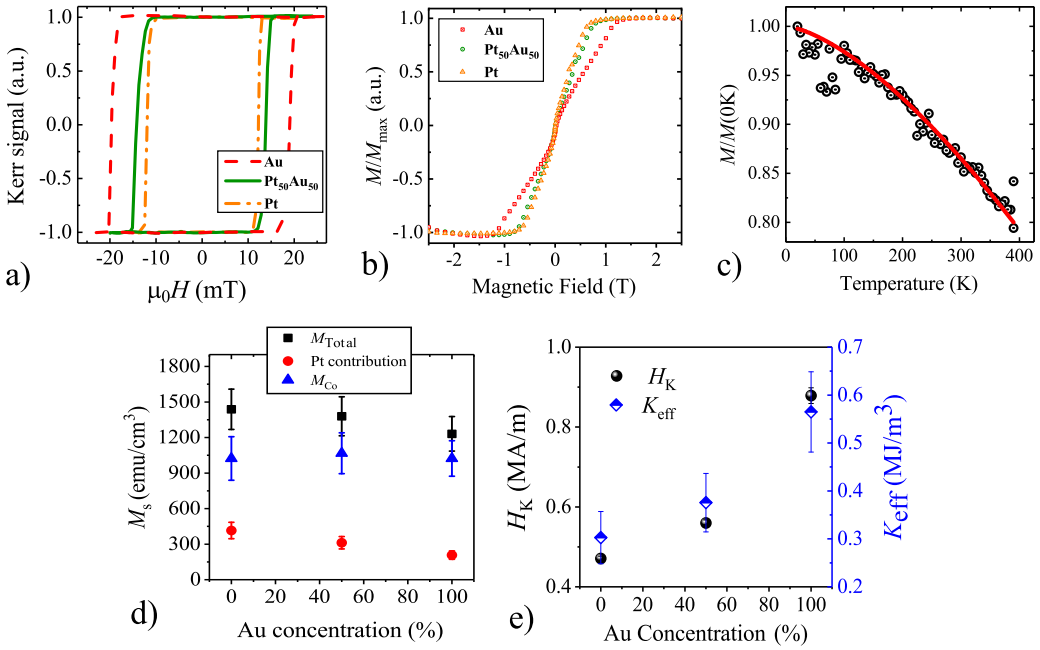

Figure 4.3: a) Polar MOKE patterns resembling perpendicular magnetic anisotropy of the deposited multilayers. b) SQUID-VSM measurements in in-plane (hard-axis) configuration. c) Change of normalized saturation magnetization with temperature for Pt\Co\Pt multilayer, fitted with the Bloch law. d) Total saturation magnetization, M_S, of Pt\Co\Au$_x$Pt$_{1-x}$. Knowing the gold percentage in the top layer we could derive magnetization of cobalt and platinum layers. e) Rising trend of H_K and K_{eff} with Au concentration.

of sample. Interestingly -but trivial at the same time- cobalt magnetization in all samples is the same and about 1000 emu/cm^3. Value of $M_{S,Co}$ (hereafter just mentioned as M_S) is comparable with previously published saturation magnetization for Co/Pt multilayers with the same nominal thickness [12, 41, 88, 135–137]. On the other hand, if thicknesses derived from brightness profiles of STEM images are used, the resulted saturation magnetization for Co will be $\sim 600 - 700$ emu/cm^3 which is unusually low for supposedly ~ 1 nm of Co [38, 135]. Consequently, the nominal thickness of cobalt will be used for calculation of other related parameters throughout the chapter.

Also, having the temperature dependence of magnetization, we can fit its curve with the Bloch law. The Bloch law indicates the relation of saturation magnetization

with temperature if it is far from Curie temperature:

$$\frac{M_S(T)}{M_0} = 1 - C\left(\frac{k_B T}{J}\right)^{3/2} \tag{4.1}$$

where M_0 is saturation magnetization at 0 K, C=0.0294 in case of an FCC lattice, k_B is the Boltzmann constant and J is the exchange integral [122]. For an FCC film exchange integral is related to the exchange stiffness as follows [123]:

$$A = \frac{4JS^2}{a} \tag{4.2}$$

in which a is the lattice constant and $S = 1$. So, temperature dependence of saturation magnetization has been measured and used to get the exchange stiffness in Pt\Co\Pt (figure 4.3.c). First the magnetization turned to in-plane direction applying high in-plane field, then change of saturation magnetization, M_S, with temperature (5 K to 300 K) was measured with two different in-plane field applied (2 T and 3 T here). Subtracting these two sets of data from each other, we can eliminate the contribution of temperature dependent diamagnetic signal. Following the mentioned procedure, the exchange stiffness parameter was evaluated as $A = 17 \pm 1$ pJ/m. Although this value is much lower than the exchange stiffness for bulk cobalt, 30 pJ/m [138], it is compatible with other A estimations for the same Co thicknesses [139].

Figure 4.3.e shows that the anisotropy field, H_K, of the multilayers is increasing with Au concentration of the top layer. The increasing of coercive field with x is also clear in figure 4.3.a. The anisotropy field and saturation magnetization were used to calculate effective anisotropy, $K_{eff} = \mu_0 H_K M_S/2$, demagnetizing energy, $K_D = \mu_0 M_S^2/2$, and uniaxial anisotropy $K_U = K_{eff} + K_D$ for future parameter calculations such as domain wall width and domain wall energy density. The effective anisotropy is also rising with percentage of gold in the top layer.

4.4 Field-Induced DW Motion (FIDWM)

Field-induced (current-free) domain wall motion is very useful in studying the dynamics of the system as it helps to rule out all current induced effects which usually bring up complications, such as SHE and Rashba effect. FIDWM can be used to measure different material dependent parameters, especially in systems with broken inversion symmetry when the effects are dominated by DMI and influencing DW structure. In

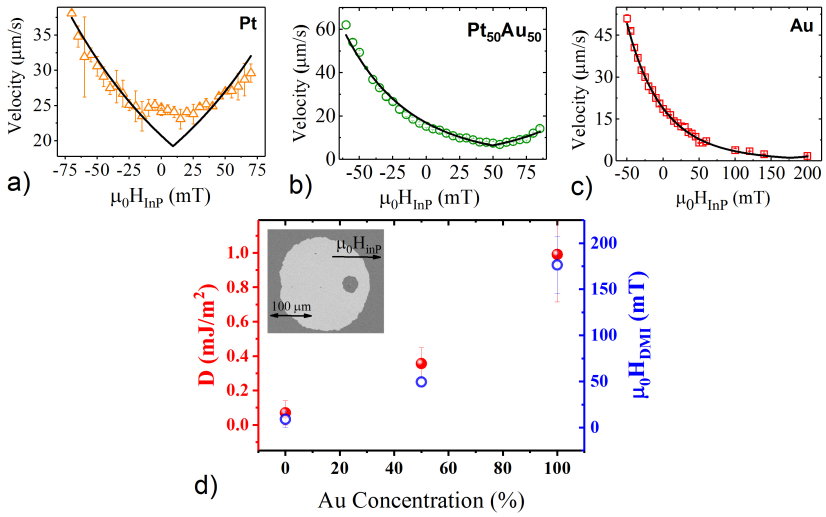

Figure 4.4: Asymmetric bubble expansion of Pt\Co\X: a-c) Changes of velocity for the DW normal to the InP field for different cobalt covering layers. Data are fitted with simple model of creep regime theory to get the DMI. d) Evaluated DMI field using asymmetric bubble expansion method (blue open circles) and DMI constant (red dots) as a function of Au concentration. The inset is a wide-field Kerr image of asymmetrical bubble expansion in presence of InP field.

this section we investigated bubble domain expansion as a function of both out-of-plane and in-plane field.

4.4.1 Asymmetrical Bubble Expansion

As mentioned in section 2.5.2, measuring DW velocity for different in-plane fields gives us an estimation of the DMI in the sample. Figure 4.4 represents DW velocity, v, measurements for Pt\Co\X where X is Pt, $Au_{50}Pt_{50}$ or Au. Experiment and fitting of this asymmetric bubble expansion was done by Aleš Hrabec in Leeds. Magnetic parameters mentioned in previous section was used and changes of velocity with InP field was fitted using equations 2.18, 2.19, and 2.20. It should be also noted that for the case of Au cap layer, the minimum of the velocity curve could not be seen reliably to the highest achievable in-plane field. So fitting the curve leads to a high uncertainty for D.

Going from Pt to Au, as the top layer of cobalt, it is clear that the inversion

symmetry of the structure increases, which is expected to lead to a rising DMI field, H_{DMI}, and constant, D. This can be proved with the shift of minima in velocity vs. H_{InP} graphs in figure 4.4. In this way, Pt\Co\Au shows the highest DMI ($D = 1.0 \pm 0.3$ mJ/m^2). Also, knowing that the magnetization of the bubble domain shown in the inset of figure 4.4 is pointing out of the sheet, and using the symmetries of field alignments one can easily deduce that DWs have left-handed chirality (*c.f.* section 3.4.2), which is again consistent with *ab initio* calculations and previous experimental studies on Pt\Co interfaces [12, 29, 31].

4.4.2 Symmetrical Bubble Expansion

One of the ways to get material properties in PMA multilayers is to study the propagation of DW when OoP field is applied on the film. This experiment can offer us information about samples pinning properties, Walker breakdown, and damping, considering minimal sample preparation it needs (you, basically, just need to clean the specimen). Knowing these will bring us a better understanding of domain wall motion, which in turn helps us in engineering of future devices. As a result, propagation of bubble domain with increasing out-of-plane field (no in-plane field present) was investigated for the multilayers. Experimental data were acquired by Aleš Hrabec in LSP, Paris-Sud University, analysis of the data and fitting is done by the author and they are all presented in figure 4.5. Increasing the broken inversion symmetry of the system, it can be seen that achievable DW velocity at a particular driving field is also increasing. Although, the creep motion was not measured for more than 20-30 mT field range, DW velocity, v, still changes by three orders of magnitude (figure 4.5.b). After that comes the inflection point of the curve and the start of depinning transition. Also, in all cases there seem to be some points with a linear variation of velocity at high fields belonging to the flow regime.

All the curves were fitted using the following procedure including only three structure-dependent fitting parameters (*c.f.* section 2.4.3):

1. Checking equations 2.9 and 2.13 one can confirm that the curvature of the creep and depinning regime are opposite in sign, so there is an inflection point which separates the two regimes. This point is assumed to be the higher limit of the creep regime, *i.e.* $(H_{\mathrm{d}}, v(H_{\mathrm{d}}))$ (stars in figure 4.5.a-b).
2. The low driving field interval of $0 < H < H_{\mathrm{d}}$ is then fitted by equations 2.9 and

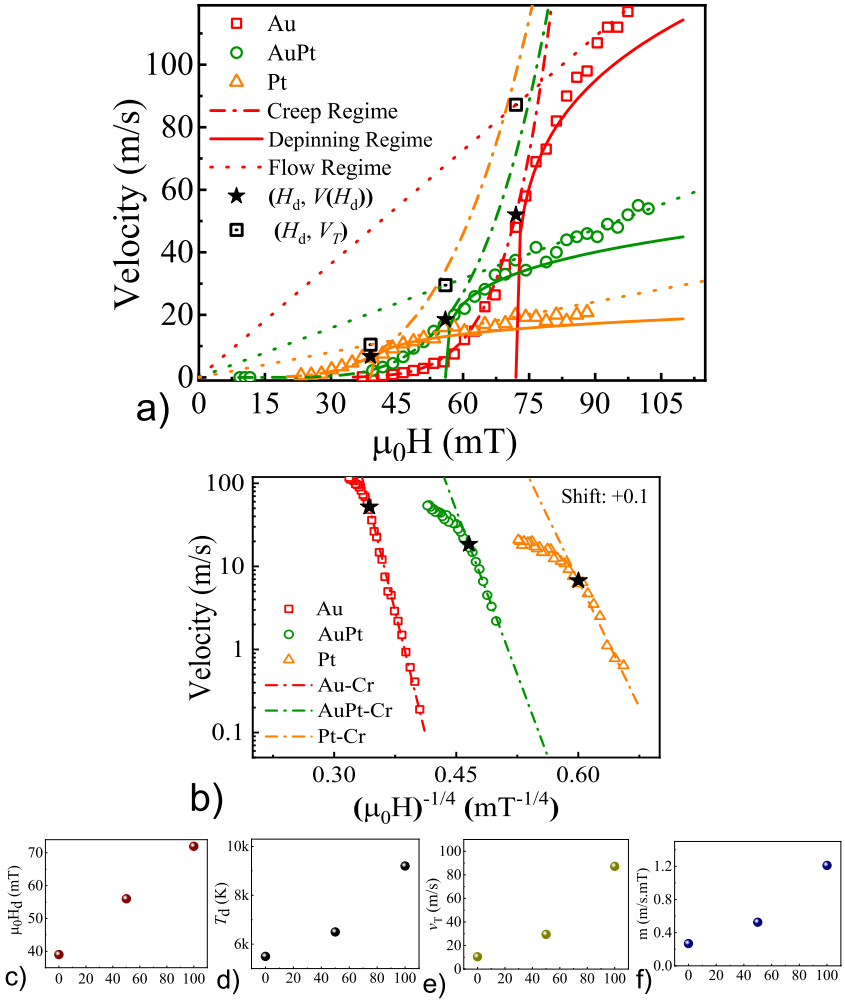

Figure 4.5: a) Symmetric field-induced domain wall motion (no in-plane field) for Pt\Co\Au$_x$Pt$_{1-x}$. The data are fitted with universal models for the creep (dashed-dotted curve) and depinning regimes (solid curve). The star shows the depinning velocity, v_T, from which the mobility of the flow regime and the resulting linear change of velocity is estimated, illustrated by the dotted lines. b) Same curves of part (a) in a semi-logarithmic scale plotted as a function of $(\mu_0 H)^{-1/4}$ to emphasise on the linear variation of creep velocity in this relation. Data are shifted to the right respectively for clarity of presentation. c-f) changes of depinning field, H_d, depinning temperature, T_d, depinning velocity, v_T, and mobility of DW, m, with respect to concentration of gold on the top layer, all showing an upward trend.

2.10 to get an estimation of the depinning temperature, T_d.

3. To increase the accuracy of the estimations, the second step is repeated for higher H_d until the fit diverges from the experimental curve. The final H_d value is considered as the upper limit of creep regime.
4. Finally, equation 2.13 with $\beta = 0.25$, $\psi = 0.15$, and $x_0 = 0.65$ [94, 140] is used to fit the universal depinning regime for $H \geqslant H_d \left[1 + \left(0.8 \times (T/T_d)^{\psi}\right)^{\frac{1}{\beta}}\right]$ (*cf.* section 2.4.3). Using this fit we could get a finer tune of H_d, $v(H_d)$ and T_d.

The fits can all be seen in figure 4.5 for various top layers. Estimating the three material dependent parameters from the simultaneous fits of the creep and depinning regimes, it is observed that all three of H_d, T_d (figure 4.5.a-b) and $v(H_d)$ have a rising trend with concentration of gold in the top layer, *i.e.* broken inversion symmetry (Figure 4.5.c, d, and e).

Assuming that v_T (*c.f.* equation 2.11) is the velocity that DW would have in absence of pinning, the mobility of the domain wall then will be $m = v_T/\mu_0 H_d$. Using this calculated mobility, we can draw a line with this slope going through origin which shows the linear change of velocity in the respective flow regime. Non-trivially, the line falls onto the very experimental data points at high fields, which were already suspected to be related to flow regime (within experimental fluctuation). This is interesting, as this DW mobility is calculated from fitting of creep and depinning functions which are entirely separate from where the flow regime can happen. In other words, there is a possibility to gain knowledge of flow related behaviour without reaching the attributed velocities.

Also, proportionality of domain wall mobility to the damping factor, α, can be used to know about the accessible flow regime as follows [88]

$$m = \frac{\gamma \Delta}{\alpha} \quad \text{Steady} \tag{4.3}$$

$$m = \frac{\gamma \Delta}{\alpha + \alpha^{-1}} \quad \text{Precessional} \tag{4.4}$$

where γ is the gyromagnetic ratio, Δ is domain wall width, $\Delta = \sqrt{A/K_{\text{eff}}}$, and α is the Gilbert damping factor. Following this process, the mobility of the domain walls leads to a precessional flow with $\alpha_{\text{exp}} = 0.9 \pm 0.1$ and 0.4 ± 0.1 for Pt\Co\Pt and Pt\Co\$Au_{50}Pt_{50}$, respectively, and a steady flow solution with $\alpha_{\text{exp}} = 0.2 \pm 0.1$ for Pt\Co\Au. So, using universal DWM functions, we confirmed the resulted damping factor is also increasing with Au proportion in the layer covering cobalt.

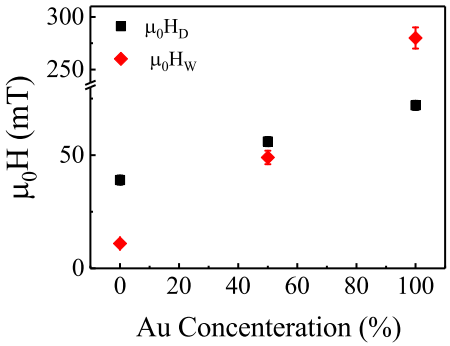

Figure 4.6: Comparison of Walker breakdown field, H_{W}, and depinning field, H_{d}, for different contributions of Au in the top layer.

As stated in section 2.4.3, the steady and flow regime are separated with Walker breakdown field, H_{W}. This field can be evaluated using [11]

$$H_{\mathrm{W}} = \alpha \sin \Phi_{\mathrm{W}} (H_{\mathrm{DMI}} - H_{\mathrm{demag}} \cos \Phi_{\mathrm{W}}), \tag{4.5}$$

where α is the Gilbert damping, H_{DMI} DMI field, H_{demag} the DW demagnetizing field, and $\cos \Phi_{\mathrm{W}} = ([H_{\mathrm{DMI}}/H_{\mathrm{demag}}] - \sqrt{[H_{\mathrm{DMI}}/H_{\mathrm{demag}}]^2 + 8})/4$. [11]. The Walker field is expected to increase with Gilbert damping and DMI in the sample. As it is clear in figure 4.6 H_{W} is significantly rising with increasing of gold contribution in the top layer (*i.e.* increasing of breaking inversion symmetry, hence DMI). Comparing these values with depinning field, H_{d}, self-consistency of the results are confirmed. As for both of the Pt and $Pt_{50}Au_{50}$ samples $H_{\mathrm{W}} < H_{\mathrm{d}}$ one can say that Walker field is hidden in the creep regime and only precessional flow is accessible. On the other hand, Au sample is a good example for the case that H_{W} is higher than H_{d}, thus both steady and precessional flow can be seen in such a system. Unfortunately, multiple nucleation and merging of the bubble domains at high applied fields for the investigated sample limited the measured velocities to steady flow values.

4.4.3 Micromagnetic Simulation

As a part of collaboration within the Marie Curie ITN-WALL network, micromagnetic simulation and 1D model calculations of FIDWM for present samples were studied by Simone Moretti (formerly at the University of Salamanca). MuMax 3.9.3 [141] was used to simulate a rectangular sample of $1024 \times 512 \times t$ nm^3 (t is the FM layer thickness)

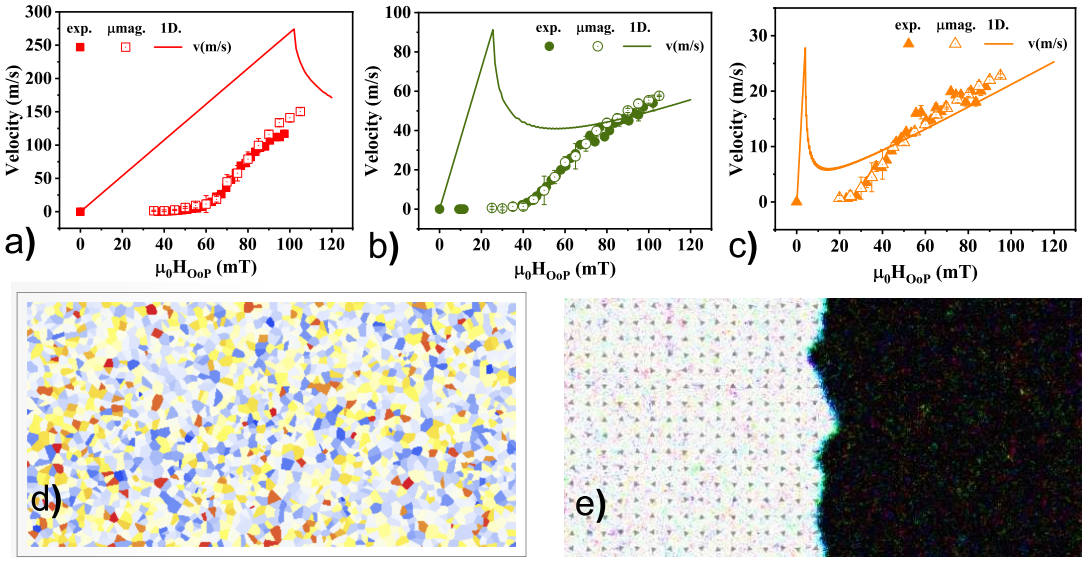

Figure 4.7: Field-induced DW motion in Pt\Co\X for capping layers of a) Au, b) AuPt, and c) Pt, along with the simulation from micromagnetic simulations and 1D model results. It is shown that 1D model cannot predict experimental FIDWM while the micromagnetic simulations can follow changes in velocity much more precisely. d) An example of grain pattern used for micromagnetic simulations. e) A snapshot of a DW in the system.

and periodic boundary conditions were applied along the y axis (along width of the rectangle). The sample was then discretized to $2 \times 2 \times t$ nm^3 cells. Disorder was set as the fluctuation of the Co layer's thickness distributed normally around the experimental value. In this way, the saturation magnetization, uniaxial anisotropy and DMI of each grain would also vary as follows:

$$t_{\mathrm{G}} = N(t_0, \delta t) \rightarrow \begin{cases} M_G = (M_{\mathrm{S}} t_{\mathrm{G}}/t_0) \\ K_G = (K_{\mathrm{S}} t_{\mathrm{G}}/t_0) \\ D_G = (D_{\mathrm{S}} t_{\mathrm{G}}/t_0) \end{cases} \tag{4.6}$$

where t_0 is the experimental value of FM layer thickness, δt is standard deviation of thickness spread and G stands for grain (Figure 4.7). It should be noted that the studied multilayers are epitaxial and does not have grain structure *per se*. Here fluctuations of the FM layer thickness was taken to define the *"grain"*.

Different thickness fluctuation, δt, and grain sizes were used, to be able to reproduce the experimental data. Finally, grain size of 15 nm and δt of 7%, 8.5% and 9% was used for Pt, AuPt and Au capped multilayers, respectively, and the resulted Gilbert damping, $\alpha_{\mu mag}$ was derived from simulations. The fitting results are demonstrated in figure 4.7. The agreement of micromagnetic simulation outputs with experimental data is very good, indeed. The solid lines in the figure are indicating the result of 1D model (where disorder is absent) calculated using $\alpha_{\mu mag}$. It is shown that 1D model cannot predict the behaviour of the domain wall dynamics, especially for Au and AuPt top layer. It could only roughly reproduce the high field region for Pt\Co\Pt when it was mentioned to coincide with the flow regime. This is expected, as the 1D model results are only for a sample without any disorder which almost never can be the case in real life.

4.5 Current-Induced DW Motion (CIDWM)

It was stated in previous chapters that DWs in PMA are important for applications in spintronic devices which are going to be operated using current. Hence, study of current-induced DW motion attracted a lot of experimental attention, recently. Here also, to study current-based DW dynamics, films were patterned into 2.5×20 μm^2 wires (by Aleš Hrabec). The samples in this section have the nominal Co thickness of 0.8 nm. Unfortunately, the magnetic characterization of these samples are not in hand, as they were patterned before doing such. Nevertheless, their current-induced DWM can be studied qualitatively.

4.5.1 Current Induced Switching

Possibility of current induced switching was investigated in patterned films. Firstly, the wires were uniformly magnetized by applying a perpendicular field. Then, an in-plane magnetic field of various magnitudes was applied in order to obtain an in-plane component of magnetization, which is sensitive to the spin-orbit torque. Magnetization reversal was seen in Pt\Co\Au and Pt\Co\$Pt_{50}Au_{50}$ using pulsed current with density of 2.2×10^{12} A/m^2 (Figure 4.8). The polarity of the current reversibly sets the resulting magnetization state which is in agreement with SOT-induced switching scenario. No magnetization switching was seen for Pt\Co\Pt as was expected: due to the completely

symmetrical case of this stack, torques coming from top and bottom layers cancel each other and there won't be any net spin-orbit torque applied on the magnetization of the ferromagnetic layer.

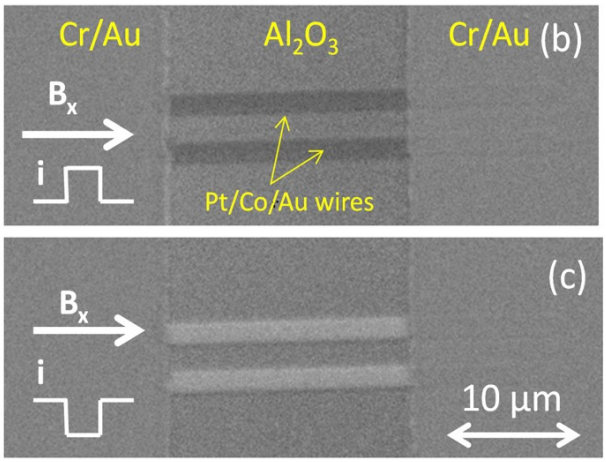

Figure 4.8: Subtracted Kerr image of Pt\Co\Au showing magnetization reversal. Direction of magnetization changes depending on the direction of applied current.

4.5.2 Evolution of DW Velocity with Current Density

In order to investigate the efficiency of Slonczewski-like torque, current induced movement of DWs in patterned nanowires was studied. After current induced switching process, it was noticed that there is always a DW trapped where Cr/Au contact finishes and the wire starts. It is expected that the current shunting to the contact pads at such point does not let the current to flow into the part of the nanowire that sits underneath the contact, so it remains unswitched. As a result there will be a DW at each edge of the wire. Then, applying only current to the wires, the DW starts moving into the field-of-view. Figure 4.9.a presents a typical DW motion in a sequence of 2.2×10^{12} A/m^2 current pulses separated by 60ns.

DW displacement was measured using pulses of increasing current density. For each measurement several pulses of 20 ns was used which were separated by 200 ms. Velocity was calculated by dividing the displacement by the total pulse time. Velocity at each current density is an average of five individual measurements. To minimize the parasitic effect of rise and fall time of the pulse, the measurement was repeated for a specific current using different pulse times. Then, getting the slope of displacement vs. time

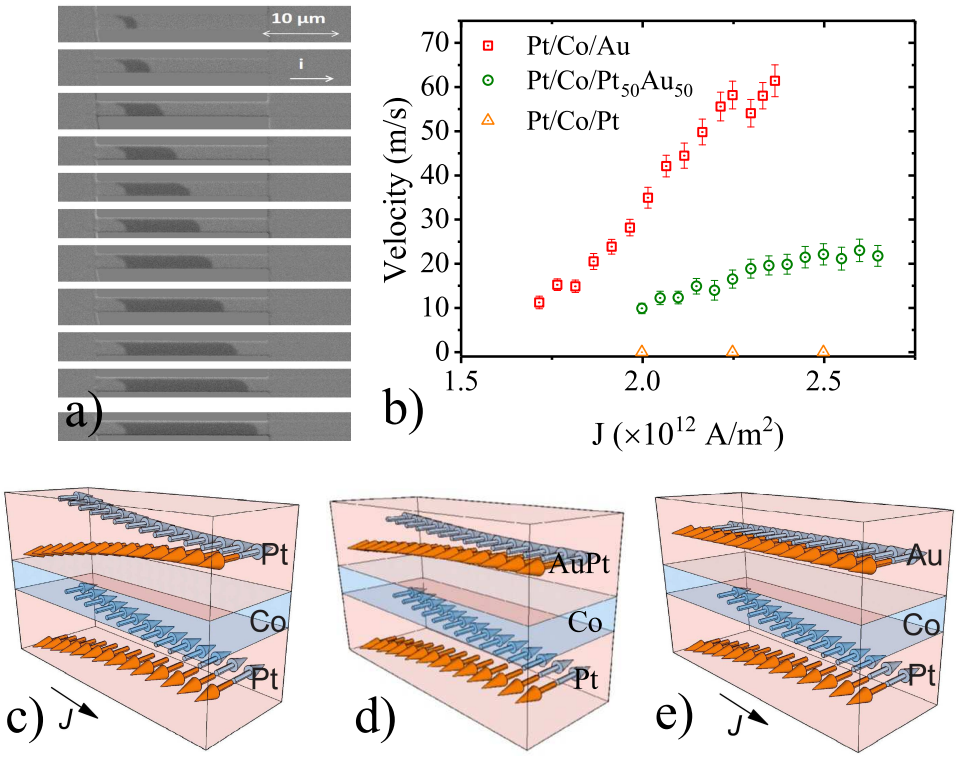

Figure 4.9: a) Series of subtracted Kerr images of current-induced DW movement using current density of 2.2×10^{12} A/m^2, each separated by 60 ns. DWs are always moving against the electron flow. b) DW velocity vs. current density for different top layers. Each point is an average of 5 measurements. Spin-Hall effect in c) Pt\Co\Pt, b) Pt\Co\Au$_5$0Pt$_5$0, and c) Pt\Co\Au. In Pt\Co\Pt, top and bottom interfaces of Co are facing opposite spin accumulation leading to zero net SOT while in Pt\Co\Au there would be almost no spin accumulation on top interface when a current is passing through the stack, hence Co will experience highest torque (Schematic courtesy of Aleš Hrabec).

for that particular current density, final velocities were rescaled. The data is shown in Figure 4.9.b. It is clear that in the case of Pt\Co\Pt, DWs are completely insensitive to applied current and as soon as Au is added to the top layer (*i.e.* symmetry is broken) the DW velocities are rising.

The zero velocity of Pt\Co\Pt is in agreement with the scenario of compensated SHE coming from the same layers at each side of the ferromagnet (Figure 4.9.c). As

4.9.d shows for the case in which there is 50% gold contribution in the top layer, the compensation would not be full anymore as the SHE in gold is negligible [42] and there is a stronger SOT coming from the bottom Pt layer, hence higher velocities. In the last case, cap layer of 100% gold has a negligible contribution to spin accumulation at the interface [42], and all of SOT comes from accumulated spins in Pt\Co interface (Figure 4.9.e). Consequently, we have the highest effective spin Hall angle, thus highest sensitivity to current, in these set of stacks.

It is worth to mention that the volume spin transfer torque which is needed to move the DWs is happening at much higher current densities that is applied here [142, 143]. Also, the fact that DWs always move against the electron flow shows the effect of spin-orbit torque in the movement of the DWs in the sample [144] and cancels out any doubt about spin-transfer-torque playing a role here [144–146].

4.5.3 Change of DW Velocity with InP field

DW velocities were also measured as a function of in-plane field H_{InP} applied along the current direction for up-down (UD) and down-up (DU) DWs. Figure 4.10 shows the DW velocities as a function of InP field. The fact that velocity of UD is decreasing with H_{InP}, while the DU DW's velocity is increasing, shows that both DWs have the same chirality. It, also, can be seen that at zero InP field both UD and DU domain walls are moving in the same direction for both samples. Both of these facts are indications of presence of DMI in the multilayers and promotion of homochiral Néel DWs.

As Bloch DWs would not move in presence of SOT [13], in regions that the wall is not Néel type ($H_{\mathrm{DMI}} \cong -H_{\mathrm{InP}}$), DW velocity is zero. This, again, agrees with theory as damping-like torque needs a component of magnetization parallel to the current, to be able to act on the wall. Such component is absent if the wall structure is Bloch. The field for which $v_{\mathrm{DW}} = 0$ m/s in AuPt is smaller than Au capped multilayer (8 mT and 49 mT, respectively). As this stopping field is proportional to the DMI strength [30], the results here are in agreement with previous observation of increasing DMI with Au concentration estimated with asymmetrical bubble expansion.

By increasing in-plane field from the stopping field, DW structure changes to Néel and the velocities are growing, also its sign is reversed on either side of this field. This sign reversal is in agreement with theory as it is mutual effect of spin Hall angle and domain wall chirality, which defines velocity sign, *i.e.* direction of motion. A high

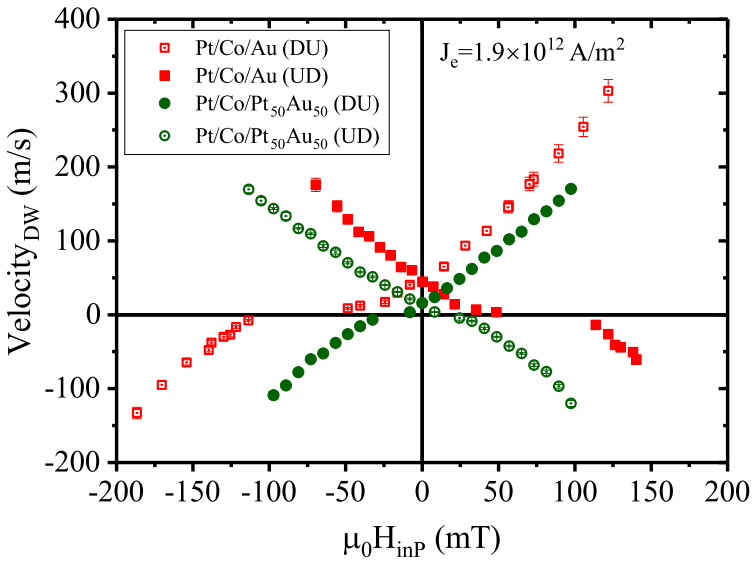

Figure 4.10: Change of current induced DW velocity with applied in-plane field for up-down (UD) and down-up (DU) DWs of different capping layers. The zero field region is when domain wall structure is Bloch like.

enough applied in-plane field can change the chirality of the wall, hence direction of motion.

Figure 4.10 also shows that the velocity achieved for the same InP field is higher in Pt\Co\Au than Pt\Co\$Au_{50}Pt_{50}$. This is an indication of higher effective spin Hall angle of for the Au capped sample. This velocity is scaling almost linearly with the applied InP field.

4.6 Discussion

In this chapter, epitaxial trilayers of Pt\Co\Au_xPt_{1-x} ($x = 0, 0.5, 1$) were investigated in terms of DMI and domain wall motion. The well-defined (111) orientation of multilayers was shown by high-angle X-ray diffraction patterns. The presence of the so called Pendellösung fringes around the main (111) peak is also an indication of uniformly strained layers and smoothness of the interfaces. The epitaxial structure is also confirmed using cross sectional STEM images showing lattice fringes.

Using in-plane magnetization loops one sees that the total magnetization in Pt\Co\Pt is the highest, which can be understood considering the induced moment in Pt. Sub-

Table 4.2: Magnetic properties of epitaxial Pt/Co/Au_xPt_{1-x} for the three different values of Au concentration, x. These are saturation magnetization M_s, uniaxial anisotropy constant $K_u = K_{eff} + \frac{1}{2}\mu_0 M_s^2$, DW width $\Delta = \sqrt{A/K_{eff}}$, depinning field H_d obtained from fitting with the creep law, thickness fluctuation δ used in the micromagnetic simulations, effective DMI constant D_{eff}, as well as the inferred handedness of domain walls.

x	M_s	K_u	Δ	$\mu_0 H_d$	D_{eff}	Chirality
-	10^3emu/cm^3	MJ/m^3	nm	mT	mJ/m^2	-
1	1.0 ± 0.1	1.2 ± 0.2	5.5 ± 0.9	72 ± 2	1.0 ± 0.3	Left
0.5	1.1 ± 0.2	1.1 ± 0.2	7 ± 1	56 ± 2	0.35 ± 0.09	Left
0	1.0 ± 0.2	1.0 ± 0.2	8 ± 1	39 ± 2	0.07 ± 0.07	None

tracting the induced platinum moment, the cobalt moment is estimated and used for other parameter calculations. All calculated data are summarized in table 4.2 where Δ is lowered with increasing gold concentration, an obvious consequence of rising K_u.

DW dynamics in epitaxial Pt\Co\Au_xPt_{1-x} multilayers have also been investigated. Using asymmetrical bubble expansion, the DMI strength of the samples was evaluated. DMI is negative (equivalent to left-handed chirality) and is getting stronger with increasing Au concentration, due to breaking the symmetry of the top and bottom layers. Moreover, vanishing DMI in Pt\Co\Pt system shows a very well-defined symmetrical stack, which was made possible by depositing epitaxial multilayers and displayed in STEM images of figure 4.2. This is not trivial, as there were many experimental studies reporting a finite (non-zero) value of DMI for polycrystalline deposited Pt\Co\Pt, coming from difference in Co-Pt interface quality in top and bottom of the ferromagnetic layer [12, 40, 41].

Symmetrical propagation of bubble domains was also used to investigate the different regimes of domain wall motion. The creep, depinning, and flow regimes are all recognizable from the data of three multilayers. The achievable velocity for the same driving field is growing as the broken inversion symmetry in the sample is increasing. Fitting the velocity curves with universal functions of the depinning and creep regimes [92, 140], material dependent parameters of T_d, H_d and velocity at the depinning field $v(H_d, T)$ were extracted which are all increasing with Au concentration in the top layer.

As a combination of depinning temperature and depinning field describes the shape of the pinning potential in the film (via density of pinning centres and height of pinning barrier) [92, 140], also considering the fact that both are increasing with broken inversion symmetry, one could say that pinning is getting stronger with Au concentration. This can be understood more easily knowing the fact that Co and Au are barely forming an alloy [147, 148], and Au is very weakly polarizable [34, 134] (in contrast to Pt [42, 149, 150]). So the interface of Co and Au will be more abrupt in comparison with a Co-Pt interface, for which the magnetic parameters are smeared out as a result of the proximity induced magnetization. Furthermore, STEM cross sections of Pt\Co\Au trilayers were showing higher interface roughness for the top layer in comparison with much smoother interfaces in Pt\Co\Pt. This higher roughness can potentially enhances the pinning, due to induced variations of FM thickness and changes in magnetic properties (the same assumption was used for definition of grains in simulation). This is also reflected in adequate thickness fluctuations for micromagnetic simulation, as it is rising with experimental depinning field. (Thickness fluctuations of the STEM specimen cannot be considered as a good reference for grain size, as image contrast is averaged through the depth of the membrane).

It was also stated that knowing T_d and $v(H_\mathrm{d}, T)$, the depinning velocity of the domain wall, v_T was calculated, which can give us the DW mobility for the case that there was no disorder in the system. Due to the high driving fields that are used in flow regime, one could assume that pinning/disorder is ineffective in those field spans. As a result, this mobility might be considered as the flow mobility of the DW. Consequently, the Gilbert damping factor was calculated using the mobility of DW in FIDWM which is increasing with Au proportion in the top layer. The results are shown in figure 4.11 alongside evaluated damping from 1D model and micromagnetic simulations. The Gilbert damping parameter for Pt and AuPt capped trilayers are very close for all these approaches. On the other hand, the value for Au capped cobalt has more than a two-fold difference for 1D and DW universality calculations. The Co-Pt interface was usually reported to have strongly enhanced damping in comparison to other Co\non-magnetic-metal interfaces [151–153], in general. It has also been reported that proximity would increase damping comparing Co\Pt, Co\Cu\Pt, and Co\Au multilayers [154], but there are contradictory articles in the literature which are suggesting that electron-electron interactions for weak spin polarizability of metals can cause enhancement of damping

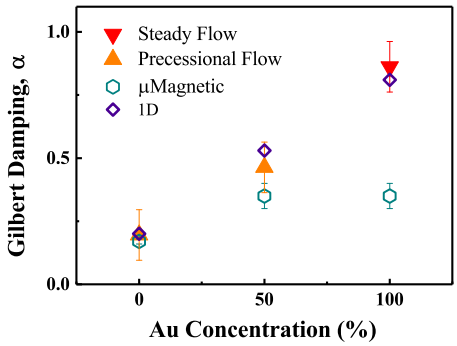

Figure 4.11: Changes of damping factor for different Au concentrations on the top layer of Pt\Co\Au_xPt_{1-x}. Results are from micromagnetic simulation and field induced domain wall motion are shown.

[155]. Here we see increasing of α with adding Au. Different theoretical and experimental investigations show that the ratio of damping factor in Co/NM with various metallic layers does follow quadratic relation with spin-coupling coupling in the NM layer [152, 153, 156], or following the sequence of Cu→Au→Pd →Pt [153, 157, 158]. These facts suggest that there is strong contributions from interface related damping [159] in present systems. Also, Barati *et al.* [152] showed that in Co-Au interfaces, the very interfacial atomic layer of Au and Co have the biggest contribution in damping, while for the case of Co-Pt the effect is extended to a few atomic layers. As a result, higher damping of gold-including samples in here, are most likely to be attributed to imperfection of interface in terms of surface roughness, disorder or interdiffusion. This hypothesis could be backed up with observation of higher thickness fluctuation in Au containing top layers from HR-STEM images. In addition, large enhancement of the Gilbert damping by intermixing in FM-NM interfaces has been shown for Fe-Pt multilayers [159].

Furthermore, assuming the DW as a 1D elastic interface, internal dynamics of the DW is not considered in the universal functions of creep and depinning evolution, but they will affect the velocity of the domain wall [160]. Not considering the DW's internal dynamics can only lead to an upper limit estimation for damping [161], due to the fact that all dissipation mechanisms are -implicitly- attributed to damping. While, recently, Yoshimura *et al.* showed that other energy dissipation channels like nucleation and annihilation of vertical Bloch walls might happen in samples with high DMI

[162]. This extra dissipation introduced by DW internal dynamics can sometimes go as high as supressing the linear velocity-field dependence for the DW [162]. It is also known that disorder hides Walker breakdown and the transition of steady to precessional regime in many magnetic structures, which adds a new way of energy dissipation during DW propagation [160]. So, it all suggests that complete micromagnetic simulations are actually the best way to obtain the precise damping parameter from FIDWM measurements. This is also the reason that the value of damping evaluated from DW mobility is usually much larger than this value coming from FMR measurements, emphasising on a contribution to the damping by DW propagation [163], which accounts phenomenologically for all possible magnetization-dissipation mechanisms.

4.7 Conclusion

Epitaxial multilayers of Pt\Co\Au_xPt_{1-x} (x=0, 0.5, 1) with controlled symmetry breaking were deposited and studied. The well-defined crystallinity of films were proved using high resolution STEM cross sectional images and X-ray diffraction. The magnetic characterization and controlled change of proximity effect in the samples made it possible to evaluate Co magnetization. Adding Au to the top layer increases PMA, and breaks the inversion symmetry, hence enhances the net DMI. We also showed that the strength of SHE in mentioned the epitaxial stacks of Pt\Co\X increase qualitatively with enhancing broken inversion symmetry. Both SHE and DMI suggest the presence of homochiral Néel walls in the system. Increasing contribution of Au in the top layer lead to rising of the depinning field and depinning temperature for the DW, suggesting a higher pinning for samples with Au. This is in agreement with the sharper interface of Co with Au, as proximity induced magnetism is not present. Moreover, field-induced DW motion was predicted with full micromagnetic simulation, where 1D model was not able to deliver reliable results in comparison with the experimental measurements. Lower values for Gilbert damping was evaluated using micromagnetic simulation, which may be grounded on the fact that DW motion includes other ways of energy dissipation that are not a part of Gilbert damping. This can also justify the higher values of damping that are usually reported from domain wall motion, in comparison with FMR.

At last, it is worth to mention that in conventional ferromagnets, permalloy is the accepted model system [138, 164] and GaMnAs is the case for magnetic semiconductors [165–167]. In thin films with broken inversion symmetry, CoFeB multilayers are often

used as a model system [30, 46, 128, 168], but the complications of B diffusion [128, 169] and the necessity of annealing in these systems [39] are not very favourable for such. Consequently, we propose these epitaxial trilayers instead. As the layers are epitaxial, comparison to theoretical predictions is more reliable in this case. The proposed model system can also be exploited for systematical study of DMI and SHE in a multilayer stack. The same approach can be used for other materials on each side of the ferromagnet and can be extended to study of skyrmionic structures. The study, also, can be extended to the physics of skyrmions which contain the same physics as the chiral walls, although expanded into two dimensions.

Chapter 5

Polycrystalline Multilayers of Pt\Co\Ir(t_{Ir})\Ta

5.1 Introduction

As was mentioned in previous chapters, chiral domain walls and skyrmions have a high potential to be used as basic components of next generation of magnetic recording media/processing devices. To be able to make use of them efficiently, one of the important targets is to achieve an optimal sequence of thin films for high DMI and SHE. Pt\Co\Ta multilayers experimentally showed high SHA [14] and skyrmionic structures were also reported in superlattices of these stacks [170]. It is also known that a Co\Ta interface has low DMI with the same sign as Co\Pt interface [29], so the resulting *"high"* DMI of such multilayers are not only optimal, but also less than what one can get with a single Pt\Co interface. On the other hand, experimental results and theoretical models revealed that the DMI of Co\Ir interface is opposite to the Co\Pt one [12, 29, 31]. So, inserting Ir underneath Ta was expected to enhance DMI. Considering these facts, structures of this study decided to be Ta\Pt\Co\Ir(t_{Ir})\Ta. In this chapter we will investigate the effect of increasing Ir thickness on the domain wall dynamics and DMI. Also, in discussing the features of asymmetrical bubble expansion, shortcomings of the simple creep model for evaluation of DMI [109] will be reviewed and the results will be compared to BLS measurements.

5.2 Samples

It was mentioned having Ir on top of Co is to enhance DMI in the system, which is mostly an interfacial effect (*c.f.* section 2.5.1). Hence iridium just needs to make an interface with Co, and should not be so thick to shadow any bulk originated spin Hall effect of Ta layer on top of it. As a result Ir thicknesses were changed between zero to 2.0 nm (figure 5.1). Polycrystalline multilayers were deposited on thermally oxidized Si substrate ($\sim$ 100 nm SiO_2). The base pressure was 7.0×10^{-8} Torr. The Ar partial pressure was 55sccm for all materials. The deposition power was 10W, 25 W, 12W, and 25W for Ta, Pt, Ir and Co, respectively. Deposition rates were calibrated by checking the thickness of superlattices of Co\Pt and Co\Ir, and thick monolayer of Ta as it was explained in section 3.2.3.

Some of the final deposited multilayers' structure were investigated using HRTEM and EDX. Figure 5.2 includes both image and EDX elemental distribution. Looking at the image, there seem to be some interdiffusion in different interfaces. Nevertheless, the

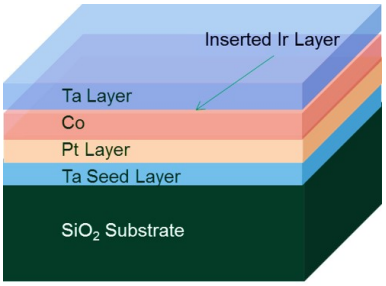

Figure 5.1: Structure of the deposited stack: SiO_2\Ta\Pt\Co(0.8 nm)\Ir(t_{Ir})\Ta (t_{Ir} = 0.0 - 2.0 nm).

contrast is good enough to distinguish all layers from the neighbouring ones (either by change of colour or change of crystallinity). As is clear in the image, Pt layer is highly textured and multi-grained and its crystallinity continues into Co and top Ir in several places. No crystallinity can be seen in the seed or capping Ta layer, emphasising the desired amorphous texture. It also should be noted that although the TaO_x is relatively thick, a thin Ta layer between the top oxidized Ta and Co is still visible, protecting the inner layers from oxidation.

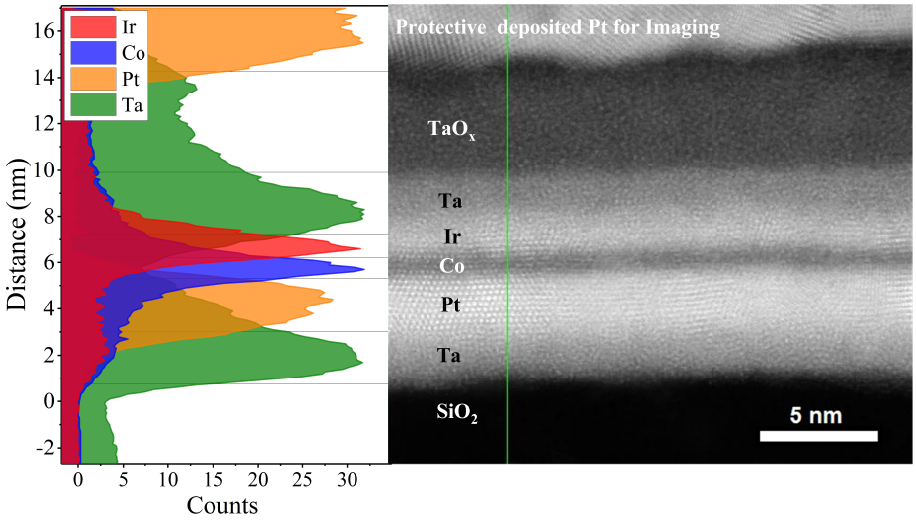

Figure 5.2: EDX spectrum and HRTEM HAADF image of SiO_2\Ta\Pt\Co\Ir(1 nm)\Ta, showing textured and clear distinguishable layers in the film. The preparation of TEM sample and imaging was done by Andreas Bischof and Marta D. Rossell in IBM-Zürich, respectivly

5.3 Magnetization, Anisotropy and Symmetric Exchange

Working towards a structure like Ta\Pt\Co\Ir(t_{Ir})\Ta, the first step was to grow a multilayer like Ta\Pt\Co\Ta with perpendicular magnetic anisotropy. So samples of Ta(4.0)\Pt(2.2)\Co(t_{Co})\Ta(4.0) with changing Co thickness were deposited on SiO_2 substrate with conditions mentioned in section 3.2.1. Polar MOKE loops for different Co thicknesses are presented in Figure 5.3. It is clear that samples with Co thickness less than 0.7 nm do not have out-of-plane anisotropy. When FM layer thickness is $t_{FM} > 0.7$ nm square hysteresis loops appear. The coercive field increases with Co thickness, saturates with the value of $\sim$ 7.5 mT and decreases sharply after 1.25 nm of Co. For Co thicknesses more than 1.3 nm the magnetic anisotropy rotates towards in-plane direction gradually (Figure 5.3.b).

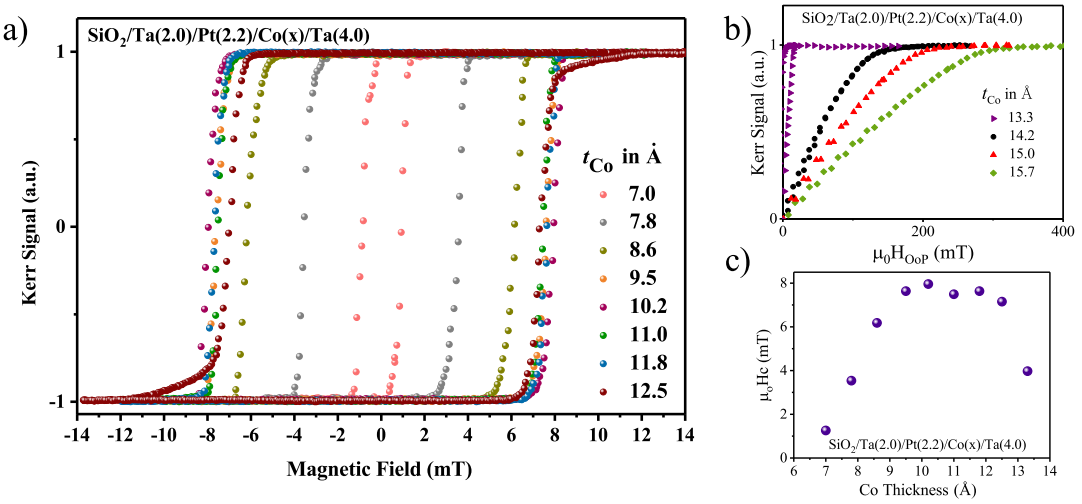

Figure 5.3: Polar MOKE information from SiO_2\Ta(2.0)\Pt(2.2)\Co(t_{Co})\Ta(4.0) stacks. a) Hysteresis loops for samples with Co thicknesses of 0.7-1.25 nm showing strong PMA. b) Gradual rotation of anisotropy into the plane of film for thicker Co thicknesses. c) Change of coercive field for samples in part (a).

These trilayers are building blocks of skyrmionic or other magnetic device structures for many of which the ability of switching at low magnetic fields is important, so the Co thickness of 0.8 nm was selected for final structure due to its low coercive field and having square hysteresis loop at the same time. The final structures are supposed to have a thin layer of Ir between Ta and the ferromagnetic material, thus multilayers of

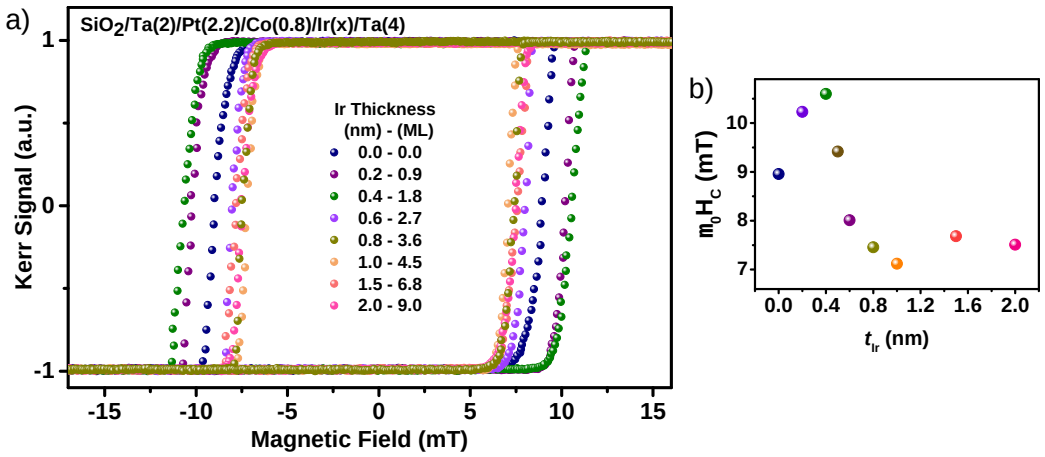

Figure 5.4: Polar MOKE measurements of SiO_2\Ta(2.0)\Pt(2.2)\Co(0.8)\Ir(t_{Ir})\Ta(4.0) stacks changing the Ir thickness from zero to 2 nm/9 monolayers(ML). a) Square shaped hysteresis loops show strong PMA in all samples. b) Change of coercive field for increasing t_{Ir}. We believe that for thicknesses of 0.6 nm and more there will be a continuous layer of Ir.

Ta(4.0)\Pt(2.2)\Co(0.8)\Ir(t_{Ir})\Ta(4.0) (t_{Ir}= 0.2 to 2 nm) were deposited on SiO_2. It is also important to keep the perpendicular magnetic anisotropy of the structure. As figure 5.4 shows, they all showed PMA.

The magnetization and anisotropy field, H_K, of the samples were measured by SQUID-VSM as explained in section 3.3.2. Saturation magnetization, M_S, is the areal moment divided by the nominal Co thickness. These values can be used to measure effective anisotropy, $K_{eff} = \frac{1}{2}\mu_0 M_S H_K$, and uniaxial anisotropy, $K_U = K_{eff} + \frac{1}{2}\mu_0 M_S^2$. As figure 5.5 depicts, M_S increases significantly as soon as there is some Ir in the system, which emphasises the presence of a dead-layer (DL) between Co and Ta plus proximitized magnetism in Ir. After that, M_S remains almost constant. The mean value of saturation magnetization $M_{S,avg} = 1.7 \pm 0.1$ MA/m is higher than magnetization of bulk Co, which can be attributed to proximity induced magnetization in Pt [149] and Ir [171]. The anisotropy field of the samples is slightly decreasing with Ir thickness, but all the values are between 0.6-0.8 T and the changes are, again, not significant ($H_{K,avg} = 0.72 \pm 0.07$ T).

It is known that usually a magnetic dead-layer of several atomic layers forms when a ferromagnetic material is placed next to Ta [172–182], which is believed to be on ac-

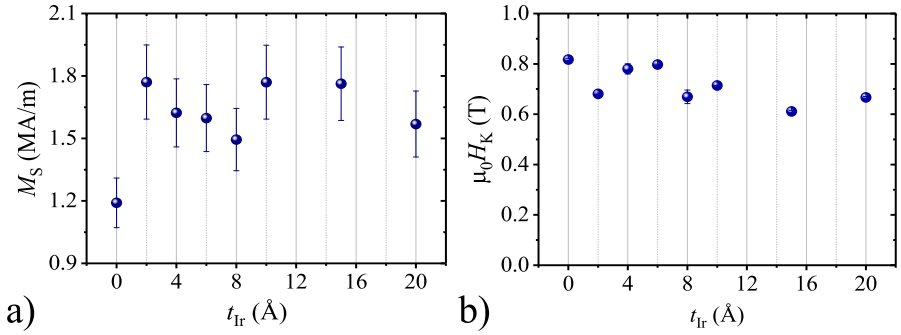

Figure 5.5: Changes of a) M_S and b) H_K for SiO_2\Ta\Pt\Co(0.8)\Ir(t_{Ir})\\Ta multilayers.

count of intermixing between Ta and FM layer [177–179, 181]. This results in deduction of effective thickness of the ferromagnetic material. Reported dead-layer thicknesses, t_{DL}, for Co-Ta and as-deposited CoFeB-Ta interfaces are shown in figure 5.6. Results from annealed films are omitted as annealing usually increases the dead-layer thickness through intensifying interdiffusion at the interface [40]. The values are changing between 0.2 nm and 0.58 nm for different interfaces. This discrepancy is trivial and inevitable as the interface quality is highly dependent on deposition conditions. But unfortunately we did not have multilayers with different Co thicknesses deposited on the same vacuum cycle as the multilayers in this chapter, so could not conclude a definite answer for the amount of dead-layer they might have.

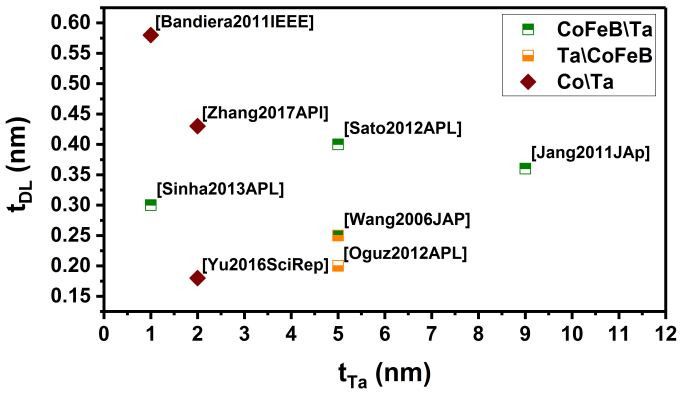

Figure 5.6: Reported values for thickness of magnetic DL in Co-Ta and CoFeB-Ta as-deposited interfaces as a function of Ta thickness.

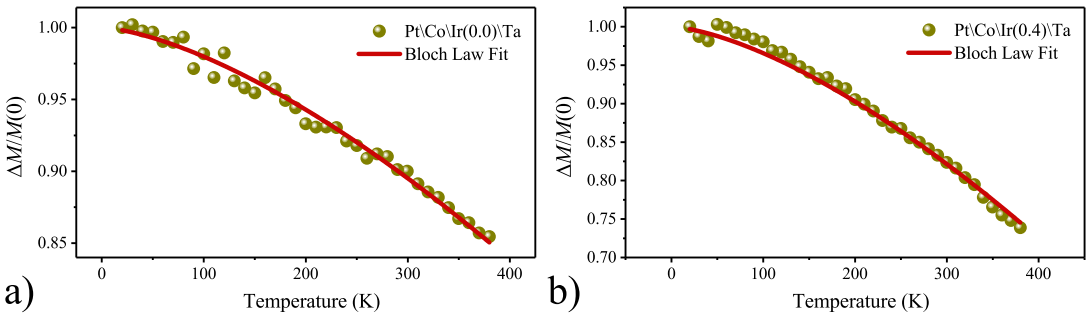

Figure 5.7: Temperature dependence of magnetization in a) Pt\Co\Ta, and b)Pt\Co\Ir(0.4)\Ta. The red line shows Bloch law fit.

Also, to measure the exchange stiffness parameter, A, the magnetization of Pt\Co\Ta and Pt\Co\Ir(0.4)\Ta samples as a function of temperature was measured by SQUID magnetometer. Fitting the data with Bloch $T^{3/2}$ law and following the procedure mentioned in section 4.3, exchange stiffness parameter was evaluated as $A_{\text{avg}} = 17.0 \pm 0.2$ pJ/m (Figure 5.7).

5.4 Ta Phase: β or α?

The structure of Ta layer is important since a large spin Hall angle would only arise from β-phase Tantalum, which has basically a tetragonal crystal structure (30 atm/unit-cell, a=10.194Å, c=5.313Å), and is reported to have high resistivity of 125-170 $\mu\Omega$.cm. On the other hand α-phase Ta has a BCC crystal with a lattice constant of 330.13 pm. Consequently, in this section we examine structure of deposited Ta layers of this research as due to technological interest it is important to have β-Ta.

Figure 5.8 presents XRD patterns with a distinct β-phase (002) peak at $2\theta = 33.7°$. No visible α-Ta peak can be seen in the pattern (expected position of α peaks are shown with black dashed vertical lines in figure 5.8), confirming a pure β-Ta thin film. (The broad peak centred around 45°, is caused by the instrument. This peak can be easily ignored because there are no α-Ta/β-Ta peaks expected in its vicinity). The pattern is also in agreement with other reports that say sputtered Ta thin film usually show (002) crystalline orientation on specific substrates, including SiO_2 [183].

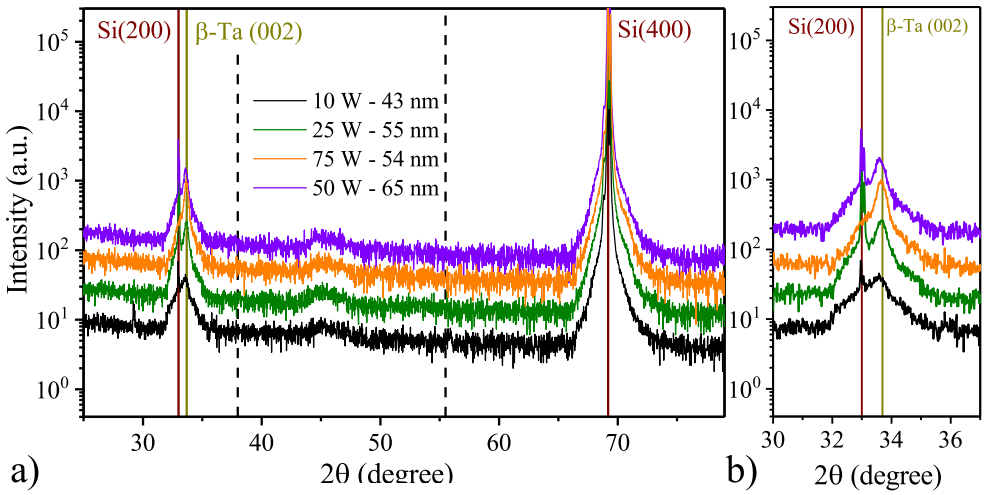

Figure 5.8: a) XRD patterns of Ta monolayer grown on SiO_2. b) Zoomed-in graph around the β-Ta (002) diffraction. Dashed lines are the expected position of α-Ta peaks. The broad peak at $\sim 45°$ is resulted from the instrument and can be ignored. The patterns for higher deposition powers are shifted upwards for clarification.

5.5 Different Regimes of Domain Wall Motion

As mentioned previously, DWs are studied since they have the prospect to be elementary components in future processing/storing media, where efficiency is heavily dependent on reliability of the DW's motion. Consequently, systematic study of DW motion using driving forces with various strength is essential for future applications. Stated in section 2.4.3, there are different regimes for DW dynamics for which numerous studies has been published [88, 89, 115]. Nevertheless, the systematic study of creep and depinning regimes' universal behaviour and pinning properties is limited to recent years and fewer reports [92, 94, 140, 184]. Here, pinning plays an important role and somehow dictates the DW dynamics, especially when the driving force is low. As a result, studying pinning properties quantitatively, by slight changes in the system, results in a better understanding of the DW motion in multilayers. Thus, in this section we investigate the domain wall motion in Pt\Co\Ir(t_{Ir})\Ta multilayers using bubble expansion (details of the measurement procedures are explained in section 3.4.1) and evaluate the three material-dependent pinning parameters: depinning field H_{d}, velocity at the depinning field $v(H_{\mathrm{d}}, T)$, and depinning temperature T_{d}.

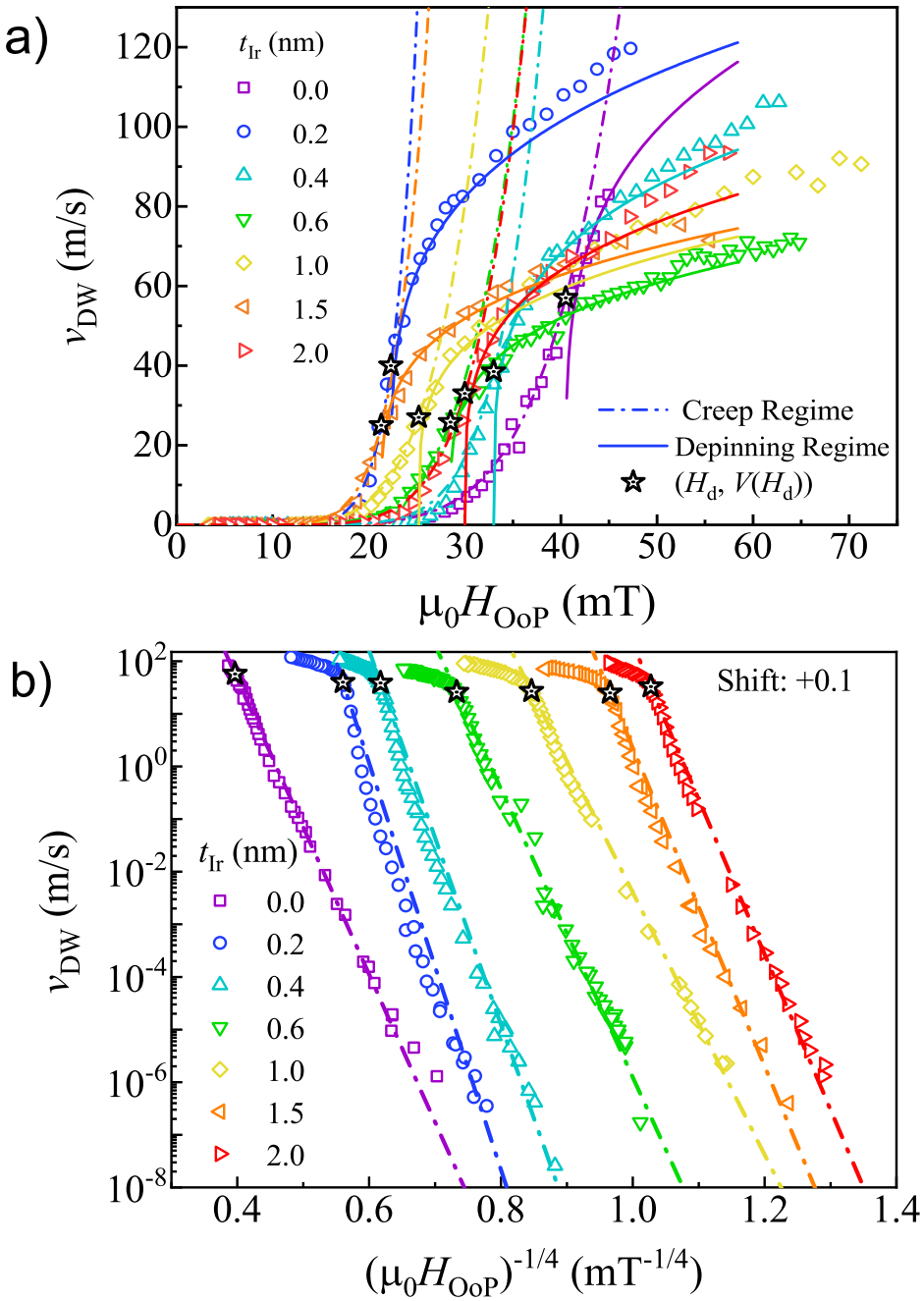

Figure 5.9: a) DW motion regimes in Pt\Co\Ir(t_{Ir})\Ta along with the fits to creep and depinning universal functions (Dashed-dot and solid lines, respectively). b) log(v) as a function of scaled driving field to highlight the compatibility of experimental data to the universal creep law. The stars show the inflection point which is correspondent to the depinning field, H_d.

To do that, the velocity of the moving domain wall was measured for increasing driving forces. Creep and depinning regimes can be identified in the experimental data, but the flow regime could not be seen for any of the samples (figure 5.9).

The data are fitted with the procedure explained in section 4.4.2 for universal creep and depinning regimes. The fitting curves are also shown in figure 5.9. As it can be seen in figure 5.9.b, at low fields $H \ll H_{\mathrm{d}}$, the velocity changes by nine orders of magnitude over a small field range of 20-30 mT, which is a characteristic of creep motion. The linear relationship of $\ln(v)$ to $(\mu_0 H)^{-1/4}$, again proves creep regime DW motion. The fact that fitting of this regime with $\mu = 1/4$ is working very well is showing that the domain wall motion is compatible with progress of a 1D elastic interface in 2D medium with random-bond short-range pinning potential [89, 92]. In the depinning transition, on the other hand, the change of DW velocity is not large comparing with creep regime and the DW goes out of depinning universal behaviour roughly after 10-60 mT. But still the universal behaviour of depinning seem to be conforming to the experimental data.

Depinning velocity can be calculated using equation 2.11. Figure 5.10 illustrates reduced velocity, v/v_T, as a function of reduced driving field, H/H_{d}. That all the data collapse onto a universal curve also emphasises the good agreement with the predicted depinning universal behaviour that can be observed over a large magnetic field span (H/H_{d} =1–1.5), which is comparable to the previous universality range reported for Pt\Co\Pt trilayers (up to 1.3 at RT [94]).

As was mentioned before, simultaneous investigation of the creep and depinning transition regimes yields three material (and temperature) dependent parameters, namely depinning field, H_{d}, depinning temperature, T_{d}, and velocity at depinning field, $v(H_{\mathrm{d}}, T)$. Variation of these fitting parameters with Ir thickness is presented in figure 5.11. It seems that for thicker Ir thicknesses $t_{\mathrm{Ir}} > 0.5$ nm, the material dependent pinning parameters (H_{d}, v_T, and T_{d}) are almost constant. Even for the DW mobility –which is a characteristic of the flow regime and not depinning– this statement appears to be true. One could say that above $t = 0.5$ nm, additional Ir thickness does not affect domain wall dynamics. On the other hand, when Ir is thin (*i.e.* $t_{\mathrm{Ir}} < 0.5$ nm) all the parameters show a non-monotonic change with the thickness. However, as there is not enough experimental data for thin Ir samples, it is hard to conclude a behaviour for changes. Moreover, the estimated T_{d} and H_{d} in these multilayers are both lower than reported

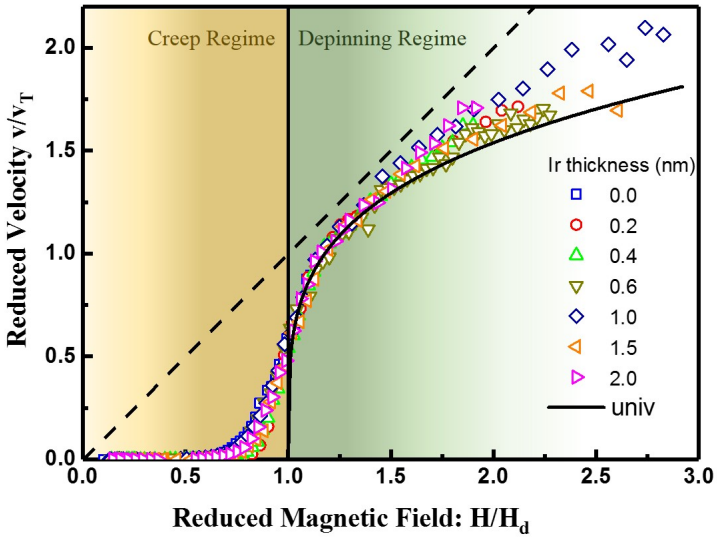

Figure 5.10: Reduced domain wall velocity with respect to reduced field for different Ir thicknesses. The tilted dashed line represents linear flow regime in which $v/v_T = H/H_\mathrm{d}$. The vertical solid line separates creep and depinning regime. The solid curve marks the universal depinning transition which is conforming to all experimental data in $1 < H/H_\mathrm{d} < 1.5$ range. All the samples leave the universal depinning regime at some point after 1.5 into the intermediate regime and reaching for flow.

room temperature values for Au\Co\Au [94] ($\sim$ 3 and 4 times less, respectively) which can be indicative of less pinning in the material.

Also, knowing that in the absence of pinning the DW velocity equates to depinning velocity, v_T, the mobility of DW can be calculated as $m = v_\mathrm{T}/(\mu_0 H_\mathrm{d})$ [140]. Except for the sample with $t = 0.2$ nm (in which the mobility $m = 3.1 \pm 0.7$ m/(s.mT) is higher than the one for the other thicknesses), m for the samples with Ir is almost the same with average value of $m = 1.8 \pm 0.2$ m/(s.mT). This value is much higher than $m = 0.48$ m/(s.mT) [88] and $m = 0.85$ m/(s.mT) [91] for Pt\Co\Pt, but close to $m = 1.6$ m/(s.mT) for Au\Co(0.8nm)\Au trilayers [185] which are obtained from fitting of the flow regime. The linear flow regime which represents this mobility is depicted by a dashed line in figure 5.10, which does not coincide with any of the experimental data. Consequently, we consider the experimental data after depinning universal behaviour to contain the intermediate regime between depinning transition and linear flow (*c.f.* figure 2.4). Unfortunately, higher fields could not be reached to show the flow regime,

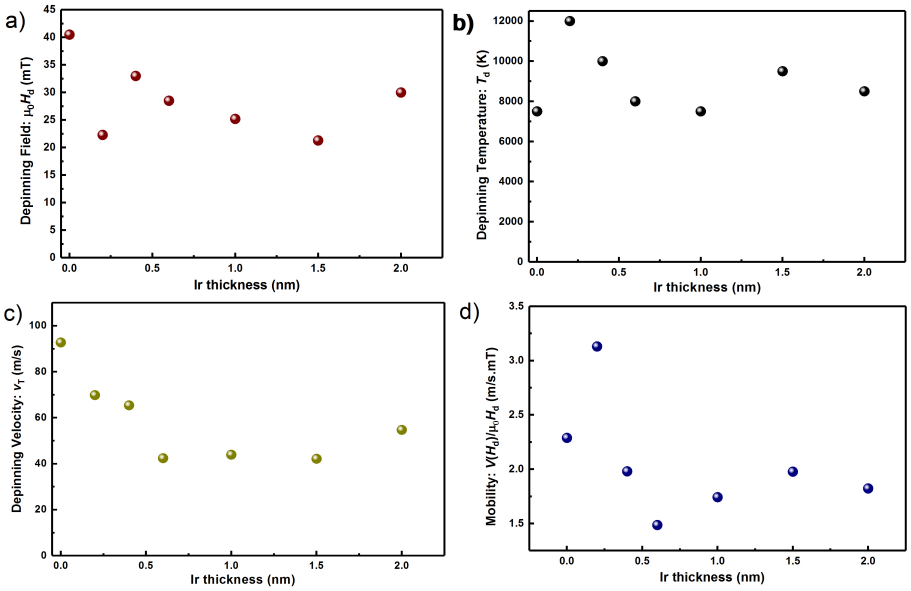

Figure 5.11: Changes of material dependent parameters a) H_{d}, b) $T_t extd$, c) v_T, and d) mobility resulted from fitting of universal creep regime and depinning transition for structures with different Ir thicknesses on top of Co.

due to multi-bubble nucleation and interference of bubble domains into each other.

Gilbert damping can also be determined by $m = \gamma\Delta/\alpha$ for steady flow regime (There has been no solution for the precessional flow). Hence, the average value for damping is $\alpha_{\mathrm{avg}} = 0.5 \pm 0.1$ which is comparable to the damping factor for other multilayers of Pt\Co [88].

Noticing the changes in velocity at depinning, $v(H_{\mathrm{d}})$, and depinning velocity, v_T, (Figure 5.12.a-b) it can be seen that they generally follow the increasing trend with H_{d}. Such behaviour was reported for different multilayer structures in [140]. Depinning temperature, on the contrary, does not show any systematic change with depinning field, suggesting a fluctuation of pinning properties.

As was observed in various figures throughout section 2.4.3, the parameters related to the multilayer with 0.2 nm of Ir are not following the general trend, and are often much higher or lower than values for other samples. Even the mobility of this multilayer is $m = 3.1 \pm 0.7$ m/(s.mT) is much higher than the rather common value of $m = 1.8 \pm 0.2$ m/(s.mT) for other films. This can be due to the fact that 0.2 nm of Ir is not actually a continuous layer and cobalt is facing both Ta and Ir in different places.

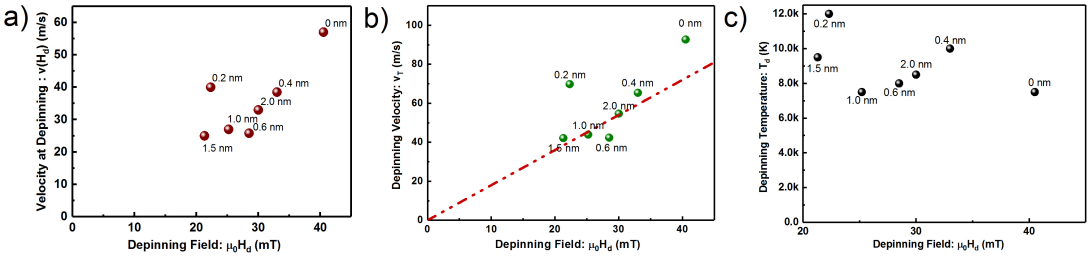

Figure 5.12: Variations of a) velocity at depinning $v(H_\mathrm{d}, T)$, b) depinning velocity v_T and c) depinning temperature T_d with respect to the depinning field. The inclined red line in (b) has slope of 1.8 m/(s.mT) showing the average value of m for Ir included multilayers (except for sample with 0.2nm of Ir).

Unfortunately, cross sectional TEM images could not reveal enough contrast to excatly distinguish between Ir and Ta in stacks with a very thin Ir layer.

5.6 Evaluation of DMI Field Using Asymmetric Bubble Expansion

Using the bubble expansion method, as explained in sections 2.5.2 and 3.4.1, the evolution of DW propagation velocity changing with applied in-plane field was measured. Figure 5.13 clearly shows that v vs. H_InP graphs do not just show a parabolic curve with a shift of minimum value from zero, H_offset, as is emphasized in Je's model [109]. One can see that the right and left walls show same trends, but considering the minimum of the graph neither of them have a symmetric change in either side of this value. This is in contrast with predictions of the model presented in figure 2.7 and other published reports of asymmetrical bubble expansion [12, 39, 44, 109]. A closer look also reveals that in some graphs (structures with 0.2, 0.4, and 0.6 nm of Ir) velocities of left DW (LW) and right DW (RW) meet up at high enough in-plane fields. Moreover, there are some step-like features in the velocity versus field curves, which cannot be dependent on local pinning fields as they seem to happen for both walls almost symmetrically. Consequently, it is clear that behaviour of present multilayers are not as simple as what Je *et al.* [109] and Hrabec *et al.* [12] explained. There were also a few other reports [38, 41] stating that they were unable to describe their experimental data with the theory and method Je *et al.* [109] used. This indicates that the currently used

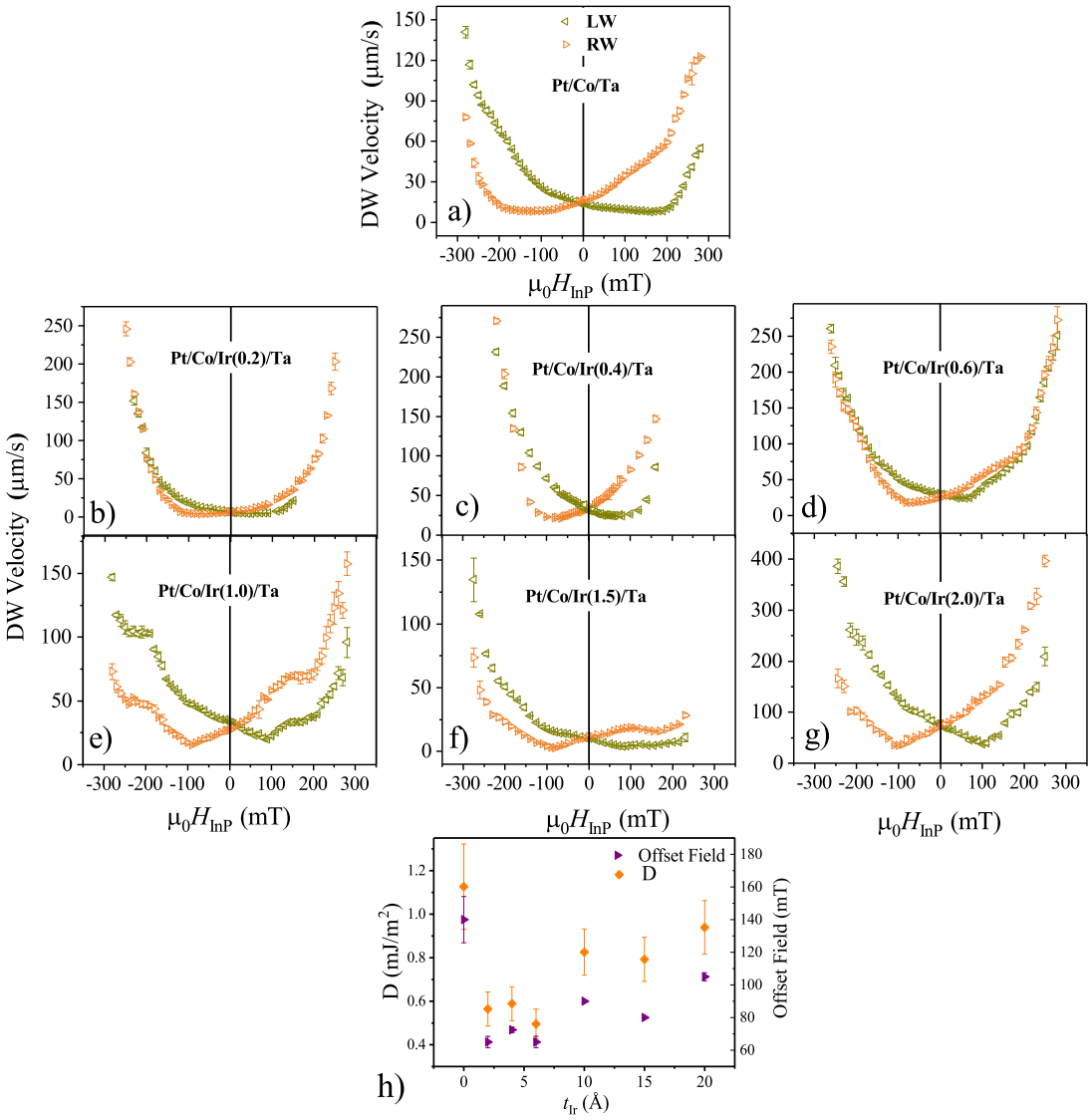

Figure 5.13: a-g) Velocity for DWs on the left and right side of the magnetic bubble (LW and RW, respectively) along the direction of in-plane filed vs. applied InP field, $\mu_0 H_{\mathrm{InP}}$, for different Ir thicknesses in Pt\Co\Ir(t_{Ir})\Ta multilayers. h) Variation of offset field (where the velocity is minimum) and the DMI factor calculated from it (the values are averaged for the LW and RW).

method is not universal and should be used with great care. Lavrijsen *et al.* [41] said that interpreting DMI as a simple in-plane field might be too simple, or other factors like tilting of domain wall magnetization with in-plane field should be also included in the theory. Vaňatka *et al.* [38] believe that exclusive relation of domain wall velocity to domain wall energy cannot be general and pinning potential landscape might also play a big role. As a result, measuring DMI of the present samples is not as straightforward as expected at first and needs more investigation.

Nevertheless, if we ignore all these anomalies and still follow the same argument in [12] and [109], H_{offset} would be where the wall is changed to Bloch type with highest domain wall energy, hence $H_{\text{InP}} = -H_{\text{DMI}} = H_{\text{offset}}$. Accepting this assumption, figure 5.13.h displays that unexpectedly, inserted Ir layer results in massive decrease in DMI field when compared with the sample that has no Ir (*i.e.* Pt\Co\Ta). This is counterintuitive, as *ab initio* calculations reported that Ir\Co interfaces are expected to have opposite DMI to Pt\Co ones [31]. Thicker Ir layer seems to help recovery of a little bit of lost DMI, but still not as much as expected. In the contrary to the analytical calculations, Kim *et al.* [186] also published some experimental results of Ir/Co having the same sign of DMI as Pt/Co interface using BLS to evaluate the DMI. (This will be discussed in more details in section 5.9).

5.6.1 Checking Creep Regime

As mentioned in section 2.4.3, domain wall movement for asymmetrical bubble expansion is assumed to be in the creep regime, in which DWs act as elastic interfaces and their velocity should obey creep law 2.9. So, to prove creep propagation of the wall, $\ln(v)$ should have linear proportionality to $H^{-1/4}$ when DWs are driven with an OoP field. The creep law was checked for samples in absence and presence of a constant InP field to make sure that the DW motion will follow the creep universality class. Figure 5.14 depicts this linear relationship for Pt\Co\Ir(0.6 nm)\Ta, which is present even in presence of high in-plane fields. Even the highest achievable in-plane field will not change the domain wall dynamics or pinning properties of the system so that the DW goes out of creep regime with exponent $\mu = 1/4$.

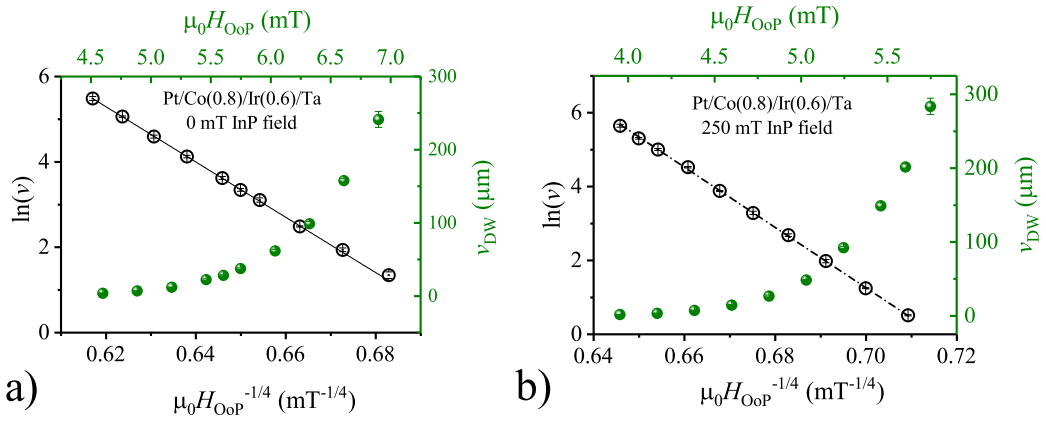

Figure 5.14: Investigation of creep propagation of the DWs: a) without any applied in-plane field, b) in presence of high in-plane field for Pt\Co\Ir(0.6)\Ta, which shows DW propagation follows creep regime even when high InP field is applied.

5.6.2 Asymmetrical Change of Relative DW Velocity With In-Plane Field

Following the arguments of the model (section 2.5.2), increasing the in-plane field to be larger than the DMI field, the domain wall energy should decrease on one side (where H_{DMI} inside the DW is parallel to H_{InP}) and increase on the other side of the bubble (where H_{DMI} is anti-parallel to H_{InP}). So, it is expected that in the former case DW always moves faster than the latter and velocity asymmetry for these two walls gets larger with InP field. In this way, there expected to be a point that magnetization in the domain wall, all around the bubble, is aligned with applied in-plane field (Figures 5.15.c and 5.16.a). Model of Je *et al.* [109] explains the situation up to this point.

On the contrary, in the present multilayers, propagation of bubble domains will be, again, symmetric for high enough in-plane fields as is clear in figure 5.15.d. This is not just limited to one sample, and changing the nucleation point to another site on the sample presents the same behaviour, therefore the effect is not a result of local parameters, either.

In this way, taking the difference of wall velocity for right and left domain walls of every propagated bubble and divide it by sum of the velocities, the changing of asymmetry can be seen clearly. As stated before, using equations 2.18, 2.19 and 2.20, velocity asymmetry of the walls is expected to reach a saturated value as figure 5.16.a

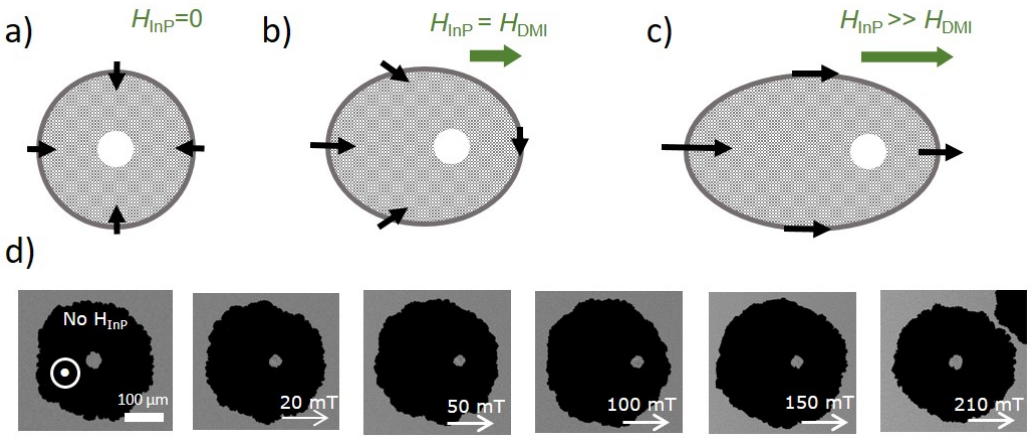

Figure 5.15: Change of magnetic domain shape and Néel wall magnetization with in-plane field, comparing theory and experimental results: a) LH Néel wall will expand symmetrically with OoP field. DMI field manifests as an InP field parallel with DW magnetization. b) Competition between H_{DMI} and H_{InP} implies direction of magnetization inside the DW. Where $H_{\mathrm{DMI}} = H_{\mathrm{InP}}$ theory expects the right wall to take Bloch form. c) InP field is high enough to align all magnetizations with its direction. Theory does not support any DW configuration after this point. d) Kerr microscope images from Pt\Co\Ir(0.6)\Ta with increasing applied InP field, the propagated bubble domain changes from being symmetrical for no InP field to asymmetrical for medium fields, but it changes back to symmetrical propagation for higher magnetic fields which is unexpected.

represents. But it is clear from figure 5.16.b-c that in case of these investigated multilayers this saturation condition does not happen for present multilayers. Instead there is a peak which after difference of velocity for left and right wall is decreasing and for some cases reaches to zero in the available in-plane field range. It is also interesting to mention that for samples having relatively thicker iridium the changing pattern of velocity asymmetry is different comparing to ones with very thin Ir (about 2 atomic layers) (Figure 5.16.b-c). This difference of behaviour for thick Ir samples was also observed in DW dynamic's related parameters in section 5.5.

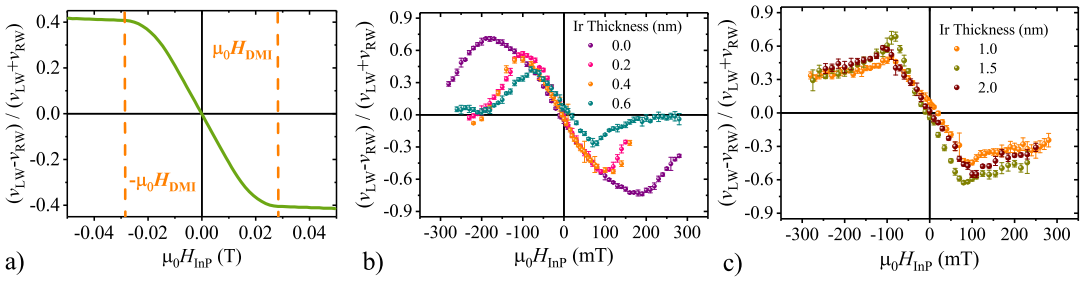

Figure 5.16: Difference between right and left DW velocities normalized to their sum, $(v_{RW} - v_{LW})/(v_{RW} + v_{LW})$, as a function of in-plane field, a) extracted from equation 2.20 which predicts a saturated value for velocity asymmetry (Graph is courtesy of Simone Moretti). Experimental results for multilayers with b) thin and c) thick Ir layers.

5.7 DMI Evaluation Using BLS spectroscopy

In addition to bubble expansion, we used Brillouin light scattering to evaluate the DMI of the multilayers. It was explained in section 2.5.3 that BLS is using propagation nonreciprocity of SWs in thin films with DMI, in contrast to bubble expansion which benefits from changes of bubble domain's growth when it is exposed to both InP and OoP magnetic fields. This nonreciprocity of SWs propagation results in Stokes and anti-Stokes frequency peaks which are offset from symmetric positions about the elastic peak. The offset changes sign depending on polarity of magnetic saturation.

Knowing the anisotropy field of the films, large enough in-plane fields were applied to make sure of their in-plane saturation. Then, the Damon-Eshbach configuration (explained in section 3.4.3) was used to measure the frequency shift of backscattered light. Normalized experimental data on multilayers with changing Ir thickness are shown in figure 5.17. It can be seen that the frequency shift changes direction with respect to the direction of saturation magnetization (black and red data in figure 5.17). The data were fitted with a Lorentzian function to get the peak position, which corresponds to the frequencies of Stokes (negative frequencies) and anti-Stokes (positive frequencies) processes with a fixed wavevector of $k = 16.7\mu\text{m}^{-1}$.

The resulted frequency shift, Δf, is firstly decreasing with Ir thickness and reaches an almost constant value for samples with more than 0.5 nm of Ir (figure 5.18.a). It should be noted that surface anisotropy cannot be considered as the dominant con-

tribution as the cobalt is ultrathin. For thick films where $(k_{SW}/t_{FM}) \ll 1$ (t_{FM} is ferromagnetic thickness) does not apply spin waves will be localized to top and bottom surfaces depending on the direction of travel and will cause a nonreciprocity even in absence of DMI [187], but such frequency shift should be negligible here because the ferromagnetic layer thickness is only 0.8 nm. The change in the peak frequency cannot also be attributed to the dipolar coupling as the dipolar effect, unlike DMI, would not change its sign with respect to magnetization direction [118]. D values were calculated from Δf for each sample following the process described in section 2.5.3,

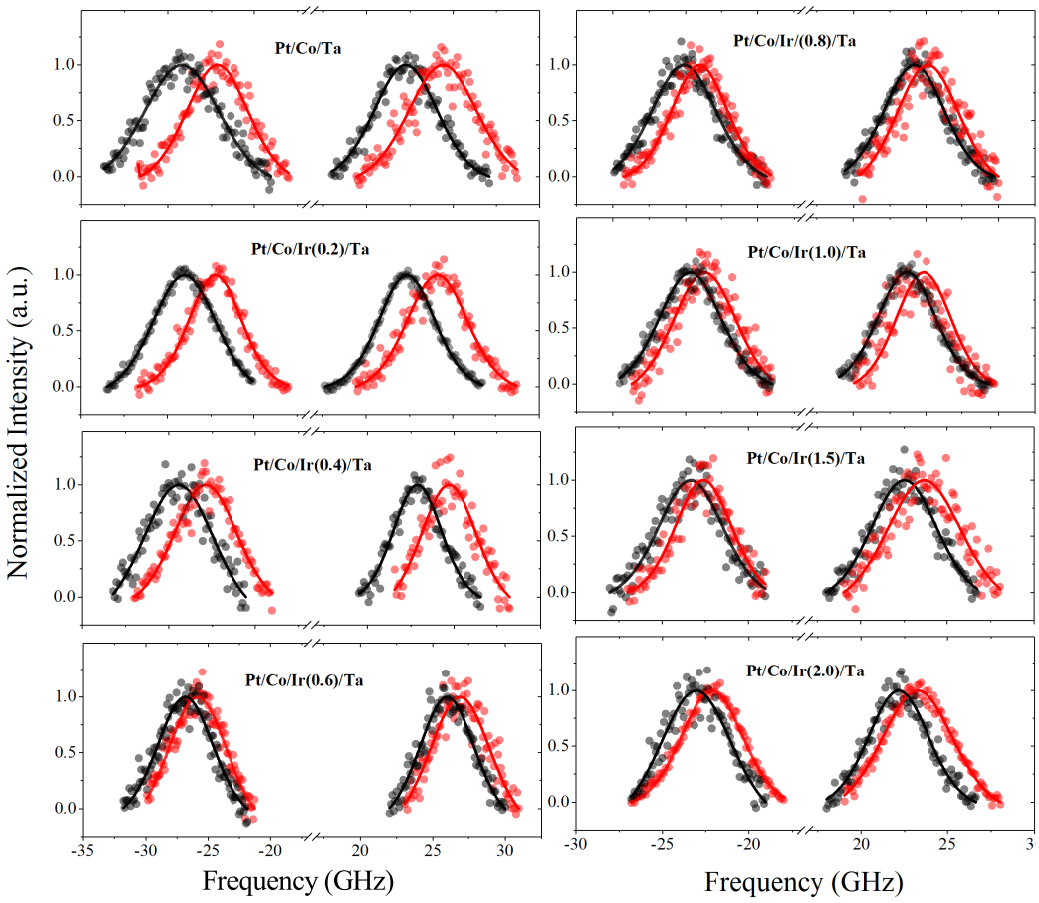

Figure 5.17: Normalized BLS spectra measured for different Pt\Co\Ir(t_{Ir})\Ta for opposite inplane saturation directions in black and red. The peaks with negative and positive frequency is related to Stokes and anti-Stokes reflection, respectively. Solid lines are Lorentzian fits.

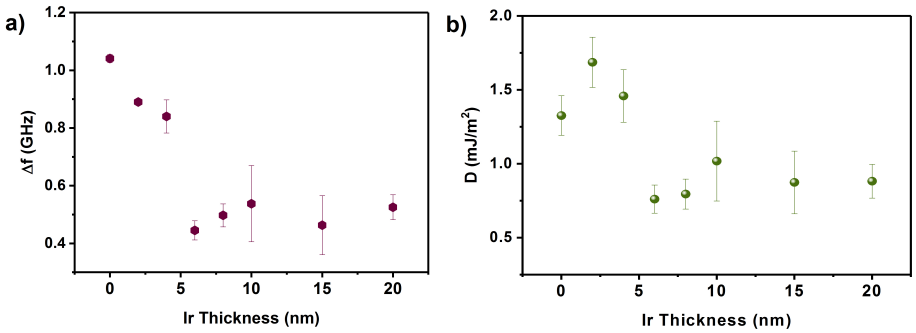

Figure 5.18: a) Frequency shift and b) DMI factor resulted from BLS experiments for various Ir thicknesses. .

and are presented in figure 5.18.b. Almost the same trend as Δf reflects into the DMI variation with Ir thickness, except for Pt\Co\Ta which might be an underestimation due to neglecting the probable dead-layer formed at the interface of Co and Ta.

5.8 Micromagnetic Simulation

In this section, theoretical analysis on response of DW velocity to applied in-plane field is discussed. All the work here is done by Joo-Von Kim (C2N, Paris-Sud University) and is just added for further discussion on the results. The basic assumption of the analysis is that the dominant contribution to in-plane field dependence is from changes of depinning field H_{d} with H_{InP} which reflects into variation of velocity prefactor v_0 and pinning potential ΔE in equations 2.9 and 2.10, respectively.

All the input parameters are from the experimental results for Pt\Co\Ta multilayer. The simulation mesh is a 1×0.5 μm^2 ferromagnetic film with 0.8 nm thickness which is divided into $512 \times 1024 \times 1$ cells. The average 10 nm sized cells have random values of perpendicular anisotropy constant K_u distributed around experimental value of 1.38×10^6 MJ/m^3 with 17.5% spread. The magnetization outside the mesh is the same as inside along the x direction but periodic boundary conditions are used along the y direction to make an infinitely large system. A DW is set and relaxed to the disorder distribution around the centre of the simulation grid ($x = 0$) which has an up-domain on the left and a down-domain on the right. A uniform OoP magnetic field is applied along z and increases with steps of 2 mT. At each step the system will be relaxed and the OoP field for which the DW depins will be taken as the depinning field for a

particular constant InP field. For each value of H_{InP}, the same procedure is repeated for 100 random realizations of disorder. The disorder is set so that the value of H_{d} at zero in-plane field is close to experimental estimated H_{d}.

Changes of depinning field, H_{d} with respect to in-plane applied field is shown in figure 5.19 for various D constants. It can be seen that the asymmetry in H_{d} is increasing for higher D values which leads into variation of pinning potential ΔE and then domain wall velocity as stated before. It should also be noted that the behaviour of H_{d} with respect to H_{InP} is very similar to changes of domain wall elasticity in [188].

Including smoothed function of H_{d} changes in equations 2.10 and 2.9, the domain wall velocity curve as a function of H_{InP} can be reproduced for increasing values of D. As is presented in figure 5.20, $D = 2$ mJ/m^2 data not only imitates the general asymmetric behaviour of the experimental curve, but also predicts the minimum point quiet well. More importantly, simulation results replicate the velocity divergence of opposite domain walls at high InP fields, a feature which was not expected in the Je's model for domain wall velocity based on changes of domain wall energy with in-plane applied field [109] (*cf.* figure 5.16). Also, DMI fields corresponding to different D values is shown by dashed vertical lines in figure 5.20.a-d along with simulated velocity curves. One can clearly see that in figure 5.20.d where DMI field is close to the minimum point of experimental data, H_{offset}, the simulated curve does not coincide with experimental one for most of the region covered. As a result, it should be noted that taking the minimum point as H_{DMI} may lead to significant underestimation of DMI field, hence

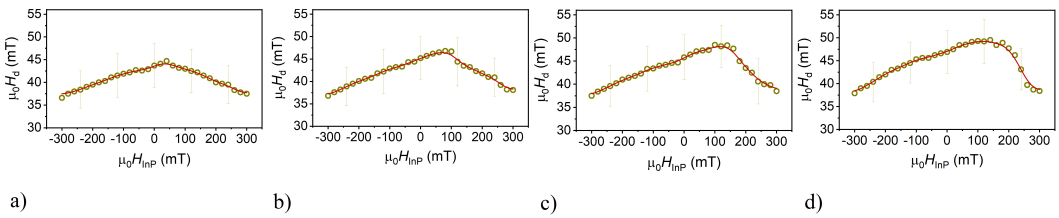

Figure 5.19: Variation of depinning field with in-plane applied field for four different values of DMI factor D: a) 0.5 mJ/m^2, b) 1.0 mJ/m^2, c) 1.5 mJ/m^2, and d) 2.0 mJ/m^2. The circles represent the average H_{d} value and the error bars indicate standard deviation for the different disorder distribution. The trend of H_{d} change with H_{InP} for each distribution is the same as the solid (red) curve which represents a smoothed function. All from micromagnetic simulations.

D constant of the system.

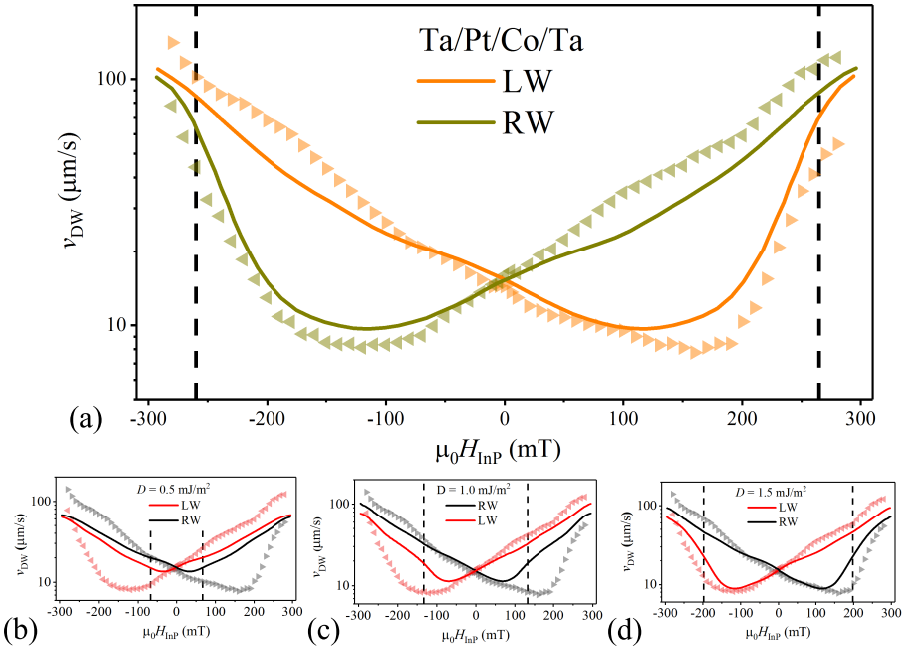

Figure 5.20: Comparison of micromagnetic simulation and experimental results for domain wall velocity as a function of in-plane field, H_{InP}, for different values of the DMI factor, D: a) 2.0 mJ/m^2, b) 0.5 mJ/m^2, c) 1.0 mJ/m^2, and d) 1.5 mJ/m^2. The triangles are the experimental data of Pt\Co\Ta. The solid lines are curve from micromagnetic simulations. The dashed vertical lines are representing DMI field extracted from simulation.

5.9 Discussion

The domain wall dynamics and Dzyaloshinskii-Moriya interaction in polycrystalline SiO_2\Ta\Pt\Co\Ir(t_{Ir})\Ta multilayers have been investigated. It was shown that the Ta seed layer has β-phase and all samples have perpendicular magnetic anisotropy which is expected to originate from Pt-Co interface. The changes of saturation magnetization, M_{S}, and anisotropy field, H_{K} were also presented in figure 5.5 and table 5.1. We believe that M_{S} of the sample with t_{Ir}=0 (*i.e.* Pt\Co\Ta) is underestimated because of the most probable dead-layer formed in Co-Ta interface. This underestimation of saturation magnetization will return into other calculated parameters that are dependent on M_{S}

such as DMI factor strength. Putting M_S of this multilayer aside, for the rest of the films saturation magnetization does not vary significantly and has the average of $M_{S,avg} = 1.7 \pm 0.1$ MA/m. H_K has also the same situation with slight reduction in value with Ir thickness, t_{Ir} and average of $H_{K,avg} = 0.72 \pm 0.07$ T.

Using asymmetric bubble expansion, chirality of the domain walls in all multilayers proved to be left-handed. This was reported many times in literature for Pt-Co interfaces from *ab initio* calculations [29, 31, 189] and experimental investigations [42, 46, 107], also for Pt\Co\Ir multilayers [12, 139, 190].

Investigating the domain wall dynamics with perpendicular magnetic driving field reveals that universal creep and depinning regime (equations 2.9 and 2.13) can be fitted to the experimental data with a very good agreement. On the other hand, evaluation of DMI with asymmetric bubble expansion method seems not to be in accordance with the simple creep model of Je *et al.* [109], in which the in-plane field dependence of the domain wall velocity appears exclusively in the domain wall energy, σ_{DW}. In their model, they assumed that pinning strength, roughness of domain wall and correlation length of the disorder are all independent of in-plane applied field [109]. There were reports for which this model was able to describe the results [39, 44, 191, 192], but further experimental investigations revealed that these assumptions are not always true. For instance, Soucaille *et al.* [35] mentioned change of their domain wall roughness with InP field, and here we showed that depinning field (*i.e.* depinning strength) is also changing with H_{InP}. Moreover, exclusive change of σ_{DW} with H_{InP} could not predict divergence of domain wall velocities for opposite sides of the bubble at high enough InP fields as it was reported in this chapter (*c.f.* figure 5.15 and 5.16) and attributed to probable change of depinning field with H_{InP} (*c.f.* section 5.8). The imperfection of this model was put into more question when the behaviour of v_{DW} curve was not as symmetrical as it expected to be (*c.f.* figure 5.13 and [35]), also not even close to a polynomial curve with a single minimum value [38, 41]. All in all, it seems that using Je's model to evaluate DMI from asymmetrical bubble expansion is not as straightforward as it was expected to be, and there are some anomalies that need to be studied and investigated more.

Knowing all the above, we still assumed that the minimum point of the v_{DW} vs. H_{InP} equals to H_{DMI} and calculated D from it. The DMI of the multilayers was also estimated using Brillouin light scattering. Figure 5.21 shows the D values evaluated

Table 5.1: Derived parameters of polycrystalline Pt\Co\Ir(t_{Ir})\Ta for different Ir thicknesses t_{Ir}. Parameters are coercive field H_{c}, saturation magnetization M_{S}, effective anisotropy K_{eff}, DW width Δ, DMI constant evaluated using asymmetric bubble expansion D_{BE} and BLS D_{BLS}, DW mobility m, depinning temperature T_{d} and depinning field H_{d}.

t_{Ir}	H_{c}	M_{S}	K_{eff}	Δ	D_{BE}	D_{BLS}	m	T_{d}	$\mu_0 H_{\mathrm{d}}$
nm	mT	MA/m	MJ/m^3	nm	J/m^2	J/m^2	m/(s.mT)	K	mT
0.0	9 ± 1	1.2 ± 0.1	0.49 ± 0.05	5.9 ± 0.5	1.1 ± 0.2	1.3 ± 0.1	2.3 ± 0.4	7500 ± 200	40 ± 2
0.2	10 ± 1	1.8 ± 0.2	0.60 ± 0.06	5.3 ± 0.4	0.56 ± 0.08	1.7 ± 0.2	3.1 ± 0.7	12000 ± 500	22 ± 2
0.4	11 ± 1	1.6 ± 0.2	0.63 ± 0.06	5.2 ± 0.4	0.59 ± 0.08	1.5 ± 0.2	2.0 ± 0.4	10000 ± 200	33 ± 2
0.6	8 ± 1	1.6 ± 0.2	0.64 ± 0.06	5.2 ± 0.4	0.50 ± 0.07	0.8 ± 0.1	1.5 ± 0.3	8000 ± 200	29 ± 2
0.8	7 ± 1	1.5 ± 0.2	0.50 ± 0.06	5.8 ± 0.5	———	0.8 ± 0.1	———	———	———
1.0	7 ± 1	1.8 ± 0.2	0.63 ± 0.05	5.2 ± 0.4	0.8 ± 0.1	1.0 ± 0.3	1.7 ± 0.4	7500 ± 200	25 ± 2
1.5	8 ± 1	1.8 ± 0.2	0.54 ± 0.05	5.6 ± 0.5	0.8 ± 0.1	0.9 ± 0.2	2.0 ± 0.4	9500 ± 200	21 ± 2
2.0	8 ± 1	1.6 ± 0.2	0.52 ± 0.05	5.7 ± 0.5	0.9 ± 0.1	0.9 ± 0.1	1.8 ± 0.4	8500 ± 200	30 ± 2

by these two techniques. Overaly, BLS results show larger DMI strength than values from minima in the bubble expansion. This phenomenon has been reported before [35, 190]. In general, estimated D from BLS can be considered as an averaged value for the sample as it is based on propagation of spinwaves and local fluctuations of magnetic properties in the sample will be ineffective [193]. Whereas, bubble expansion depends on the propagation of a bubble domain, the creation of which is related to existence of nucleation points in the film. These nucleation points are mostly local defects and can lead to inhomogeneous effective anisotropy or exchange stiffness. These in turn mirror into local changes of DW thickness width Δ, hence estimated DMI from asymmetric bubble expansion [35]. The sensitivity of domain wall dynamics to local fluctuations can also be seen in figure 5.19 where there is a big standard deviation for resulted H_{d} values for different distributions of disorder in micromagnetic simulations. This big standard deviation is present despite the fact that all the input macroscopic experimental values for the system are still the same. So, equating H_{DMI} from H_{offset} (the in-plane field at which velocity curve shows a minimum) may lead to significant underestimation of the DMI. In conclusion, great care is needed when measuring DMI, as different techniques on same samples do not necessarily result in the similar values.

It is good to mention, that for the case of $t_{\mathrm{Ir}} = 0$, the magnetic dead-layer [172–182] leads to an underestimation of M_{S} due to the reduction of the effective thickness of the ferromagnetic material. This reflects into the calculation of other parameters for this stack including the DMI strength, D. Nevertheless, if we take the average value of saturation magnetization as this sample's M_{S}, the DMI strength will be $D_{\mathrm{BLS}} = 1.8\pm0.1\ \mathrm{mJ/m^2}$ and $D_{\mathrm{ABE}} = 1.6\pm0.3\ \mathrm{mJ/m^2}$ for BLS and asymmetric bubble expansion (naïvely taking H_{DMI} to be the velocity minimum), respectively. The D_{BLS} value is very close to $D_{\mathrm{sim}} = 2.0\ \mathrm{mJ/m^2}$ the value used in the simulations in figure. 5.20.a. All these calculated values are shown in figure 5.21.

Figure 5.21 also indicates that increasing the heavy metal thickness after $t_{\mathrm{Ir}} = 0.5$ nm does not change the DMI significantly, which is in good agreement with interpreting DMI as a purely interface effect [193]. This could be seen in two ways. First, after such a thickness one can be certain that there is a continuous layer of Ir ($t_{\mathrm{Ir}} > 0.5$ nm). On the other hand, when Ir is thin, it might not form a continuous layer in which case the ferromagnet underneath will face Ta in some regions. This will result in local modification of the interface between cobalt and the top capping layer and the

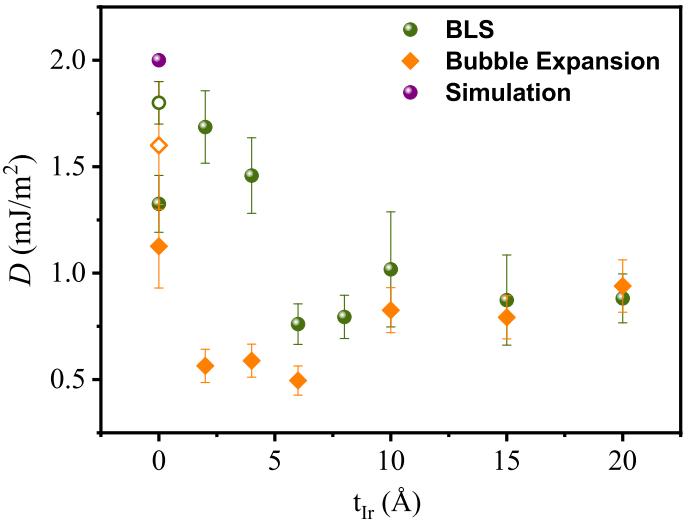

Figure 5.21: Comparison between DMI factors estimated from frequency shift in BLS spectrum and minimum of velocity in bubble expansion. For $t_{\mathrm{Ir}} = 0$ the open shapes show the D value for BLS and bubble expansion when the M_{S} is substitute with the average value of other samples (*i. e.* excluding the DL effect)

average D of the sample (other related parameters as well) will change accordingly. Unfortunately, TEM cross section images could not achieve a high enough contrast to exactly distinguish a very thin Ir layer from Ta on the interface and we were not able to discuss the matter in a more quantitative way. But, checking the continuity of the crystal structure on top of cobalt layer in samples with 0.4 nm and 1.0 nm of Ir, one could see for the latter almost everywhere this crystalline structure grows to the top layer, whereas in the former case, there are rare cases of this observation. Also, as figure 5.22 shows wherever this happens the crystal structure is much thicker than the expected 0.4 nm. Knowing that Ta grow amorphously on top of Co and Ir, this effect can be related to island growth for thin Ir layers supporting the mention assumption.

Alternatively, this could be checked by investigating asymmetric bubble expansion for different nucleation points in the multilayers with thin Ir. It should be noted that D values for thicker Ir are almost the same between two techniques despite all the anomalies in asymmetric bubble expansion. Second, theoretical first principles calculations showed that DMI takes 80 % of its contribution from the first two monolayers of the HM layer [34], which agrees with observed trend here that above $t_{\mathrm{Ir}} = 0.5$ nm

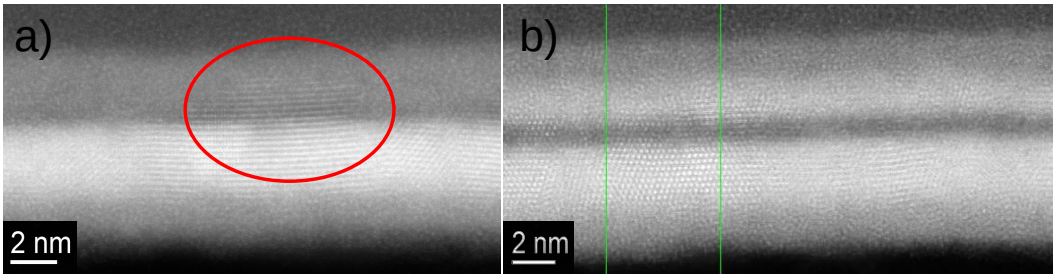

Figure 5.22: Cross-sectional HAADF images of multilayers with a) 0.4 nm and b) 1.0 nm of Ir. In the case of 0.4 nm Ir there is only one position that the crystalline structure of Pt\Co continues in the top layer, where for the 1.0 nm of Ir this effect is global (neglecting the contrast difference for Ir and Ta in this case). This fact supports the idea of island growth of iridium for thin Ir layers.

(about two monolayers of Ir in (111) direction) the DMI constant does not vary notably. Anyhow, the saturation of DMI for a specific thickness of the HM layer was mentioned in other literature as well. Robinson *et al.* [127] results show saturation of DMI after about 0.4 nm of HM layer for Pt\Co\Ir(0-2.5 nm)\Pt multilayers, which is equivalent to what we stated here. Thickness-dependent DMI was also observed in a Ta\CoFeB\Pt(wedge:0-0.3nm)\MgO\Ta (with no saturation in their thickness range) [194] and in SiO_2\CoFeB\Pt(0-6nm)\Cu structures, for which DMI reached a plateau after about 2 nm of Pt [195]. This dependence/independence of properties on Ir thickness was also seen for material-dependent parameters estimated from universal behaviour of domain wall motion (for present films). T_d, v_T, H_d along with the DW mobility are all depicted in figure 5.11 and table 5.1 for different t_Ir. It was mentioned that for films with $t_\mathrm{Ir} < 0.5$ nm the parameters fluctuate, but additional Ir thickness seems not to change the domain wall dynamics considerably.

In addition, D values extracted from both techniques suggest that Ir reduces total DMI of the stacks, meaning its DMI constant has the same sign as Pt. Changing of DMI sign and strength has been confirmed with experiments when scanning the $5d$ transition metals [30, 42, 196]. In the case of Ir, however, the situation has been more complicated. The opposite DMI sign of Pt and Ir was expected from theoretical calculations [29, 31, 197] and reported in various experimental studies [12, 42, 196, 198, 199], but this was put under dispute when Kim *et al.* measured same sign of DMI for Ir\Co\$AlO_x$ and Pt\Co\$AlO_x$ trilayers [186]. Ajejas *et al.* [129] have observed decline

of DMI when exchanged Ir for Al in Pt\Co\Al\Pt. Recently, Ma *et al.* [196] also detailed that DMI of their Ir\Co\MgO\Ta and Pt\Co\MgO\Ta have the same sign but different strength. Just to add to the already present strange behaviour of Ir-FM DMI, it was shown that the DMI of Ir also changes sign depending on the adjacent FM layer. *Ab initio* calculations revealed that the sign of D is positive (right-handed chirality) for Ir\Fe, and negative (left-handed chirality) for Ir\Co and is positive again for Ir\Ni [34]. Experimental studies on different $5d$ elements also reported that D_{Ir} is changing sign with exchange of FM layer from CoFeB to Co [196]. Considering all these contradictory results about the sign of the DMI in Ir including interfaces, one will wonder about the physical reason for it. Although, to the best of my knowledge there is still no definite answer for this but there can be some hypotheses. DMI is demonstrated to be dependent on the filling of the $5d$ states. It is changing sign for Ta and W with less than half filled $5d$ states and Pt and Au with more than half filled states [196]. It is also very sensitive to hybridisation of $3d$ orbitals of FM with $5d$ orbitals of HM material, in addition to aligning of Fermi energies in mentioned atomic states [29, 34]. As a result slight changes of the Fermi energy in either of FM or HM will affect DMI. The situation is more critical for Ir as it sits close to the sign reversal of DMI having 7 electrons in the $5d$. Moreover, in polycrystalline samples such as the ones here, interdiffusion of the atoms in the interface is almost unavoidable, as a result it may cause changes of Fermi energy alignment for the atoms at the interface. These are the very atoms that are important in the generation of the DMI.

5.10 Conclusion

In this chapter, the domain wall dynamics and Dzyaloshinskii-Moriya interaction in polycrystalline SiO_2\Ta\Pt\Co\Ir(t_{Ir})\Ta multilayers have been investigated. The presence of the β-phase of Ta seed layer was proved by investigating the X-ray diffraction spectra. Perpendicular magnetic anisotropy was observed for all multilayers which is expected to originate from the Pt-Co interface. Magnetic characterization showed almost the same saturation magnetization and effective anisotropy for all of the samples, except when $t_{\mathrm{Ir}} = 0$. The lower M_{S} of the Pt\Co\Ta sample was attributed to the well-known dead-layer at the interface of Co with Ta. Symmetrical propagation of DW using OoP driving field was also studied. The data were shown to have good agreent with universal creep and depinning formulations. The experimental results

on asymmetrical bubble expansion did not have the form expected from the simple creep model of Je et al. [109], along with other researchers work [35, 38, 41, 129]. We showed that getting H_{DMI} from the velocity minimum in asymmetrical bubble expansion might lead to significant DMI underestimation. Assuming that depinning field, H_{d} also changes with the applied H_{InP} – just like DW's energy density–, using micromagnetic simulations the H_{d} variations came out to be asymmetric. This asymmetry was mirrored in changes of v as a function of H_{InP} and resulted in better prediction of experimental data. Comparing the D from different measurements, generally BLS delivers a higher value. This can be understood if considering BLS measurement as an average from the whole film, while domain wall expansion is focusing on local changes. The change of depinning related parameters and DMI strength for thin and thick Ir layers happen to be different. While for $t_{\mathrm{Ir}} < 0.5$ nm the mentioned parameters was changing without a particular trend, films with $t_{\mathrm{Ir}} > 0.5$ nm showed almost similar values of each parameters for higher Ir thicknesses. This variation of parameters for thinner Ir was argued to be as a result of island growth of dusting Ir, and inability to form a continuous layer. Finally, some discussions about contradictory results on the sign and strength of DMI in Ir interfaces was also made.

Chapter 6

Polycrystalline Multilayers of Pt\Co\Hf(t_{Hf})\Ta

6.1 Introduction

Following the arguments in the introduction of previous chapter, here again the aim is to gain a higher effective DMI in trilayers, using additive effects from two materials with opposite DMI, when they are placed at either side of the ferromagnet. Pt is a usual material to use for its high spin-orbit coupling, which leads to high spin-Hall angle [14] and large DMI strength [29, 107]. Peculiarly, Hf, being a $5d$ heavy-metal, is not a well-studied material for DMI, and to the best of my knowledge, there are only two reports on its DMI. Still, those articles are contradicting in both sign and strength of Hf's resulting DMI when facing CoFeB [30, 35]. In this chapter we firstly study the magnetic properties of Pt\Co\Ta multilayers. Then depositing Hf on the top of Co layer, we will investigate Pt\Co\Hf\Ta multilayers magnetic properties and measure the effective DMI of the whole stack, as a function of Hf thickness.

6.2 Samples

Polycrystalline multilayers of Pt\Co\Hf(t_{Hf})\Ta were deposited using multi-target-module (MTM) of the TIMARIS deposition system [200], as a part of secondment that I had to Singulus Technologies. Base pressure of the system was better than 7×10^{-9} Torr. The deposition power for Ta, Pt, Co, and Hf were 0.5 kW, 0.1 kW, 0.3 kW, and 0.1 kW, respectively. Ar partial pressure during sputtering was 300 sccm (unless stated otherwise). To calibrate the deposition rate a rather thick film (about 200 nm) was deposited on the SiO_2 and then the film thickness was measured using an alpha-step. Thermally oxidised silicon wafer substrates were Ar etched for 60 s using 180 sccm pressure and power of 200 W. Then the multilayers were deposited. The same multilayer structures were deposited several times on one substrate as a pre-sputtering process.

6.3 Magnetic Characterization

Firstly, samples of etched-SiO_2\Ta(2)\Pt(2)\Co(t_{Co})\Ta(4) were grown to get the best thickness for Co. The Co thicknesses are t_{Co} =0.8, 1.0, 1.2, and 1.4 nm. The hysteresis loops of the samples were measured using VSM, for which the moments were calibrated with a 1×1 cm^2 Ni sample (The same size as the measured samples). All the samples

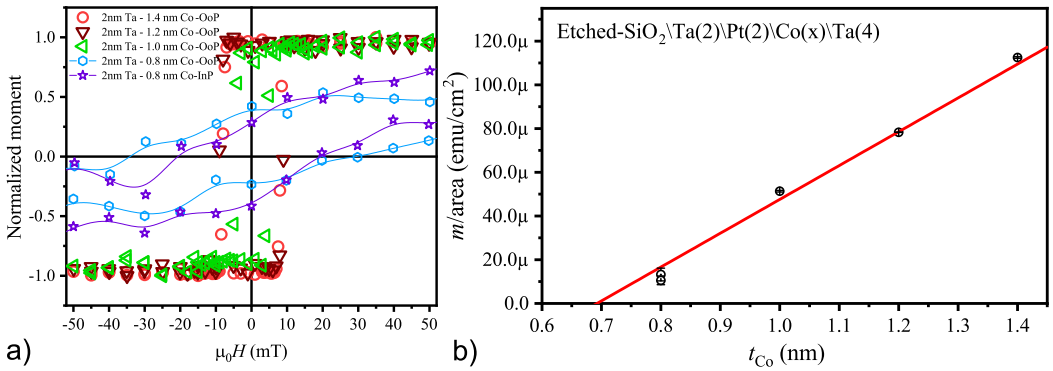

Figure 6.1: a) The hysteresis loop of etched-SiO_2\Ta(2)\Pt(2)\Co(t_{Co})\Ta(4) multilayers with different Co thicknesses. The data also shows that multilayer with 0.8 nm of Co does not have PMA anymore. b) The change of moment per area for different multilayers. The solid line shows the linear fitting to get the dead-layer. The insets show areal moment vs. Hf thickness.

except for 0.8 nm Co exhibit PMA, as is depicted in figure 6.1.a. The 1.0 nm thickness was decided to be the desired thickness, as it shows both PMA and has the lowest coercive field, H_c, at the same time.

The changes in moment per area for multilayers with Co thickness is illustrated in figure 6.1.b. Fitting the values with a line, it shows that the deposited cobalt reaches zero moment at 0.69±0.04 nm implying that this portion of the ferromagnetic layer does not exhibit magnetic properties. This is known as a dead-layer, and usually arises from interdiffusion of the materials at the interface [177–179, 181]. This effect is specially known for ferromagnetic layers meeting tantalum [172, 175, 177, 180–182] (refer to section 5.3 for more details). It also explains the magnetic loops of the specimen with nominally 0.8 nm of Co not having an easy plane, where DL would probably just leave $\sim$ 0.1 nm of active magnetic material in the stack.

To check if the Hf helps with the dead layer Ta(2)\Pt(2)\Co(0.8)\Hf(t_{Hf})\Ta(4) were deposited on etched-SiO_2 substrates. The thicknesses used for dusted Hf layers were t_{Hf} =0.2, 0.4, 0.6, 1 and 2 nm. The magnetic behaviour of the samples was investigated by VSM in both InP and OoP configuration. The results in figure 6.2 suggests that Hf slightly reduces the magnetic DL in the multilayers, as it measures a much better signal. It also can be seen that this series of multilayers **still** do not show a strong preferred anisotropy between InP and OoP directions. The presence of such a

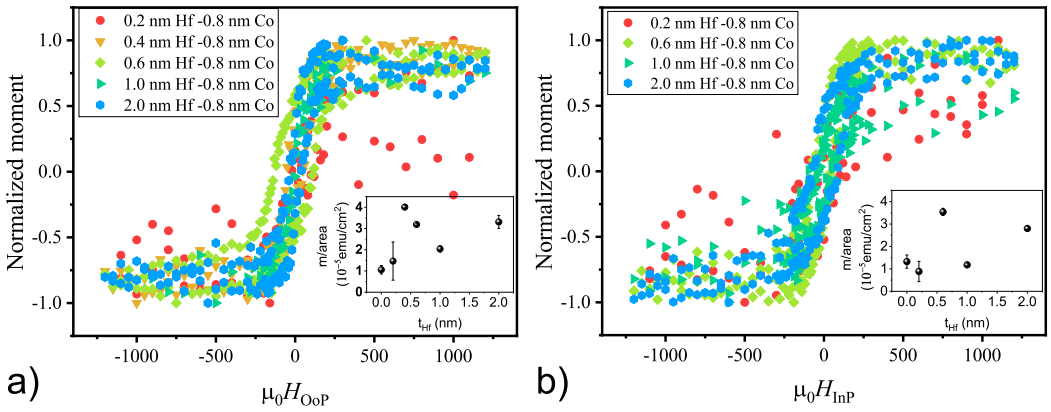

Figure 6.2: a) The hysteresis loop of etched-SiO_2\Ta(2)\Pt(2)\Co(0.8)\Hf(t_{Hf})\Ta(4) multilayers with different Hf thicknesses for a) OoP, and b) InP applied field. The insets are showing the change of areal magnetization with t_{Hf}.

dead layer, thus the discontinuity of cobalt might prevent PMA to dominate, as usually a 0.5 nm cobalt facing Pt is expected to rotate the anisotropy to the normal direction [201]. It is also known that cobalt deposited on the top of Pt exhibits PMA usually when cobalt is more than 2 monolayers [202]. This suggests that even a thick Hf layer could not completely eliminate the development of the DL in the ferromagnetic layer of cobalt.

The next set of samples were etched-SiO_2\Ta(2)\Pt(2)\Co(1)\Hf(t_{Hf})\Ta(4). The Hf thicknesses are t_{Hf} =0.2, 0.4, 0.6, 1 and 2 nm. Figure 6.3.a shows the OoP magnetic loops of the multilayers measured by VSM, which indicates the full squareness of the OoP hysteresis loops. The loops were used to get the saturation magnetization M_S. The anisotropy field, H_K, of the samples were also measured with in-plane saturated film using SQUID-VSM. Figure 6.3.b-c shows that coercive and anisotropy fields of different films does not change significantly, except for the case of H_c in the stack with 0.2 nm of Hf. This different behaviour of 0.2 nm dusted samples was previously mentioned for Ta\Pt\Co\Ir\Ta multilayers in chapter 5), which was attributed to complications coming from not making a continuous layer with 0.2 nm dusting material. The anisotropy fields are measured with in-plane saturated film using SQUID-VSM. The average of the anisotropy field for all stacks is $\mu_0 H_K = 0.95 \pm 0.01$ T.

As stated above, data are suggesting that there is still a dead-layer for Hf included films. Moments of films with different Hf thicknesses were considered to check the

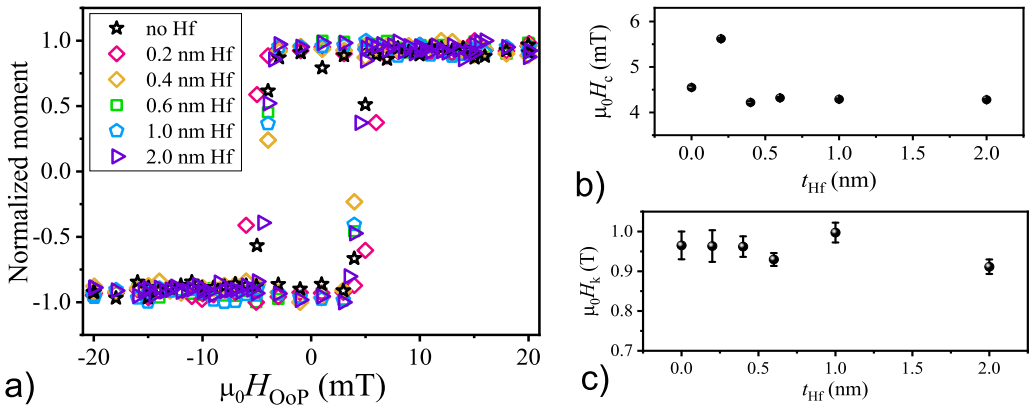

Figure 6.3: a) The hysteresis loop of etched-SiO_2\Ta(2)\Pt(2)\Co(1)\Hf(t_{Hf})\Ta(4) multilayers with different Co thicknesses. The change of b) coercive field, $\mu_0 H_c$, and c) anisotropy field, $\mu_0 H_K$, for different multilayers.

change of areal moment vs. t_{FM}. Also, films with less than 0.4 nm of Hf were excluded to avoid complications of having Co facing two materials (Hf and Ta) at the interface. The results in figure 6.4.a suggest a DL of 0.63±0.04 nm. This value is slightly less than DL for first set of films (for which Co makes an interface with Ta), but still in the error margin. This DL, along with the hysteresis loops shown in figures 6.2 and 6.3.a shows that introducing Hf does not really change the magnetic properties of the samples and any change made is less than 0.2 nm difference of Co thickness between the samples. Black points in figure 6.4.b represent calculated M_S with the nominal thickness of the Co (*i.e.* 1 nm), and red points are the same parameter when DL is subtracted from the Co thickness. It can be seen than the value of M_S massively changes when DL is considered and is closer to other values reported in literature [135, 177, 186]. There are not many measurements on magnetic properties of Hf included multilayers, but it is mentioned that Hf induces a higher PMA, usually in samples with CoFeB [203, 204] (supposedly as it can be a good boron sink [205, 206]). Reportedly, there was no magnetic dead layer present in Hf\CoFeB\MgO trilayers [204, 206]. Nevertheless, it should be kept in mind that a dead-layer is usually as a result of intermixing of the materials at the interface and its creation can be process, as well as material dependent [203]. Also, the high lattice mismatch between Co and Hf ($\sim 27\%$) can play an important role in inducing a dead layer.

It is worth to mention that M_S of the present films partly comes from the proximity

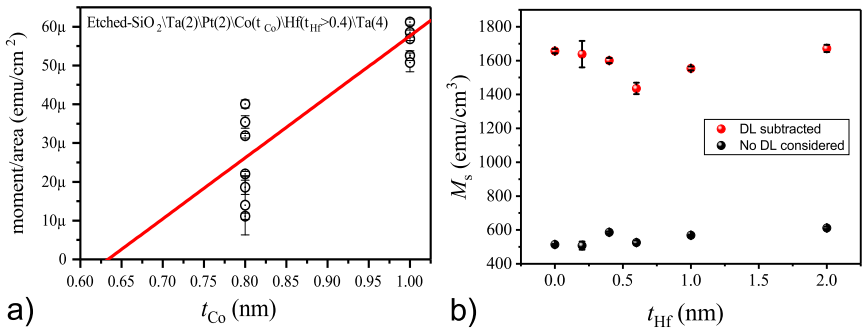

Figure 6.4: a) The hysteresis loop of etched-SiO_2\Ta(2)\Pt(2)\Co(1)\Hf(t_{Hf})\Ta(4) multilayers with different Co thicknesses. b) The change of coercive field, $\mu_0 H_c$, for different multilayers.

induced magnetism in Pt layer [149, 207, 208], which is not accounted for in this calculatins. Consequently, the M_S is larger than the saturation magnetization of bulk Co which is ~ 1440 emu/cm^3. These M_S (with DL deducted) values are used for future calculations which are dependent on M_S.

Also, using the variation of saturated magnetization as a function of temperature for the range of 20-350 K, the data were fitted by Bloch law and the exchange stiffness, A, of the multilayers were calculated. Details of the calculation is described in section 3.3.2. Using the M_S, H_K, and A other magnetic related parameters, such as DW width, Δ, anisotropy energy, $K_{eff} = \mu_0 H_K M_S/2$ and demagnetizing energy density, $K_D = \mu_0 M_S^2/2$ were calculated. Further characterization was solely done on this set of samples, for which all the magnetic parameters are detailed in table 6.1.

6.4 Effective Dzyaloshinskii-Moriya Interaction

To identify the strength of DMI in the multilayers we used both asymmetrical bubble expansion and BLS techniques. The details of the measurement and analysis for the asymmetrical bubble expansion are explained in 3.4.1 and 2.5.2, respectively. As the coercive fields of all the films are small and similar in value (*c.f.* table 6.1), the OoP field of 3 mT was used to propagate the bubble domains, except for the film with 0.6 nm of Hf for which $\mu_0 H_{OoP} = 2$ mT was used to grow the bubble domains. When the static InP field is present, it affects the DW surrounding the bubble and breaks the symmetry of the propagation. Figures 6.5.m-r and 6.5.s-x illustrate this symmetric and

Table 6.1: Magnetic parameters of polycrystalline Pt\Co(1)\Hf\Ta for different Hf thicknesses t_{Hf}. Parameters are coercive field $\mu_0 H_{\mathrm{c}}$, anisotropy field $\mu_0 H_{\mathrm{K}}$, saturation magnetization M_{S}, effective anisotropy K_{eff}, demagnetizing energy density K_{D}, DW width Δ, and ground state Bloch wall energy, σ_0. The mentioned errors are the largest error between different values.

t_{Hf}	$\mu_0 H_{\mathrm{c}}$	$\mu_0 H_{\mathrm{K}}$	M_{S}	A	K_{eff}	K_{D}	Δ	σ_0
nm	mT	T	MA/m	pJ/m	MJ/m^3	MJ/m^3	nm	mJ/m^2
-	±0.1	±0.03	±0.03	±0.3	±0.02	±0.2	±0.1	±0.2
0.0	4.6	0.97	1.66	12.8	0.80	1.7	4.0	12.8
0.2	5.6	0.96	1.64	16.4	0.79	1.7	4.6	14.4
0.4	4.2	0.96	1.60	15.4	0.76	1.6	4.5	13.8
0.6	4.3	0.93	1.44	13.2	0.67	1.3	4.4	11.9
1.0	4.3	1.00	1.55	14.8	0.77	1.5	4.4	13.5
2.0	4.3	0.91	1.67	10.5	0.76	1.8	3.7	11.3

asymmetric growth of bubble domain when $\mu_0 H_{\mathrm{InP}} = 0$ mT, and $\mu_o H_{\mathrm{InP}} = -100$ mT, respectively. Knowing that the magnetization of the black domains (images 6.5.s-u and w) faces the reader and the $\mu_0 H_{\mathrm{InP}} = -100$ mT is towards the left, it is clear that the DWs have left-handed chirality (*c.f.* section 3.4.2).

The measured velocities for each InP applied fields were averaged between 3 measurements with different propagation timing, to smear out the probable effects of local changes in different parameters. The results are illustrated in figure 6.5.a-f. Fields up to 280 mT were applied with the available electromagnet. It is worth to mention that in high InP fields, the domain propagation is very fast and in some cases the DW displacement cannot be measured with the shortest pulse available. Also, there can be several domains nucleated in the field of view, and they will merge together, although, extreme care was taken to have just one single nucleation point in the field of view to avoid this as much as possible. As a result, limitations were applied to the highest InP field for which the DW velocities could be measured. Thus, measured velocity curves does not continue on both sides of the minimum point (for a particular DW) and one arm of each single curve could not be sampled. This is more clear in changes of $\ln(v_{\mathrm{DW}})$ with H_{InP} in figure 6.5.g-l, where the minimum of the curve, H_{offset} can be hardly seen

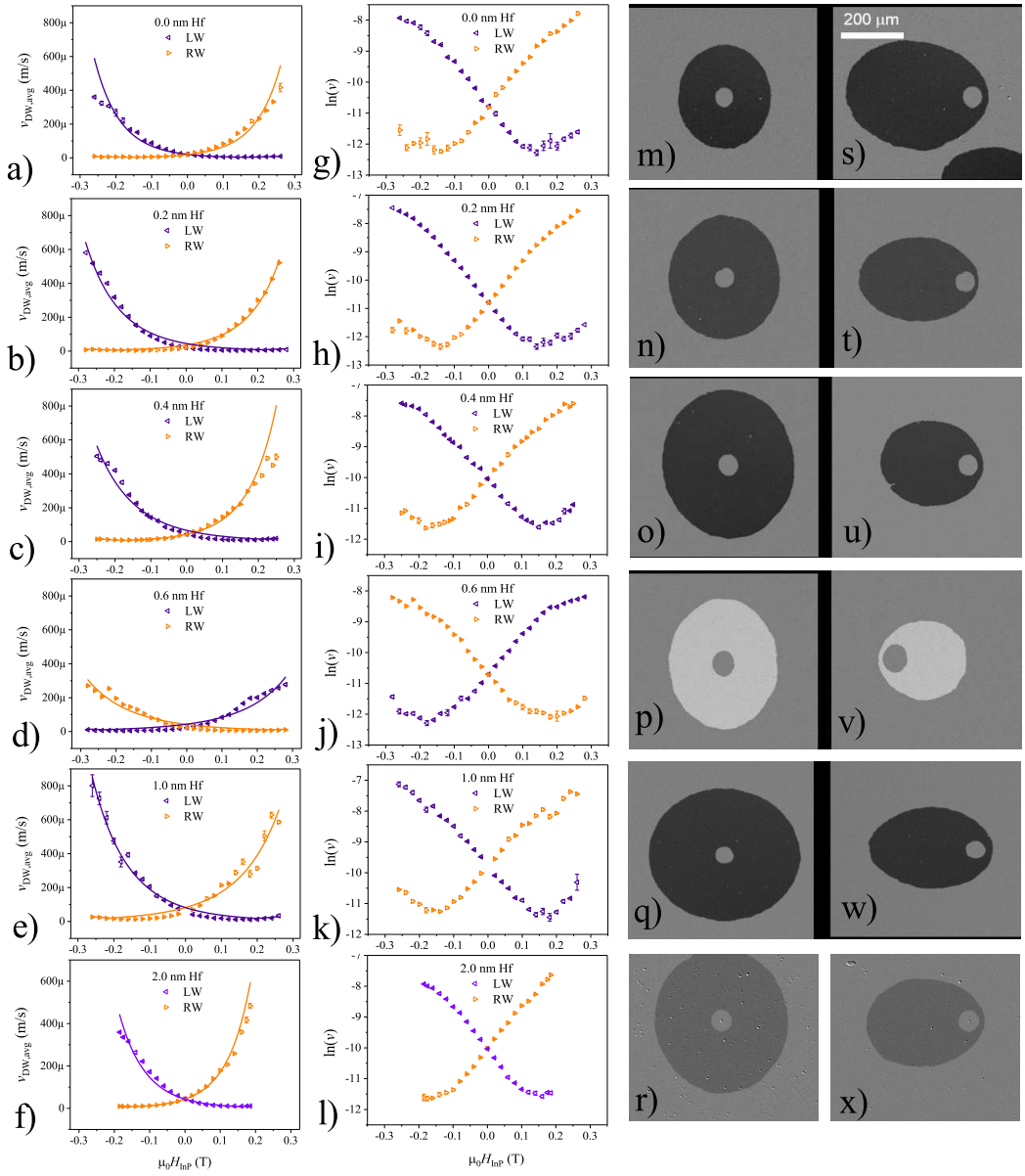

Figure 6.5: Asymmetrical bubble expansion in etched-SiO_2\Ta\Pt\Co(1)\Hf(t_{Hf})\Ta multilayers with different t_{Hf}. a-f) Changes of DW velocity vs. InP applied field along with the fitting to the creep theory affiliated to Je *et al.* [109]. g-l) Natural logarithmic changes of velocity for the same multilayers. Data for the DW on the right (left) side of the bubble are shown by right (left) faced orange (purple) triangles. Growth of bubble domain with: m-r) $\mu_0 H_{InP} = 0$ mT and, s-x) $\mu_0 H_{InP} = -100$ mT for different films. Pulse times are not necessary the same for all images.

for some samples.

Nevertheless, the anomalies seen for polycrystalline Pt\Co\Ir\Ta multilayers –which were described in detail in previous chapter– are not present here, and the velocity curves are symmetrical for opposite facing walls (LW and RW). Consequently, equations 2.18 and 2.19 were used to fit the data with creep theory. The final equation will be:

$$v_{\mathrm{DW}} = v_0 \exp\left(-\zeta(\mu_0 H_{\mathrm{OoP}})^{-1/4}\left(\frac{\sigma_0 + 2K_{\mathrm{D}}\Delta - \pi\Delta M_{\mathrm{S}}|\mu_0 H_{\mathrm{InP}} + \mu_0 H_{\mathrm{DMI}}|}{\sigma_0 + 2K_{\mathrm{D}}\Delta - \pi\Delta M_{\mathrm{S}}|\mu_0 H_{\mathrm{DMI}}|}\right)^{1/4}\right) \tag{6.1}$$

where v_0 is the velocity prefactor, ζ another prefactor that is considered constant in this model, $\mu_0 H_{\mathrm{OoP}}$ the driving OoP field, K_{D} demagnetizing energy density, σ_0 energy density of Bloch DW in the ground state, Δ DW width, M_{S} saturation magnetization, $\mu_0 H_{\mathrm{InP}}$ in-plane applied field and $\mu_0 H_{\mathrm{DMI}}$ the DMI field. Results of magnetic measurement were used to calculate values of K_{D}, Δ, and σ_0 (detailed in table 6.1) for fitting. Deriving the H_{DMI} from the fit then, DMI strength would be $D = \mu_0 H_{\mathrm{DMI}} M_{\mathrm{S}} \Delta$.

In addition to asymmetric bubble expansion, the same films were examined with BLS (by Hans Nembach) to evaluate DMI. As it was stated in detail in section 2.5.3, when DMI is present in the sample it causes a nonreciprocal propagations for the spin-waves which are propagated perpendicular to the magnetization direction. The Damon-Eshbach geometry with an incident wave-vector of $k_{\mathrm{SW}} = 16.7\ \mu\mathrm{m}^{-1}$ was used. In this geometry the sample is saturated in-plane and the propagation of the spin-waves in perpendicular direction to the applied field is measured using backscattering of a laser with $\lambda = 532$ nm (more details in 2.5.3).

Figure 6.6 presents the results from BLS measurements for multilayers with different t_{Hf}, along with the frequency shift, Δf. It can be seen that Δf is increasing as soon as there is Hf in the stack, which suggests the increase of the effective DMI in the films. I also argue that the non-reciprocity in the spin-waves is not due to surface anisotropy, as this effect is negligible for ultra-thin ferromagnetic layers [187]. The fact that the shifts of the Stokes and anti-Stokes peaks do not have the same sign when the film is saturated in opposite directions, helps us to exclude any contribution from dipolar effects, as well[105].

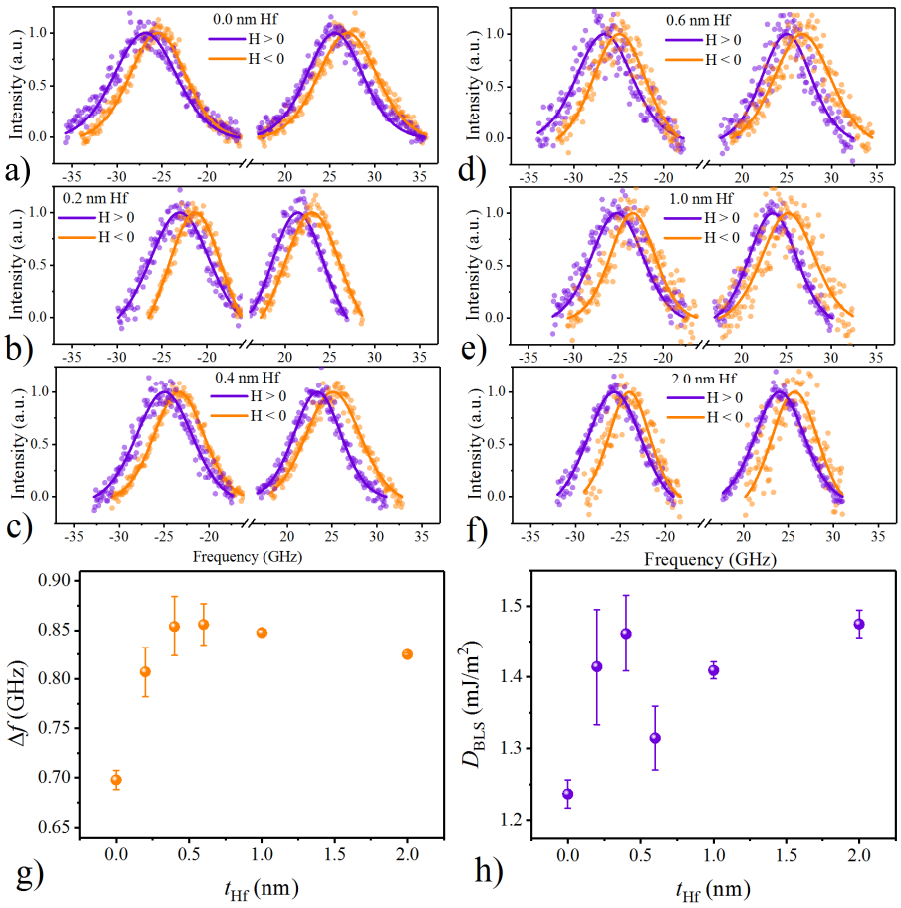

Figure 6.6: BLS meaurements for etched-SiO_2\Ta\Pt\Co(1)\Hf(t_{Hf})\Ta multilayers with different Hf thicknesses, calculated using a-f) The Stokes and anti-Stokes peaks for opposite directions of saturated magnetization (in red and black circles) along with the Lorentzian fits to the data (black and red solid lines). The changes of g) frequency shift Δ_f and h) DMI strength D, with t_{Hf}.

6.5 Discussion

The fitting to asymmetrical bubble expansion DW velocities have a good agreement with the data as they are shown by solid lines in figure 6.5.a-f. On the other hand, –as it is expected– the limitations of not being able to measure far from the minimum point in v curves, leads to high error bar in the derived D, as it can be seen in figure 6.7.a. To compare the results with the fitting values, we used the same procedure as in previous chapter, and assumed that the minimum of the velocity curves is the

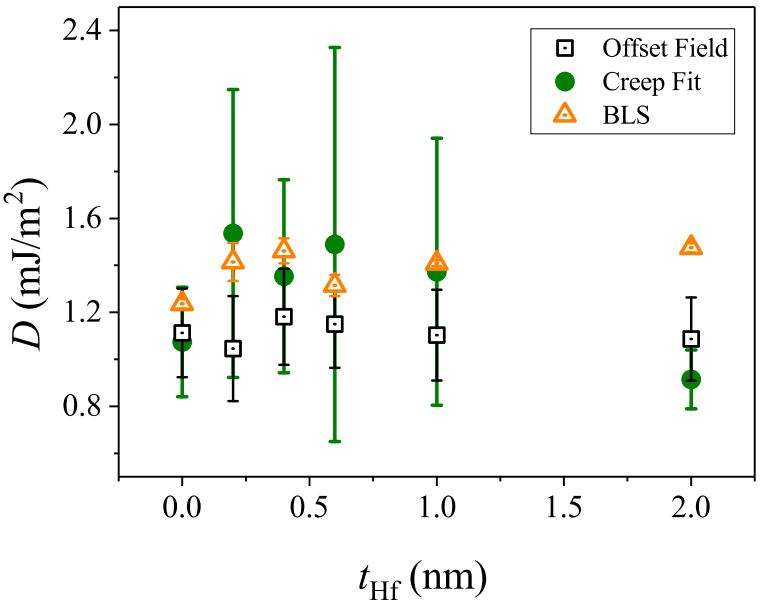

Figure 6.7: DMI strength for etched-SiO_2\Ta\Pt\Co(1)\Hf(t_{Hf})\Ta multilayers with different Hf thicknesses, calculated using asymmetric bubble expansion, and BLS measurement.

$\mu_0 H_{offset} = -\mu_0 H_{DMI}$, which also can be an evaluation of the DMI strength D. As it can be seen in figure 6.7.a the D strength estimated from the $\mu_0 H_{offset}$ (Black squares) is generally lower that the fitted D (Green solid circles), but still within the error bar.

When there is no InP field present, sample images of the bubbles show that bubbles are always elongated in one direction (figure 6.5.m-r). This elongation of bubble domain was previously reported [35] and suggest an InP uniaxial anisotropy in the samples. It also means that the DW velocities will be higher if the InP field is aligned with the elongation axis of the bubble. So, the anisotropy field of the etched-SiO_2\Ta\Pt\Co(1)\Hf(1.0)\Ta was measured in both directions parallel and perpendicular to the elongation axis. The respective values are $\mu_0 H_{K,\parallel} = 900 \pm 10$ mT and $\mu_0 H_{K,\perp} = 950 \pm 10$ mT. To check how it affects the fitting, thus evaluated D, these values were substituted in the fitting equation 6.1, and resulted in $D_{1.0Hf,\parallel} = 1.5 \pm 0.6$ mJ/m^2 $D_{1.0Hf,\perp} = 1.4 \pm 0.6$ mJ/m^2. It can be seen that this does not affect the final values significantly, as both results are very close and within error bars. This can be seen in figure 6.5.e and q, for the case of the multilayer with 1.0 nm of Hf where velocities are reaching 800 μm/s for $\mu_0 H_{InP} = 280$ mT. The fact that in such

multilayers velocity in one direction is twice as much without notable change in DMI can be interesting for technological applications.

As for the BLS results, for all samples we found that Stokes peak are higher than the anti-Stokes frequencies for the samples that are saturated with the positive InP field. This indicates left-handed chirality (negative sign of D), which is in accordance with the results from asymmetrical bubble expansion.

The resulting DMI constant from asymmetrical bubble expansion, D_{BE}, indicated the increase of effective DMI when the Hf is placed between the Co and Ta. The values evaluated with BLS, D_{BLS}, are also suggesting the same fact. As the DMI of Ta is expected to be negligible [30], this rising of D suggests that the DMI sign of Hf and Pt are opposite, thus show an additive behaviour when placed in opposite sides of the ferromagnetic layer. This is in agreement with measurements of Soucaille *i.e.* [35], in which they found right-handed chirality for Hf\CoFeB\MgO, and in contrast to left-handed chirality of the same structures by Torrejon *et al.* studied using current induced DW motion [30]. This can be as a result of complexity of effecting parameters when CoFeB is used as the ferromagnetic layer, which can include level of crystallinity [209, 210], annealing temperature [39], boron diffusion [128, 206], *etc.* For example, it was previously mentioned that Ir exhibits opposite chirality depending on the FM layer that it makes interface with [34]. The same might be valid here, especially considering that the combination of the used CoFeB is usually missing in the literature.

Comparing the resulting D values from both techniques, figure 6.7 again emphasises on the fact that DMI strength estimated from H_{offset} will lead to underestimation. A closer approximate to D_{BLS} is derived from the fitting of DW velocity curves, but it still shows a large error (due to the mentioned limitations in measurement). It should be kept in mind that fitting the velocity curves in this way is only reasonable in the case of symmetrical curves with no anomalies (a thorough discussion on the model limitations can be found in section 5.9).

6.6 Conclusion

We performed a detailed study of the magnetic properties of Pt\Co(t_{Co})\Hf(t_{Hf})\Ta multilayers with $t_{\mathrm{Co}} = 0.8$ and 1.0 nm and $t_{\mathrm{Hf}} = 0.0 - 2.0$ nm. The VSM data showed partial PMA for $t_{\mathrm{Co}} = 0.8$ nm when $t_{\mathrm{Hf}} \neq 0$. The anisotropy easy axis of the multilayers rotates towards the OoP direction when (nominally) 1 nm of Co is deposited. Having

areal moment for films with different Co thickness, the thickness of the dead-layer in the samples was evaluated and deducted to get the active magnetic material. Asymmetrical bubble expansion and BLS measurements were used to evaluate the strength of DMI. Both techniques proved the left-handed chirality of the DWs, in contrast to previous measurement [30]. They also showed that inserting Hf in between the Co and Ta in Pt\Co\Ta multilayer leads to increase of D suggesting that DMI sign of Hf-Co interface is opposite to Pt-Co. In addition, changing the Hf thickness did not result in significant changes of DMI. The results here also confirmed our previous speculation that in bubble expansion measurements, taking the field at which the velocity minima happens as the H_{DMI}, is too much simplification and leads to underestimation of D. We suggest that even under the circumstance of well-behaved velocity curves, only the full fit of the curve considering all magnetic parameters might give us a good estimation of DMI strength.

Chapter 7

Conclusion and Outlook

7.1 Summary

This thesis has explored a full study of domain wall dynamics for epitaxial and polycrystalline multilayers. As these structures can be applied in new spintronic based devices, the need for understanding how to control different effects and the best way to estimate their strength is of importance. So firstly, an introduction to the context of the work was given, and some required background was explained. The experimental results followed the description of preparation and techniques. The results were separated based on the structure.

The epitaxial films of Pt\Co\Au_xPt_{1-x} were grown (x = 0, 0.5, 1) using high-temperature sputtering deposition. Using increasing contribution of Au in the top layer, the inversion symmetry of the system was increased in a controlled way. This systematical change of material symmetry enabled us to study the changes of magnetic properties, DW motion regimes, DMI, and SHE. The films texture was proved to be epitaxial using XRD and cross sectional electron microscopy with bright atomic fringes. The crystalline ordering of the films helped us to avoid ambiguities coming from uncontrollable quality of sputtered materials and interfaces, also to get a fully symmetrical multilayer with zero effective DMI and SHE. This is not easy to get as there were many polycrystalline Pt\Co\Pt trilayers that exhibit non-zero values for these effects [12, 40, 41]. Increasing concentration of Au in the top layer not only enhances PMA, but also intensifies the depinning field and temperature. This means a higher pinning in the film and can be described by the sharper interface that gold makes with Co, due to low proximity induced magnetization [34, 134] and not having the tendency to alloy with Co [147, 148]. A full micromagnetic model of the DW motion reproduced the experimental results with a very good agreement, and it was shown that 1D model is not very reliable. Universal fitting of creep and depinning field-induced DW motion has resulted in high estimations of damping, especially in the case of Pt\Co\Au where damping parameters were large. It was argued that this might be due to other dissipation mechanism during DW motion that are not usually included in other ways to measure damping.

To enhance the previously proven high DMI in Pt\Co\Ta films [170], Ir layers with different thicknesses was added to the top interface. The PMA multilayers of Pt\Co\Ir(t_{Ir}) (t_{Ir} = 0-2.0 nm) had β-Ta as the top layer. Studying field-induced domain wall motion and applying universal creep and depinning formulations, the material

dependent parameters of pinning was concluded. Also, the DMI strength in different films was studied using asymmetrical bubble expansion and BLS. It was shown that depinning parameters and DMI in samples with more than two monolayers of Ir are almost similar, and argued that less Ir leads to disscontinuous layer and unpredictable characteristics. The evaluation of DMI using Je's creep model [109] was discussed in detail and explained that it is insufficient to explain the DW behaviour in the present stacks. In the mentioned model the effect of InP field was excluded to the domain wall energy density, but assuming that depinning field is also effected by applied InP field better agreement with results was achieved. This assumption also explained the divergence of DW velocities on each side of the bubble at high InP fields. The DMI sign of Ir was shown to be the same as Pt, which is in opposition with theoretical predictions [29, 31] and some measurements [12, 42, 196, 198, 199]. The was attributed to the high sensitivity of DMI to fine changes in the interface quality, which in turn can effect the level of $5d - 3d$ hybridization, and changes in Fermi energy at the FM-NM interface. The situation is more critical for Ir it is almost placed in the middle of heavy transition metals and its $5d$ orbital has only 7 electrons.

Polycrystalline multilayers of Pt\Co(t_{Co})\Hf(t_{Hf})\Ta (t_{Hf} = 0-2.0 nm) were deposited in a commercial sputtering system of Singulus technology. Multilayers with $t_{\mathrm{Co}} < 1.0$ nm did not show any preferred anisotropy. The investigation of moment vs. Co thickness resulted in DL of $\sim$ 0.7 nm. Films with 1 nm of cobalt were used for further investigation of DMI. Both asymmetrical bubble expansion and BLS proved left-handed chirality of the samples. It was seen that adding Hf causes DMI to rise, suggesting a positive sign of D. This is opposite to DMI of Pt, and objects with previously published results based on current-induced DW motion [30]. Moreover, changing the Hf thickness did not affect the net DMI significantly.

7.2 Future Work

As epitaxial trilayer systems were suggested to be model systems for investigation of magnetic multilayers with broken inversion symmetry, this study can be expanded to investigate DM effects for different elements and exclude interface quality impacts on DMI as much as possible. First principles calculations can be done in parallel based on the deposited system to examine the compatibility of the results with theory. The very first one to investigate is good to be Ir, considering all the contradictory results

that are found in the literature. Also, it was discussed that DWM usually gives a high limit for Gilbert damping, so this value can be measured with other techniques such as FMR to compare the results from domain wall motion (in systems with lower damping, where FMR signal is actually detectable). One of the ultimate applications for magnetic multilayers such as the ones in this study are in current-induced memories or processing devices, so these systems can be used to study current-induced DW motion and evaluate SOT related effects such as spin Hall angle and Rashba effect. One also could extend the investigation of thickness related DMI to other materials.

References

[1] *English Oxford living Dictionary*, Oxford University Press (2018)

[2] C. D. Cullity, B.D.; Graham, *Introduction to magnetic materials*, IEEE Press John Wiley & Sons, New Jrsey (2009)

[3] D. I. E., Theory of helicoidal structures in antiferromagnets, *Sov. Phys. JETP* **20**, 665 (1965)

[4] J. Sampaio, V. Cros, S. Rohart, A. Thiaville and A. Fert, Nucleation, stability and current-induced motion of isolated magnetic skyrmions in nanostructures, *Nature Nano.* **8**, 839 (2013)

[5] S. A. Wolf, Spintronics: A spin-based electronics vision for the future, *Science* **294**, 1488 (2001)

[6] D. A. Allwood, Magnetic domain-wall logic, *Science* **309**, 1688 (2005)

[7] S. S. P. Parkin, M. Hayashi and L. Thomas, Magnetic domain-wall racetrack memory, *Science* **320**, 190 (2008)

[8] Youtube - every second, Technical report, EverySecond (2018)

[9] A. Baxter, SSD vs HDD, *StorageReview.com*

[10] K.-S. Ryu, L. Thomas, S.-H. Yang and S. Parkin, Chiral spin torque at magnetic domain walls, *Nature Nano.* **8**, 527 (2013)

[11] A. Thiaville, S. Rohart, É. Jué, V. Cros and A. Fert, Dynamics of Dzyaloshinskii domain walls in ultrathin magnetic films, *EPL (Europhysics Letters)* **100**, 57002 (2012)

[12] A. Hrabec, N. Porter, A. Wells, M. Benitez, G. Burnell et al., Measuring and tailoring the Dzyaloshinskii-Moriya interaction in perpendicularly magnetized thin films, *Phys. Rev. B* **90**, 020402 (2014)

[13] A. V. Khvalkovskiy, V. Cros, D. Apalkov, V. Nikitin, M. Krounbi et al., Matching domain-wall configuration and spin-orbit torques for efficient domain-wall motion, *Phys. Rev. B* **87**, 020402 (2013)

[14] S. Woo, M. Mann, A. J. Tan, L. Caretta and G. S. Beach, Enhanced spin-orbit torques in Pt/Co/Ta heterostructures, *Appl. Phys. Lett.* **105**, 212404 (2014)

[15] H. Wang, C. Du, Y. Pu, R. Adur, P. Hammel et al., Scaling of spin Hall angle in 3d, 4d, and 5d metals from$Y_3Fe_5O_{12}$/metal spin pumping, *Phys. Rev. Lett.* **112** (2014)

[16] E. Martinez, S. Emori and G. S. D. Beach, Current-driven domain wall motion along high perpendicular anisotropy multilayers: The role of the Rashba field, the spin Hall effect, and the Dzyaloshinskii-Moriya interaction, *Appl. Phys. Lett.* **103**, 072406 (2013)

[17] L. Carroll, *Alice's Adventures in Wonderland and Through the Looking Glass*, Penguin UK (2012)

[18] U. Schäfer, J. Kiefl, W. Zhu, M. Kempf, M. Eggers et al., *Importance of Chirality to Flavor Compounds*, American Chemical Society, Washington, DC., chapter Authenticity Control of Food Flavorings - Merits and Limitations of Chiral Analysis, ACS Symposium Series (2015)

[19] P. Ball, A handle on handedness, *Nature* **News** (2000)

[20] M. Clemmit, Left-handed sugar gets a free ride out of your system, *The Scientist* **5** (1991)

[21] D. Wolman, *A Left Hand Turn Around the World: Chasing the Mystery and Meaning of All Things Southpaw*, Da Capo Press (2006)

[22] W. Thomson, *The molecular tactics of a crystal*, Oxford, Clarendon Press (1894)

[23] I. Dzyaloshinskii, Thermodynamic theory of weak ferromagnetism in antiferromagnetic substances, *Sov. Phys. JETP* **5**, 1259 (1957)

[24] T. Moriya, Anisotropic superexchange interaction and weak ferromagnetism, *Phys. Rev.* **120**, 91 (1960)

[25] A. Fert, *Materials Science Forum*, Transtech Publications, Aedermannsdorf, volume 59-60, p. 444 (1990)

[26] A. Crépieux and C. Lacroix, Dzyaloshinsky–Moriya interactions induced by symmetry breaking at a surface, *J. Magn. Magn. Mater.* **182**, 341 (1998)

[27] M. Bode, M. Heide, K. von Bergmann, P. Ferriani, S. Heinze et al., Chiral magnetic order at surfaces driven by inversion asymmetry, *Nature* **447**, 190 (2007)

[28] M. Heide, G. Bihlmayer and S. Blügel, Dzyaloshinskii-Moriya interaction accounting for the orientation of magnetic domains in ultrathin films: Fe/W(110), *Phys. Rev. B* **78** (2008)

[29] V. Kashid, T. Schena, B. Zimmermann, Y. Mokrousov, S. Blügel et al., Dzyaloshinskii-Moriya interaction and chiral magnetism in $3d-5d$ zigzag chains: Tight-binding model and ab initio calculations, *Phys. Rev. B* **90**, 054412 (2014)

[30] J. Torrejon, J. Kim, J. Sinha, S. Mitani, M. Hayashi et al., Interface control of the magnetic chirality in CoFeB/MgO heterostructures with heavy-metal underlayers, *Nature Commun.* **5**, 4655 (2014)

[31] H. Yang, A. Thiaville, S. Rohart, A. Fert and M. Chshiev, Anatomy of Dzyaloshinskii-Moriya interaction at Co/Pt interfaces, *Phys. Rev. Lett.* **115**, 267210 (2015)

[32] D.-Y. Kim, M.-H. Park, Y.-K. Park, J.-S. Kim, Y.-S. Nam et al., Chirality-induced antisymmetry in magnetic domain wall speed, *NPG Asia Materials* **10**, e464 (2018)

[33] H. Yang, O. Boulle, V. Cros, A. Fert and M. Chshiev, Controlling Dzyaloshinskii-Moriya interaction via chirality dependent atomic-layer stacking, insulator capping and electric field, *Sci. Rep.* **8**, 12356 (2018)

[34] A. Belabbes, G. Bihlmayer, F. Bechstedt, S. Blügel and A. Manchon, Hund's rule-driven Dzyaloshinskii-Moriya interaction at $3d-5d$ interfaces, *Phys. Rev. Lett.* **117**, 247202 (2016)

[35] R. Soucaille, M. Belmeguenai, J. Torrejon, J.-V. Kim, T. Devolder et al., Probing the Dzyaloshinskii-Moriya interaction in CoFeB ultrathin films using domain wall creep and Brillouin light spectroscopy, *Phys. Rev. B* **94**, 104431 (2016)

[36] M. Belmeguenai, M. S. Gabor, Y. Roussigné, A. Stashkevich, S. M. Chérif et al., Brillouin light scattering investigation of the thickness dependence of Dzyaloshinskii-Moriya interaction in $Co_0.5Fe_0.5$ ultrathin films, *Phys. Rev. B* **93** (2016)

[37] J. H. Franken, M. Herps, H. J. M. Swagten and B. Koopmans, Tunable chiral spin texture in magnetic domain-walls, *Sci. Rep.* **4**, 05248 (2014)

[38] M. Vaňatka, J.-C. Rojas-Sánchez, J. Vogel, M. Bonfim, M. Belmeguenai et al., Velocity asymmetry of Dzyaloshinskii domain walls in the creep and flow regimes, *J. Phys. Condens. Matter* **27**, 326002 (2015)

[39] R. A. Khan, P. M. Shepley, A. Hrabec, A. W. J. Wells, B. Ocker et al., Effect of annealing on the interfacial Dzyaloshinskii-Moriya interaction in Ta/CoFeB/MgO trilayers, *Appl. Phys. Lett.* **109**, 132404 (2016)

[40] A. W. J. Wells, P. M. Shepley, C. H. Marrows and T. A. Moore, Effect of interfacial intermixing on the Dzyaloshinskii-Moriya interaction in Pt/Co/Pt, *Phys. Rev. B* **95**, 054428 (2017)

[41] R. Lavrijsen, D. M. F. Hartmann, A. van den Brink, Y. Yin, B. Barcones et al., Asymmetric magnetic bubble expansion under in-plane field in Pt/Co/Pt: Effect of interface engineering, *Phys. Rev. B* **91**, 104414 (2015)

[42] K.-S. Ryu, S.-H. Yang, L. Thomas and S. S. Parkin, Chiral spin torque arising from proximity-induced magnetization, *Nature Commun.* **5**, 3910 (2014)

[43] K.-W. Moon, D.-H. Kim, S.-C. Yoo, S.-G. Je, B. S. Chun et al., Magnetic bubblecade memory based on chiral domain walls, *Sci. Rep.* **5**, 9166 (2015)

[44] D. Petit, P. R. Seem, M. Tillette, R. Mansell and R. P. Cowburn, Two-dimensional control of field-driven magnetic bubble movement using Dzyaloshinskii-Moriya interactions, *Appl. Phys. Lett.* **106**, 022402 (2015)

[45] A. N. Bogdanov and U. K. Rößler, Chiral symmetry breaking in magnetic thin films and multilayers, *Phys. Rev. Lett.* **87**, 037203 (2001)

[46] S. Emori, U. Bauer, S.-M. Ahn, E. Martinez and G. S. Beach, Current-driven dynamics of chiral ferromagnetic domain walls, *Nature Mater.* **12**, 611 (2013)

[47] S. Takahashi and S. Maekawa, Spin current, spin accumulation and spin hall effect, *Sci. Technol. Adv. Mater.* **9**, 014105 (2008)

[48] Y. A. Bychkov and É. I. Rashba, Properties of a 2d electron gas with lifted spectral degeneracy, *JETP lett.* **39**, 78 (1984)

[49] I. M. Miron, K. Garello, G. Gaudin, P.-J. Zermatten, M. V. Costache et al., Perpendicular switching of a single ferromagnetic layer induced by in-plane current injection, *Nature* **476**, 189 (2011)

[50] L. Liu, O. J. Lee, T. J. Gudmundsen, D. C. Ralph and R. A. Buhrman, Current-induced switching of perpendicularly magnetized magnetic layers using spin torque from the spin hall effect, *Phys. Rev. Lett.* **109**, 096602 (2012)

[51] A. Ganguly, K. Kondou, H. Sukegawa, S. Mitani, S. Kasai et al., Thickness dependence of spin torque ferromagnetic resonance in Co_75Fe_25/Pt bilayer films, *Appl. Phys. Lett.* **104**, 072405 (2014)

[52] M. D'yakonov, Spin orientation of electrons associated with the interband absorption of light in semiconductors, *Sov. Phys. JETP* **33**, 1053 (1971)

[53] Y. K. Kato, Observation of the spin Hall effect in semiconductors, *Science* **306**, 1910 (2004)

[54] J. Wunderlich, B. Kaestner, J. Sinova and T. Jungwirth, Experimental observation of the spin-Hall effect in a two-dimensional spin-orbit coupled semiconductor system, *Phys. Rev. Lett.* **94**, 047204 (2005)

[55] M. I. Dyakonov, *Future Trends in Microelectronics: From Nanophotonics to Sensors and Energy*, Wiley-IEEE Press, chapter Spin Hall Effect, pp. 251–264 (2010)

[56] J. E. Hirsch, Spin Hall effect, *Phys. Rev. Lett.* **83**, 1834 (1999)

[57] L. Liu, R. Buhrman and D. Ralph, Review and analysis of measurements of the spin hall effect in platinum, *arXiv preprint arXiv:1111.3702* (2011)

[58] S. O. Valenzuela and M. Tinkham, Direct electronic measurement of the spin hall effect, *Nature* **442**, 176 (2006)

[59] T. Kimura, Y. Otani, T. Sato, S. Takahashi and S. Maekawa, Room-temperature reversible spin Hall effect, *Phys. Rev. Lett.* **98**, 156601 (2007)

[60] L. Liu, T. Moriyama, D. C. Ralph and R. A. Buhrman, Spin-torque ferromagnetic resonance induced by the spin Hall effect, *Phys. Rev. Lett.* **106**, 036601 (2011)

[61] O. Mosendz, J. E. Pearson, F. Y. Fradin, G. E. W. Bauer, S. D. Bader et al., Quantifying spin Hall angles from spin pumping: Experiments and theory, *Phys. Rev. Lett.* **104**, 046601 (2010)

[62] A. Azevedo, L. H. Vilela-Leão, R. L. Rodríguez-Suárez, A. F. L. Santos and S. M. Rezende, Spin pumping and anisotropic magnetoresistance voltages in magnetic bilayers: Theory and experiment, *Phys. Rev. B* **83**, 144402 (2011)

[63] K. Ando, S. Takahashi, J. Ieda, Y. Kajiwara, H. Nakayama et al., Inverse spin-Hall effect induced by spin pumping in metallic system, *J. Appl. Phys.* **109**, 103913 (2011)

[64] W. Zhang, W. Han, X. Jiang, S.-H. Yang and S. S. P. Parkin, Role of transparency of platinum–ferromagnet interfaces in determining the intrinsic magnitude of the spin Hall effect, *Nature Phys.* **11**, 496 (2015)

[65] C.-F. Pai, Y. Ou, L. H. Vilela-Leão, D. C. Ralph and R. A. Buhrman, Dependence of the efficiency of spin hall torque on the transparency of Pt/ferromagnetic layer interfaces, *Phys. Rev. B* **92**, 064426 (2015)

[66] G. Mihajlović, O. Mosendz, L. Wan, N. Smith, Y. Choi et al., Pt thickness dependence of spin Hall effect switching of in-plane magnetized CoFeB free layers studied by differential planar Hall effect, *Appl. Phys. Lett.* **109**, 192404 (2016)

[67] L. Liu, C.-F. Pai, Y. Li, H. W. Tseng, D. C. Ralph et al., Spin-torque switching with the giant spin Hall effect of tantalum, *Science* **336**, 555 (2012)

[68] B. Gu, I. Sugai, T. Ziman, G. Y. Guo, N. Nagaosa et al., Surface-assisted spin Hall effect in Au films with Pt impurities, *Phys. Rev. Lett.* **105**, 216401 (2010)

[69] C.-F. Pai, L. Liu, Y. Li, H. W. Tseng, D. C. Ralph et al., Spin transfer torque devices utilizing the giant spin Hall effect of tungsten, *Appl. Phys. Lett.* **101**, 122404 (2012)

[70] C.-F. Pai, L. Liu, Y. Li, H.-W. Tseng, D. C. Ralph et al., Spin transfer torque devices utilizing the spin Hall effect of tungsten, *Bulletin of the American Physical Society* (2013)

[71] Q. Hao and G. Xiao, Giant spin Hall effect and switching induced by spin-transfer torque in a $W/Co_{40}Fe_{40}B_{20}/MgO$ structure with perpendicular magnetic anisotropy, *Phys. Rev. Appl.* **3**, 034009 (2015)

[72] J.-H. Park, *Magnetoresistive devices with perpendicular magnetic anisotropy for spin-torque driven applications*, Ph.D. thesis, Carnegie Mellon University, Ann Arbor, Pennsylvania, United States (2010)

[73] N. Akulov, Zur atomtheorie des ferromagnetismus, *Zeitschrift für Physik* **54**, 582 (1929)

[74] H. Xing, *Perpendicular exchange bias in ferromagnetic /antiferromagnetic multilayers and magnetization Switching*, Ph.D. thesis, University of Houston (2009)

[75] R. Skomski, *Simple models of magnetism*, Oxford University Press on Demand, Oxford, 1st edition (2008)

[76] L. Néel, L'approche à la saturation de la magnétostriction, *J. Phys. Radium* **15**, 376 (1954)

[77] U. Gradmann and J. Müller, Flat ferromagnetic, epitaxial 48Ni/52Fe(111) films of few atomic layers, *Phys. Stat. Sol. (b)* **27**, 313 (1968)

[78] M. T. Johnson, P. J. H. Bloemen, F. J. A. den Broeder and J. J. de Vries, Magnetic anisotropy in metallic multilayers, *Rep. Prog. Phys.* **59**, 1409 (1996)

[79] P. F. Carcia, A. D. Meinhaldt and A. Suna, Perpendicular magnetic anisotropy in Pd/Co thin film layered structures, *Appl. Phys. Lett.* **47**, 178 (1985)

[80] G. A. Bertero, R. Sinclair, C.-H. Park and Z. X. Shen, Interface structure and perpendicular magnetic anisotropy in Pt/Co multilayers, *J. Appl. Phys.* **77**, 3953 (1995)

[81] G. H. O. Daalderop, P. J. Kelly and M. F. H. Schuurmans, Magnetic anisotropy of a free-standing Co monolayer and of multilayers which contain Co monolayers, *Phys. Rev. B* **50**, 9989 (1994)

[82] J. M. MacLaren and R. H. Victora, Theoretical predictions of interface anisotropy in the presence of interdiffusion (invited), *J. Appl. Phys.* **76**, 6069 (1994)

[83] F. Bloch, Zur theorie des austauschproblems und der remanenzerscheinung der ferromagnetika, in *Zur Theorie des Austauschproblems und der Remanenzerscheinung der Ferromagnetika*, Springer, Berlin, Heidelberg, pp. 295–335 (1932)

[84] L. Néel, Energie des parois de bloch dans les couches minces, *Comptes Rendus Hebdomadaires Des Seances De L Academie Des Sciences* **241**, 533 (1955)

[85] V. L. Sobolev, Internal structure of a domain wall in ultrathin magnetic film, *J. Magn. Magn. Mater* **177-181, Part 1**, 195 (1998)

[86] A. Bellec, S. Rohart, M. Labrune, J. Miltat and A. Thiaville, Domain wall structure in magnetic bilayers with perpendicular anisotropy, *EPL (Europhysics Letters)* **91**, 17009 (2010)

[87] G. Chen, A. T. N'Diaye, S. P. Kang, H. Y. Kwon, C. Won et al., Unlocking bloch-type chirality in ultrathin magnets through uniaxial strain, *Nature Commun.* **6** (2015)

[88] P. J. Metaxas, J. P. Jamet, A. Mougin, M. Cormier, J. Ferré et al., Creep and flow regimes of magnetic domain-wall motion in ultrathin Pt/Co/Pt films with perpendicular anisotropy, *Phys. Rev. Lett.* **99**, 217208 (2007)

[89] P. Chauve, T. Giamarchi and P. Le Doussal, Creep and depinning in disordered media, *Phys. Rev. B* **62**, 6241 (2000)

[90] S. DuttaGupta, S. Fukami, C. Zhang, H. Sato, M. Yamanouchi et al., Adiabatic spin-transfer-torque-induced domain wall creep in a magnetic metal, *Nature Phys.* **12**, 333 (2016)

[91] J. Gorchon, S. Bustingorry, J. Ferré, V. Jeudy, A. B. Kolton et al., Pinning-dependent field-driven domain wall dynamics and thermal scaling in an ultrathin Pt/Co/Pt magnetic film, *Phys. Rev. Lett.* **113**, 027205 (2014)

[92] V. Jeudy, A. Mougin, S. Bustingorry, W. Savero Torres, J. Gorchon et al., Universal pinning energy barrier for driven domain walls in thin ferromagnetic films, *Phys. Rev. Lett.* **117**, 057201 (2016)

[93] S. Bustingorry, A. B. Kolton and T. Giamarchi, Thermal rounding of the depinning transition, *EPL (Europhysics Letters)* **81**, 26005 (2007)

[94] R. Diaz Pardo, W. Savero Torres, A. B. Kolton, S. Bustingorry and V. Jeudy, Universal depinning transition of domain walls in ultrathin ferromagnets, *Phys. Rev. B* **95**, 184434 (2017)

[95] E. E. Ferrero, S. Bustingorry and A. B. Kolton, Nonsteady relaxation and critical exponents at the depinning transition, *Phys. Rev. E* **87**, 032122 (2013)

[96] A. H. R. Schäfer, *Magnetic Domains: The Analysis of Magnetic Microstructures*, Springer, Berlin, Heidelberg (1998)

[97] T. A. Moore, I. M. Miron, G. Gaudin, G. Serret, S. Auffret et al., Erratum: "high domain wall velocities induced by current in ultrathin Pt/Co/AlOx wires with perpendicular magnetic anisotropy" [appl. phys. lett. 93, 262504 (2008)], *Appl. Phys. Lett.* **95**, 179902 (2009)

[98] I. M. Miron, T. Moore, H. Szambolics, L. D. Buda-Prejbeanu, S. Auffret et al., Fast current-induced domain-wall motion controlled by the rashba effect, *Nature Mater.* **10**, 419 (2011)

[99] P. P. J. Haazen, E. Murè, J. H. Franken, R. Lavrijsen, H. J. M. Swagten et al., Domain wall depinning governed by the spin Hall effect, *Nature Mater.* **12**, 299 (2013)

[100] A. Fert, N. Reyren and V. Cros, Magnetic skyrmions: advances in physics and potential applications, *Nature Reviews Materials* **2**, 17031 (2017)

[101] G. Chen, T. Ma, A. T. N'Diaye, H. Kwon, C. Won et al., Tailoring the chirality of magnetic domain walls by interface engineering, *Nature Commun.* **4** (2013)

[102] A. Fert, V. Cros and J. Sampaio, Skyrmions on the track, *Nature Nano.* **8**, 152 (2013)

[103] K. Garello, I. M. Miron, C. O. Avci, F. Freimuth, Y. Mokrousov et al., Symmetry and magnitude of spin–orbit torques in ferromagnetic heterostructures, *Nature Nano.* **8**, 587 (2013)

[104] S. Meckler, N. Mikuszeit, A. Preßler, E. Y. Vedmedenko, O. Pietzsch et al., Real-space observation of a right-rotating inhomogeneous cycloidal spin spiral by spin-polarized scanning tunneling microscopy in a triple axes vector magnet, *Phys. Rev. Lett.* **103**, 157201 (2009)

[105] O. Boulle, J. Vogel, H. Yang, S. Pizzini, D. de Souza Chaves et al., Room-temperature chiral magnetic skyrmions in ultrathin magnetic nanostructures, *Nature Nano.* **11**, 449 (2016)

[106] H. T. Nembach, J. M. Shaw, M. Weiler, E. Jué and T. J. Silva, Linear relation between Heisenberg exchange and interfacial Dzyaloshinskii-Moriya interaction in metal films, *Nature Phys.* **11**, 825 (2015)

[107] M. Belmeguenai, J.-P. Adam, Y. Roussigné, S. Eimer, T. Devolder et al., Interfacial Dzyaloshinskii-Moriya interaction in perpendicularly magnetized Pt/Co/AlO_x ultrathin films measured by Brillouin light spectroscopy, *Phys. Rev. B* **91**, 180405 (2015)

[108] K. Yamada, J.-P. Jamet, Y. Nakatani, A. Mougin, A. Thiaville et al., Influence of instabilities on high-field magnetic domain wall velocity in (Co/Ni) nanostrips, *Appl. Phys. Expr.* **4**, 113001 (2011)

[109] S.-G. Je, D.-H. Kim, S.-C. Yoo, B.-C. Min, K.-J. Lee et al., Asymmetric magnetic domain-wall motion by the Dzyaloshinskii-Moriya interaction, *Phys. Rev. B* **88**, 214401 (2013)

[110] T. J. Gallagher, K. Ju and F. B. Humphrey, State identification and stability of magnetic bubbles with unit winding number, *J. Appl. Phys.* **50**, 997 (1979)

[111] F. H. D. Leeuw, R. V. D. Doel and U. Enz, Dynamic properties of magnetic domain walls and magnetic bubbles, *Rep. Prog. Phys.* **43**, 689 (1980)

[112] Y. Kabanov, Y. Iunin, V. I. Nikitenko, A. J. Shapiro, R. D. Shull et al., In-plane field effects on the dynamics of domain walls in ultrathin Co films with perpendicular anisotropy, *IEEE Trans. Magn.* **46**, 2220 (2010)

[113] M. J. Benitez, A. Hrabec, A. P. Mihai, T. A. Moore, G. Burnell et al., Magnetic microscopy and topological stability of homochiral Néel domain walls in a Pt/Co/AlO_x trilayer, *Nature Commun.* **6**, 8957 (2015)

[114] K.-J. Kim, J.-C. Lee, S.-M. Ahn, K.-S. Lee, C.-W. Lee et al., Interdimensional universality of dynamic interfaces, *Nature* **458**, 740 (2009)

[115] S. Lemerle, J. Ferré, C. Chappert, V. Mathet, T. Giamarchi et al., Domain wall creep in an Ising ultrathin magnetic film, *Phys. Rev. Lett.* **80**, 849 (1998)

[116] L. Brillouin, Diffusion de la lumière et des rayons x par un corps transparent homogène-influence de l'agitation thermique, in *Annales de physique*, EDP Sciences (1922), volume 9, pp. 88–122

[117] L. Mandelstam, Light scattering by inhomogeneous media, *Zh. Russ. Fiz-Khim. Ova* **58**, 381 (1926)

[118] J.-H. Moon, S.-M. Seo, K.-J. Lee, K.-W. Kim, J. Ryu et al., Spin-wave propagation in the presence of interfacial Dzyaloshinskii-Moriya interaction, *Phys. Rev. B* **88**, 184404 (2013)

[119] Y. Wu, J. Stöhr, B. D. Hermsmeier, M. G. Samant and D. Weller, Enhanced orbital magnetic moment on Co atoms in Co/Pd multilayers: A magnetic circular x-ray dichroism study, *Phys. Rev. Lett.* **69**, 2307 (1992)

[120] M. Birkholz, *Thin Film Analysis by X-Ray Scattering*, Wiley (2006)

[121] M. Ali, *Growth and study of magnetostrictive FeSiBC thin films for device applications*, Ph.D. thesis, University of Sheffield (1999)

[122] S. Chikazumi, *Physics of Ferromagnetism*, Oxford University Press, Oxford, 2 edition (1997)

[123] C. Kittle, *Introduction to Solid State Physics*, Wiley (2004)

[124] Quantum Design, *Magnetic Property Measurement System, SQUID-VSM User Manual* (2009)

[125] Evico, *User instruction for evico magnetics Standard Kerr Microscope & Magnetometer*

[126] J. Cho, N.-H. Kim, S. Lee, J.-S. Kim, R. Lavrijsen et al., Thickness dependence of the interfacial Dzyaloshinskii-Moriya interaction in inversion symmetry broken systems, *Nature Commun.* **6**, 7635 (2015)

[127] R. M. Rowan-Robinson, A. A. Stashkevich, Y. Roussigné, M. Belmeguenai, S.-M. Chérif et al., The interfacial nature of proximity-induced magnetism and the Dzyaloshinskii-Moriya interaction at the Pt/Co interface, *Sci. Rep.* **7** (2017)

[128] R. Lo Conte, E. Martinez, A. Hrabec, A. Lamperti, T. Schulz et al., Role of B diffusion in the interfacial Dzyaloshinskii-Moriya interaction in $Ta/Co_{20}Fe_{60}B_{20}/MgO$ nanowires, *Phys. Rev. B* **91**, 014433 (2015)

[129] F. Ajejas, V. Křižáková, D. de Souza Chaves, J. Vogel, P. Perna et al., Tuning domain wall velocity with Dzyaloshinskii-Moriya interaction, *Appl. Phys. Lett.* **111**, 202402 (2017)

[130] D.-S. Han, N.-H. Kim, J.-S. Kim, Y. Yin, J.-W. Koo et al., Asymmetric hysteresis for probing Dzyaloshinskii-Moriya interaction, *Nano Lett.* **16**, 4438 (2016)

[131] K. Ploog, W. Stolz and L. Tapfer, Effect of barrier configuration and interface quality on structural and electronic properties of MBE-grown $Al_xGa_{1-x}As/GaAs$, $Al_xGa_{1-x}Sb/GaSb$ and $Al_xIn_{1-x}As/Ga_xIn_{1-x}As$ superlattices, in *Thin Film Growth Techniques for Low-Dimensional Structures*, Springer US, pp. 5–18 (1987)

[132] B. K. Tanner, *Characterization of crystal growth defects by X-ray methods*, volume 63 of *Nato Science Series B*, Springer US (2013)

[133] M. S. Gabureac, D. A. MacLaren, H. Courtois and C. H. Marrows, Long-ranged magnetic proximity effects in noble metal-doped cobalt probed with spin-dependent tunnelling, *New J. Phys* **16**, 043008 (2014)

[134] F. Wilhelm, M. Angelakeris, N. Jaouen, P. Poulopoulos, E. T. Papaioannou et al., Magnetic moment of Au at Au/Co interfaces: A direct experimental determination, *Phys. Rev. B* **69**, 220404 (2004)

[135] C.-J. Lin, G. Gorman, C. Lee, R. Farrow, E. Marinero et al., Magnetic and structural properties of Co/Pt multilayers, *J. Magn. Magn. Mater.* **93**, 194 (1991)

[136] I. M. Miron, G. Gaudin, S. Auffret, B. Rodmacq, A. Schuhl et al., Current-driven spin torque induced by the Rashba effect in a ferromagnetic metal layer, *Nature Mater.* **9**, 230 (2010)

[137] S. Bandiera, R. C. Sousa, B. Rodmacq and B. Dieny, Enhancement of perpendicular magnetic anisotropy through reduction of Co-Pt interdiffusion in (co/pt) multilayers, *Appl. Phys. Lett.* **100**, 142410 (2012)

[138] J. Coey, *Magnetism and Magnetic Materials*, Magnetism and Magnetic Materials, Cambridge University Press (2010)

[139] P. M. Shepley, H. Tunnicliffe, K. Shahbazi, G. Burnell and T. A. Moore, Magnetic properties, domain-wall creep motion, and the Dzyaloshinskii-Moriya interaction in Pt/Co/Ir thin films, *Phys. Rev. B* **97**, 134417 (2018)

[140] V. Jeudy, R. D. Pardo, W. S. Torres, S. Bustingorry and A. B. Kolton, Pinning of domain walls in thin ferromagnetic films, *Phys. Rev. B* **98**, 054406 (2018)

[141] A. Vansteenkiste, J. Leliaert, M. Dvornik, M. Helsen, F. Garcia-Sanchez et al., The design and verification of MuMax3, *AIP Adv.* **4**, 107133 (2014)

[142] I. M. Miron, P.-J. Zermatten, G. Gaudin, S. Auffret, B. Rodmacq et al., Domain wall spin torquemeter, *Phys. Rev. Lett.* **102**, 137202 (2009)

[143] M. Cormier, A. Mougin, J. Ferré, A. Thiaville, N. Charpentier et al., Effect of electrical current pulses on domain walls in Pt/Co/Pt nanotracks with out-of-plane anisotropy: Spin transfer torque versus joule heating, *Phys. Rev. B* **81**, 24407 (2010)

[144] T. A. Moore, I. M. Miron, G. Gaudin, G. Serret, S. Auffret et al., High domain wall velocities induced by current in ultrathin Pt/Co/AlOx wires with perpendicular magnetic anisotropy, *Appl. Phys. Lett.* **93**, 262504 (2008)

[145] M. Yamanouchi, D. Chiba, F. Matsukura and H. Ohno, Current-induced domain-wall switching in a ferromagnetic semiconductor structure, *Nature* **428**, 539 (2004)

[146] Z. Li and S. Zhang, Domain-wall dynamics driven by adiabatic spin-transfer torques, *Phys. Rev. B* **70**, 24417 (2004)

[147] H. Baker, *ASM handbook: Alloy phase diagrams*, number v. 3 in ASM Handbook: Alloy Phase Diagrams, ASM International (1992)

[148] T. B. Massalski, J. L. Murray, L. H. Bennett and H. Baker., *Binally Alloy Phase Diagrams*, volume 1, Metals Park, Ohio : American Society for Metals (1986)

[149] W. J. Antel, M. M. Schwickert, T. Lin, W. L. O'Brien and G. R. Harp, Induced ferromagnetism and anisotropy of Pt layers in Fe/Pt(001) multilayers, *Phys. Rev. B* **60**, 12933 (1999)

[150] M. Suzuki, H. Muraoka, Y. Inaba, H. Miyagawa, N. Kawamura et al., Depth profile of spin and orbital magnetic moments in a subnanometer Pt film on Co, *Phys. Rev. B* **72**, 054430 (2005)

[151] A. Barman, S. Wang, O. Hellwig, A. Berger, E. E. Fullerton et al., Ultrafast magnetization dynamics in high perpendicular anisotropy $[Co/Pt]_n$ multilayers, *J. Appl. Phys.* **101**, 09D102 (2007)

[152] E. Barati, M. Cinal, D. M. Edwards and A. Umerski, Gilbert damping in magnetic layered systems, *Phys. Rev. B* **90**, 014420 (2014)

[153] E. Barati and M. Cinal, Gilbert damping in binary magnetic multilayers, *Phy. Rev. B* **95**, 134440 (2017)

[154] J.-C. Rojas-Sánchez, N. Reyren, P. Laczkowski, W. Savero, J.-P. Attané et al., Spin pumping and inverse spin Hall effect in platinum: The essential role of spin-memory loss at metallic interfaces, *Phys. Rev. Lett.* **112**, 106602 (2014)

[155] E. M. Hankiewicz, G. Vignale and Y. Tserkovnyak, Inhomogeneous Gilbert damping from impurities and electron-electron interactions, *Phy. Rev. B* **78**, 20404 (2008)

[156] T. Kato, K. Adachi, Y. Kusanagi, S. Okamoto, N. Kikuchi et al., Gilbert damping in magnetic multilayers with perpendicular anisotropy, *Proceeding of Annual Conference of Magnetics in Japan* (2014)

[157] S. Mizukami, Y. Ando and T. Miyazaki, Ferromagnetic resonance linewidth for NM/80NiFe/NM films (NM=Cu, Ta, Pd and Pt), *J. Magn. Magn. Mater* **226-230**, 1640 (2001)

[158] S. Azzawi, A. Ganguly, M. Tokaç, R. M. Rowan-Robinson, J. Sinha et al., Evolution of damping in ferromagnetic/nonmagnetic thin film bilayers as a function of nonmagnetic layer thickness, *Phy. Rev. B* **93**, 054402 (2016)

[159] X. Ma, L. Ma, P. He, H. B. Zhao, S. M. Zhou et al., Role of antisite disorder on intrinsic Gilbert damping in $L1_0$ FePt films, *Phys. Rev. B* **91**, 014438 (2015)

[160] M. Voto, L. Lopez-Diaz, L. Torres and S. Moretti, Disorder-induced domain wall velocity shift at high fields in perpendicularly magnetized thin films, *Phys. Rev. B* **94**, 174438 (2016)

[161] S. Moretti, M. Voto and E. Martinez, Dynamical depinning of chiral domain walls, *Phys. Rev. B* **96**, 054433 (2017)

[162] Y. Yoshimura, K.-J. Kim, T. Taniguchi, T. Tono, K. Ueda et al., Soliton-like magnetic domain wall motion induced by the interfacial Dzyaloshinskii-Moriya interaction, *Nature Phys.* **12**, 157 (2016)

[163] T. Weindler, H. Bauer, R. Islinger, B. Boehm, J.-Y. Chauleau et al., Magnetic damping: Domain wall dynamics versus local ferromagnetic resonance, *Phys. Rev. Lett.* **113**, 237204 (2014)

[164] H. D. Arnold and G. W. Elmen, Permalloy, a new magnetic material of very high permeability, *Bell System Technical Journal* **2**, 101 (1923)

[165] T. Jungwirth, J. Sinova, J. Mašek, J. Kučera and A. H. MacDonald, Theory of ferromagnetic (III,mn)v semiconductors, *Rev. Mod. Phys.* **78**, 809 (2006)

[166] C. Gould, K. Pappert, G. Schmidt and L. Molenkamp, Magnetic anisotropies and (ga,mn)as-based spintronic devices, *Adv. Mater.* **19**, 323 (2007)

[167] S. Lee, J.-H. Chung, X. Liu, J. K. Furdyna and B. J. Kirby, Ferromagnetic semiconductor GaMnAs, *Mater. Today* **12**, 14 (2009)

[168] W. Jiang, P. Upadhyaya, W. Zhang, G. Yu, M. B. Jungfleisch et al., Blowing magnetic skyrmion bubbles, *Science* **349**, 283 (2015)

[169] T. Miyajima, T. Ibusuki, S. Umehara, M. Sato, S. Eguchi et al., Transmission electron microscopy study on the crystallization and boron distribution of CoFeB/MgO/CoFeB magnetic tunnel junctions with various capping layers, *Appl. Phys. Lett.* **94**, 122501 (2009)

[170] S. Woo, K. Litzius, B. Krüger, M.-Y. Im, L. Caretta et al., Observation of room-temperature magnetic skyrmions and their current-driven dynamics in ultrathin metallic ferromagnets, *Nature Mater.* **15**, 501 (2016)

[171] P. Poulopoulos, A. Scherz, F. Wilhelm, H. Wende and K. Baberschke, Direct probe of induced magnetic moments at interfaces via X-ray magnetic circular dichroism, *phys. status solidi (a)* **189**, 293

[172] S. Ingvarsson, G. Xiao, S. Parkin and W. Gallagher, Thickness-dependent magnetic properties of $Ni_{81}Fe_{19}$, $Co_{90}Fe_{10}$ and $Ni_{65}Fe_{15}Co_{20}$ thin films, *J. Magn. Magn. Mater.* **251**, 202 (2002)

[173] Y.-H. Wang, W.-C. Chen, S.-Y. Yang, K.-H. Shen, C. Park et al., Interfacial and annealing effects on magnetic properties of CoFeB thin films, *J. Appl. Phys.* **99**, 08M307 (2006)

[174] K. Oguz, P. Jivrajka, M. Venkatesan, G. Feng and J. M. D. Coey, Magnetic dead layers in sputtered $Co_{40}Fe_{40}B_{20}$ films, *J. Appl. Phys.* **103**, 07B526 (2008)

[175] J. Yu, X. Qiu, Y. Wu, J. Yoon, P. Deorani et al., Spin orbit torques and Dzyaloshinskii-Moriya interaction in dual-interfaced Co-Ni multilayers, *Sci. Rep.* **6**, 32629 (2016)

[176] S. Y. Jang, S. H. Lim and S. R. Lee, Magnetic dead layer in amorphous CoFeB layers with various top and bottom structures, *J. Appl. Phys.* **107**, 09C707 (2010)

[177] S. Bandiera, R. C. Sousa, B. Rodmacq and B. Dieny, Asymmetric interfacial perpendicular magnetic anisotropy in Pt/Co/Pt trilayers, *IEEE Magn. Lett.* **2**, 3000504 (2011)

[178] C.-W. Cheng, W. Feng, G. Chern, C. M. Lee and T. ho Wu, Effect of cap layer thickness on the perpendicular magnetic anisotropy in top MgO/CoFeB/Ta structures, *J. Appl. Phys.* **110**, 033916 (2011)

[179] S. Y. Jang, C.-Y. You, S. H. Lim and S. R. Lee, Annealing effects on the magnetic dead layer and saturation magnetization in unit structures relevant to a synthetic ferrimagnetic free structure, *J. Appl. Phys.* **109**, 013901 (2011)

[180] H. Sato, M. Yamanouchi, S. Ikeda, S. Fukami, F. Matsukura et al., Perpendicular-anisotropy CoFeB-MgO magnetic tunnel junctions with a MgO/CoFeB/Ta/CoFeB/MgO recording structure, *Appl. Phys. Lett.* **101**, 022414 (2012)

[181] J. Sinha, M. Hayashi, A. J. Kellock, S. Fukami, M. Yamanouchi et al., Enhanced interface perpendicular magnetic anisotropy in Ta/CoFeB/MgO using nitrogen doped Ta underlayers, *Appl. Phys. Lett.* **102**, 242405 (2013)

[182] B. Zhang, A. Cao, J. Qiao, M. Tang, K. Cao et al., Influence of heavy metal materials on magnetic properties of Pt/Co/heavy metal tri-layered structures, *Appl. Phys. Lett.* **110**, 012405 (2017)

[183] N. O. Nnolim, *Understanding the origins of metastability in thin film growth; tantalum and the early group VB-VIB metals*, Ph.D. thesis, Federated Physics Department, New Jersey Institute of Technology (2003)

[184] N. B. Caballero, I. F. Aguirre, L. J. Albornoz, A. B. Kolton, J. C. Rojas-Sánchez et al., Excess velocity of magnetic domain walls close to the depinning field, *Phys. Rev. B* **96**, 224422 (2017)

[185] A. Kirilyuk, J. Ferré, V. Grolier, J. Jamet and D. Renard, Magnetization reversal in ultrathin ferromagnetic films with perpendicular anisotropy, *J. Magn. Magn. Mater.* **171**, 45 (1997)

[186] N.-H. Kim, J. Jung, J. Cho, D.-S. Han, Y. Yin et al., Interfacial Dzyaloshinskii-Moriya interaction, surface anisotropy energy, and spin pumping at spin orbit coupled Ir/Co interface, *Appl. Phys. Lett.* **108**, 142406 (2016)

[187] A. A. Stashkevich, M. Belmeguenai, Y. Roussigné, S. M. Cherif, M. Kostylev et al., Experimental study of spin-wave dispersion in Py/Pt film structures in the presence of an interface Dzyaloshinskii-Moriya interaction, *Phys. Rev. B* **91**, 214409 (2015)

[188] J. P. Pellegren, D. Lau and V. Sokalski, Dispersive stiffness of Dzyaloshinskii domain walls, *Phys. Rev. Lett.* **119**, 027203 (2017)

[189] F. Freimuth, S. Blügel and Y. Mokrousov, Berry phase theory of Dzyaloshinskii-Moriya interaction and spin-orbit torques, *J. Phys. Condens. Matter* **26**, 104202 (2014)

[190] K. Zeissler, M. Mruczkiewicz, S. Finizio, J. Raabe, P. Shepley et al., Pinning and hysteresis in the field dependent diameter evolution of skyrmions in Pt/Co/Ir superlattice stacks, *Sci, Rep.* **7**, 15125 (2017)

[191] T. H. Pham, J. Vogel, J. Sampaio, M. Vaňatka, J.-C. Rojas-Sánchez et al., Very large domain wall velocities in Pt/Co/GdO$_x$ and Pt/Co/Gd trilayers with Dzyaloshinskii-Moriya interaction, *EPL (Europhysics Letters)* **113**, 67001 (2016)

[192] D.-Y. Kim, D.-H. Kim, J. Moon and S.-B. Choe, Determination of magnetic domain-wall types using Dzyaloshinskii-Moriya-interaction-induced domain patterns, *App. Phys. Lett.* **106**, 262403 (2015)

[193] I. Gross, L. J. Martínez, J.-P. Tetienne, T. Hingant, J.-F. Roch et al., Direct measurement of interfacial Dzyaloshinskii-Moriya interaction in x|CoFeB|MgO heterostructures with a scanning nv magnetometer (x = Ta, TaN, and W), *Phys. Rev. B* **94**, 064413 (2016)

[194] X. Ma, G. Yu, X. Li, T. Wang, D. Wu et al., Interfacial control of Dzyaloshinskii-Moriya interaction in heavy metal/ferromagnetic metal thin film heterostructures, *Phys. Rev. B* **94**, 180408 (2016)

[195] S. Tacchi, R. E. Troncoso, M. Ahlberg, G. Gubbiotti, M. Madami et al., Interfacial Dzyaloshinskii-Moriya interaction in Pt/CoFeB films: Effect of the heavy-metal thickness, *Phys. Rev. Lett.* **118**, 147201 (2017)

[196] X. Ma, G. Yu, C. Tang, X. Li, C. He et al., Interfacial Dzyaloshinskii-Moriya interaction: Effect of 5d band filling and correlation with spin mixing conductance, *Phys. Rev. Lett.* **120**, 157204 (2018)

[197] K. Yamamoto, A.-M. Pradipto, K. Nawa, T. Akiyama, T. Ito et al., Interfacial Dzyaloshinskii-Moriya interaction and orbital magnetic moments of metallic multilayer films, *AIP Adv.* **7**, 056302 (2017)

[198] C. Moreau-Luchaire, C. Moutafis, N. Reyren, J. Sampaio, C. Vaz et al., Additive interfacial chiral interaction in multilayers for stabilization of small individual skyrmions at room temperature, *Nature Nano.* **11**, 444 (2016)

[199] M. Baćani, M. A. Marioni, J. Schwenk and H. J. Hug, How to measure the local Dzyaloshinskii Moriya interaction in skyrmion thin film multilayers, *arXiv preprint arXiv:1609.01615* (2016)

[200] Singulus Technologies AG, Hanauer Landstrasse 103, D-63796 Kahl, Germany, *TIMARIS: PVD Cluster Tool for Magnetic Storage & Semiconductor Wafer Production* (2012)

[201] R. J. G. T. Suzuki, *Magneto-Optical Recording Materials*, Wiley-IEEE Press (1999)

[202] Z. G. Li, P. F. Carcia and Y. Cheng, Co thickness dependence of the microstructure of Pt/Co multilayers, *J. Appl. Phys.* **73**, 2433 (1993)

[203] C.-F. Pai, M.-H. Nguyen, C. Belvin, L. H. Vilela-Leão, D. C. Ralph et al., Enhancement of perpendicular magnetic anisotropy and transmission of spin-Hall-effect-induced spin currents by a Hf spacer layer in W/Hf/CoFeB/MgO layer structures, *Appl. Phys. Lett.* **104**, 082407 (2014)

[204] M. Akyol, J. G. Alzate, G. Yu, P. Upadhyaya, K. L. Wong et al., Effect of the oxide layer on current-induced spin-orbit torques in Hf|CoFeB|MgO and Hf|CoFeB|TaO_x structures, *Appl. Phys. Lett.* **106**, 032406 (2015)

[205] A. T. Hindmarch, V. Harnchana, A. S. Walton, A. P. Brown, R. M. D. Brydson et al., Zirconium as a boron sink in crystalline CoFeB/MgO/CoFeB magnetic tunnel junctions, *Appl. Phys. Exp.* **4**, 013002 (2010)

[206] T. Liu, J. W. Cai and L. Sun, Large enhanced perpendicular magnetic anisotropy in CoFeB/MgO system with the typical Ta buffer replaced by an Hf layer, *AIP Adv.* **2**, 032151 (2012)

[207] C. Ederer, M. Komelj, M. Fähnle and G. Schütz, Theory of induced magnetic moments and x-ray magnetic circular dichroism in Co-Pt multilayers, *Phys. Rev. B* **66**, 94413 (2002)

[208] C. Klewe, T. Kuschel, J.-M. Schmalhorst, F. Bertram, O. Kuschel et al., Static magnetic proximity effect in Pt/Ni_{1-x} Fe_x bilayers investigated by x-ray resonant magnetic reflectivity, *Phys. Rev. B* **93**, 214440 (2016)

[209] Y. Kitamoto, T. Takeuchi, K. Tsunekawa, Y. suk Choi, Y. Nagamine et al., Annealing-induced solid-phase epitaxy at interfaces between CoFeB layers and MgO barrier-layer in CoFeB/MgO/CoFeB magnetic tunnel junctions and their magnetic properties, in *ECS Transactions*, ECS (2009)

[210] Y. Huang, X. Li, L. Wang, G. Yu, K. L. Wang et al., Interface control of domain wall depinning field, *AIP Advances* **8**, 056314 (2018)